ULTRASOUND-INDUCED THERMAL THERAPY OF HYPERPLASIA IN RINGED EXPANDED POLYTETRAFLUOROETHYLENE (ePTFE) ACCESS GRAFTS

by

Michael Earl Query

A thesis submitted to the faculty of
The University of Utah
in partial fulfillment of the requirements for the degree of

Master of Science

Department of Electrical and Computer Engineering

The University of Utah

May 2014

The University of Utah Graduate School

STATEMENT OF THESIS APPROVAL

The thesis of **Michael Earl Query**

has been approved by the following supervisory committee members:

Douglas A. Christensen	, Chair	**8/23/2013** Date Approved
Yan-Ting E. Shiu	, Member	Date Approved
Bruce K. Gale	, Member	**8/23/2013** Date Approved

and by **Gianluca Lazzi** , Chair/Dean of

the Department/College/School of **Electrical and Computer Engineering**

and by David B. Kieda, Dean of The Graduate School.

ABSTRACT

Hemodialysis vascular access, the interface between a dialysis patient and a dialysis machine, is quite literally the lifeblood of a patient's health. Vascular access dysfunction is the leading cause of hospitalization in hemodialysis patients. The occlusive growth of neointimal hyperplasia (NH) in expanded polytetrafluoroethylene (ePTFE) ringed grafts is the primary cause of failure. To further develop a proposed thermal ultrasound treatment to reduce or prevent NH in arteriovenous vascular grafts, the acoustic properties of ePTFE were studied in water and alcohol solutions. Previous reports of ePTFE acoustic properties are critiqued. It was found that the acoustic transmission and attenuation through ePTFE, and therefore the potential for an ultrasound-based therapy for NH, are heavily dependent on the medium in which the graft is immersed, suggesting that the acoustic properties of implanted grafts will change as grafts mature *in vivo*. The acoustic impedance and attenuation of water-soaked ePTFE were $0.478 \pm 1.43 \times 10^{-2}$ MRayl and 1.78 ± 0.111 Np/cm·MHz, respectively, while the acoustic impedance and attenuation of ePTFE in alcohol were 1.49 ± 0.149 MRayl and $0.77 \pm 1.1 \times 10^{-2}$ Np/cm·MHz, respectively.

The use of focused ultrasound to heat implanted ringed ePTFE grafts was numerically modeled from 1.35- and 1.443-MHz transducers for *in vitro* geometries. Power deposition and heating, in turn, differed by an order of magnitude between various graft acoustic properties. Graft rings were predicted to be substantial absorbing and

scattering features.

In vitro phantom models were constructed: one with and one without thermocouples. At 1 W of acoustic power, the maximum temperature rise was 8˚ C. The thermocouple model containing a water-soaked graft did not experience heating in the far graft wall. The MRTI model confirmed that the graft rings are an absorbing/scattering feature. Heating was not prevented in the presence of water flow through the graft. Water was not heated significantly. Overall, results suggest ultrasound exposure can be used to generate temperature rises corresponding with the potential prevention or inhibition of NH in ringed ePTFE vascular grafts.

A hybrid therapeutic/diagnostic transducer design with a therapeutic semi-annular array surrounding a diagnostic linear array is presented. Compared to a solid transducer of the same dimensions, there were only marginal aberrations in the focal plane. Numerical optimization of the element drive configuration indicated that the least distorted focal plane was produced by uniform phase and magnitude at each element.

TABLE OF CONTENTS

LIST OF TABLES

ACKNOWLEDGEMENTS

I would like to thank my supervisory committee, Dr. Douglas A. Christensen, Dr. Yan-Ting E. Shiu, and Dr. Bruce K. Gale. Dr. Christensen provided invaluable mentoring and references as well as expertise in the physics of ultrasound and the use of the hybrid angular spectrum algorithm and accompanying software. Dr. Shiu arranged for generous support and offered tactful guidance to the method of research in addition to a wealth of biological insight. Dean Constantine of Constantine Technologies, LLC fulfilled the role of a de facto member of the supervisory committee providing many idea-exchanging conversations, the use of laboratory facilities and equipment, and constant encouragement. The HIFU group at the University of Utah arranged for the magnetic resonance temperature imaging experiment to be performed and Nick Todd answered questions about MRI and the related data analysis. My parents, Mike and Linda Query, deserve thanks for providing room and board for most of this process and love through all of it. I would also like to thank my wife, Amy, for her confidence and endless patience.

CHAPTER 1

INTRODUCTION

1.1 Motivation

Hemodialysis vascular access, the interface between a dialysis patient and a dialysis machine, is quite literally the lifeblood of a patient's health. The vascular access is the pivotal component of a complete blood "circuit" mating patient with purifier. Initiated at the heart, flow moves through the arterial system, eventually being exported at a vascular access. After dialysis, the flow returns to the heart through the venous system. Blood flow can be adversely affected by problems that occur anywhere within this circuit; however, hemodialysis vascular access complications are the leading cause of morbidity in hemodialysis patients [4].

There are three options for vascular access: arteriovenous (AV) fistulae, AV grafts, and central venous catheters. Catheters tend to be used only in emergent situations owing to their quick but short-lived access. Of the two remaining options, the current clinical preference is to create an AV fistula (a surgically created connection between an artery and a vein, usually in the forearm) due to the comparatively higher morbidity in grafts. This is true in defiance of the fact that grafts can reach functional maturity 4-6 times faster than fistulae [5]. The failure rate of a vascular access graft is directly related to progressive neointimal hyperplasia (NH), or excessive smooth muscle cell

proliferation at the anastomosis and on the interior of the graft. NH occludes blood flow and, if left unchecked, leads to graft thrombosis. The prevention or inhibition of NH in AV grafts could provide more rapid and reliable vascular access for hemodialysis patients.

1.2 Problem Statement

AV grafts are most commonly constructed from expanded polytetrafluoroethylene (ePTFE), an extruded Teflon®/PTFE material. It has been proposed that NH can be inhibited in ePTFE grafts by localized mild hyperthermia produced by ultrasonic exposure [2] [3]. Often grafts are made with PTFE windings (see Figure 1) to maintain rigidity and prevent kinking as opposed to the bare grafts described in [2] [3]. In many vascular applications, ringed grafts are preferred to bare grafts [6] [7]. However, adding rings to graft geometry could have a significant effect on the nature of the temperature

Figure 1. Bare (bottom) and ringed (top) ePTFE vascular grafts.

rise in ringed grafts. This thesis addresses whether or not temperature rise sufficient to inhibit NH can be achieved in ringed-graft physical models and numerical simulations.

1.3 Research Strategy

The studies of this thesis were based on three goals: first, evaluating the acoustic parameters of ringed ePTFE vascular grafts; second, numerically simulating and physically measuring ultrasonically induced temperature rise in *in vitro* models to verify that adequate graft heating can be achieved through ultrasonic therapy in ringed grafts; and third, designing and simulating a serviceable transducer to simultaneously monitor and produce therapy in a practical clinical setting.

1.4 Outline of Chapters

1.4.1 Chapter 2: Literature Review

Foundational theory and relevant literature regarding thermal and ultrasonic treatment of hyperplasia are presented and critiqued. Related therapies are examined and categorical rationale is provided for the chosen direction of research in this thesis.

1.4.2 Chapter 3: ePTFE Ringed Graft Acoustic Properties

Due to differences in published values for acoustic parameters of ePTFE used in vascular grafts, a study was performed to measure graft acoustic properties and to explain the disparity between previous publications. The porous nature of ePTFE was found to lead to a range of acoustic properties depending on the graft's environment. Graft acoustic properties were measured in three surrounding media.

1.4.3 Chapter 4: Simulations and *In Vitro* Physical Models of Ringed Grafts

To ensure adequate but not excessive heating, it is important to verify that reliable and predictable temperature rise can be achieved ultrasonically. Numerical simulations depicting the heating of the ringed graft geometry were performed by the hybrid angular spectrum (HAS) algorithm using MATLAB® and COMSOL Multiphysics®. Published ePTFE material property values [3] and measured ePTFE material property values (see Chapter 3) were used for the modeled graft material. Physical models were created with a tissue-simulating phantom material and an implanted ringed ePTFE graft. The graft was targeted with high-intensity focused ultrasound (HIFU) and temperature rise was measured by two means: implanted thermocouples and magnetic resonance temperature imaging (MRTI). Because of experimental transducer misalignment, further numerical simulations were conducted to explain discrepancies between original numerical results and experimental values.

1.4.4 Chapter 5: Transducer Design

The piezoelectric element layout of a hybrid transducer was designed with a linear array for diagnosis surrounded by a semi-annular array for therapy. The layout geometry is suited for a handheld NH treatment in a practical clinical setting. MATLAB was used to compute the Rayleigh-Sommerfeld integral to optimize the pressure pattern of the designed transducer.

1.4.5 Chapter 6: Conclusions and Suggestions for Future Work

The results of the experiments comprising Chapters 3-5 were discussed as a whole in the context of a potential NH treatment. Two potential branches of future study are suggested: *in vivo* studies in animal models and ultrasound therapy enhanced by contrast agent.

CHAPTER 2

LITERATURE REVIEW

Though the focus of this study is specific to AV grafts, the techniques presented have the potential for broader application in vascular stents and fistulae. For this reason, the following literature citation will include instrumental work relating to those secondary groups.

2.1 Neointimal Hyperplasia in Vascular Accesses

Restenosis and thrombosis are significant limiting factors in the efficacy and vitality of implanted vascular stents, grafts, and fistulae [8] [9] [10]. Neointimal hyperplasia, an abnormal accumulation primarily of smooth muscle cells (SMCs) and myofibroblasts on the intimal wall of native or prosthetic vascular tissue [11] [12], has been characterized as the major mechanism of restenosis in cardiac stents, synthetic AV grafts, and AV fistulae [13] [14] [15]. In addition, thrombosis in AV access most commonly occurs as a result of the progressive narrowing of the graft lumen due to NH [16].

NH is being combatted on a number of fronts. Currently, no effective pharmacotherapy or brachytherapy is available to reliably prevent the occurrence of NH in stents, fistulae, or grafts. Several approaches have been proposed to inhibit NH.

Major advances have been made in the field of interventional cardiology with the development and adoption of drug-eluting stents. However, there is still need for improved therapy, particularly concerning in-stent restenosis [17] [18].

Even though the arteriovenous fistula is being promoted as the vascular access of choice for hemodialysis patients [19], NH remains a point of concern in fistulae [20]. Brachytherapy has been shown to reduce NH by 30-50% [21]. Drug-therapy studies are numerous but have not yet resulted in a clear clinical solution [21].

There are numerous methods of NH inhibition that have been and are being studied with regard to AV grafts. One approach is to selectively promote the growth of endothelial cells (ECs) on the luminal surface of the vascular graft [22] [23]. The expectation is that endothelialization of the vascular graft will inhibit the growth of the underlying SMCs by the release of nitric oxide and other inhibitors. However, a recent study showed that the seeding of endothelial progenitor cells actually increased, rather than decreased, the stenosis of AV grafts in an animal model [24]. An alternative approach is to prevent the growth of all cells, including ECs, on the graft surface. This has been accomplished with potent antiproliferative drugs, such as paclitaxel and sirolimus [25] [26]. While drug-eluting stents have greatly improved the outcome of coronary angioplasty, a disadvantage of this approach for AV grafts is that it requires an invasive procedure (angioplasty to deliver the stent) and implantation of a foreign material (the stent) which cannot be readily removed; further, the long-term results of this approach in maintaining the graft patency are unknown. Efforts have been made to achieve the sustained release of antiproliferative drugs using hydrogel delivery systems in the vicinity of the graft anastomosis, the location that is most prone to the development of

NH [27]. Catheter-based delivery of gamma radiation is yet another method that has been investigated for preventing cell proliferation on graft lumens [28]. However, for synthetic vascular grafts, none of the above-mentioned strategies has yet proven effective in humans.

2.2 Thermal and Ultrasonic Effects on the Components of Hyperplasia

There has been and continues to be much investigation into the prevention and inhibition of NH. Although progress has been made on various fronts (pharmaceutical, radiative, etc.) there is not yet a comprehensive solution. From this point on, this review will concern itself with NH treatments having a component of thermal therapy and/or ultrasonic mechanical action. The term sonomechanical will be used to distinguish the purely mechanical effects of ultrasound from thermal and chemical effects. Although the term sonodynamic is sometimes used in the literature to refer to any nonthermal, ultrasound-actuated process, in this paper, "sonodynamic" will signify only sonochemical mechanisms.

Prior to an in-depth discussion on the treatments of NH involving thermal and ultrasonic mechanisms, it will be useful to briefly consider some of the research that describes the biological effects of ultrasound and hyperthermia as related to NH.

2.3 Hyperthermia in the Arena of Neointimal Hyperplasia

In 2002, Orihara *et al.* published findings describing the effects of mild hyperthermia on vascular SMCs [29]. Their study indicated that SMC proliferation, when compared to EC proliferation, was selectively inhibited after a 2-hour thermal

exposure of 43° C. Hyperthermia was shown to hinder the cell maturation process. The curtailing effect was transient though; when exposed-cells were compared with a control groups five days after exposure, analysis of the cells' progression through the cell cycle showed no differences.

Research conducted by Mark Brinton at the University of Utah [30] considered the effects of mild hyperthermia on ECs deposited on ePTFE, a common AV graft material. He found that after exposures of 43-50° C for various durations, ECs on ePTFE were more susceptible to mild hyperthermia-induced cell death than those on tissue culture dishes.

2.3.1 Ultrasound in the Arena of Neointimal Hyperplasia

Lejbkowicz and Salzberg analyzed the sensitivity of normal and malignant cells to low frequency (20 kHz), low power (0.33 W/cm^2), continuous wave (CW) ultrasound exposure [31]. They concluded that there was a harmful, purely sonomechanical effect on cell health after 4-minute exposures. To isolate mechanical and thermal effects, heating tests were performed. The study indicated that thermal effects on cell health would not be seen until 42° C. At the prescribed frequency and power level, it took 40 minutes to see temperatures in that range. That result is sufficient to show ultrasound-induced differences between experimental and control groups were produced by a purely mechanical effect.

In addition, in [32], Alter *et al.* analyzed the response of SMCs to ultrasonic radiation. She reported that cell migration and adhesion could be inhibited by low frequency cavitational/mechanical ultrasound *in vitro* with 1.5-W, 15-second exposures

to unfocused 20-kHz ultrasound. In particular, Alter conjectures about the mechanism by which adhesion and migration were inhibited. She purports that the observed disorganization of α-SM actin fibers and diminished distribution of vinculin in ultrasound-exposed SMCs accounts for their lack of adhesion and migration. This was interpreted to mean that a basic structural cytoskeletal change had been induced by "sonication" which led to altered SMC morphology and function.

Even more encouraging for potential sonomechanical NH treatment is the research conducted by Lawrie *et al.* in [33]. When comparing sonicated SMCs and ECs *in vitro*, it was shown that SMC proliferation was reduced selectively. In that study, ultrasound exposure lasted 60 seconds at an operating frequency of 1 MHz with a spatial average temporal average intensity of 0.4 W/cm^2. In this experiment, temperature rose to 51°C at the end of the 60-second exposure, but returned to 37°C within 45 seconds. When exposing the cells to an identical temperature rise in the absence of ultrasound, the number of cells adhering to the substrate before and after exposure was unaffected. The conclusion was drawn that this temperature rise had no impact on adherence and proliferation results.

2.3.2 Connections to Neointimal Hyperplasia

The thermal findings suggest that in the environments where NH exists, and considering the biological makeup of NH, it may be possible to selectively target hyperplastic growth with purely thermal treatment *in vivo*. From the ultrasonic exposure publications, the same conclusion can be drawn about ultrasonic radiation.

Research investigating hyperthermia and ultrasound (US) for cancer therapy

found that mild hyperthermia (40° C for 30 minutes) and very low intensity US (0.081 W/cm^2 at 1 MHz) enhanced apoptotic cell death when the US treatment followed the hyperthermia [34]. When the US treatment preceded the hyperthermic treatment, there was an increase in cell lysis. This suggests that hyperthermia inhibits the repair of membrane damage caused by the US, and US can augment the apoptosis that hyperthermia initiates [35] [36]. The effects of this type of combinatorial treatment on SMCs and NH have not yet been quantified.

2.4 Ultrasonic and Thermal Therapies for Hyperplasia

2.4.1 Sonotherapy

2.4.1.1 Background

This procedure was originated by a group led by Peter Fitzgerald primarily concerned with in-stent restenosis in cardiovascular stents. The therapy involved inserting an intravascular ultrasound (IVUS) catheter with a radiating element into the lumen of a cardiovascular stent and exposing the NH to therapeutic levels of ultrasound. Compared to other ultrasound treatments, sonotherapy is relatively benign in terms of thermal and mechanical potential for damage (see Figure 2) [1].

2.4.1.2 Methods and Results

In their first publication in 2001 on the topic [37], Fitzgerald *et al.* reported drastic differences in the neointimal growth of stents implanted in swine that had undergone sonotherapy compared to a sham group. Stent implantation was preceded by a balloon overexpansion injury used to induce hyperplasia. Sonotherapy was administered via a

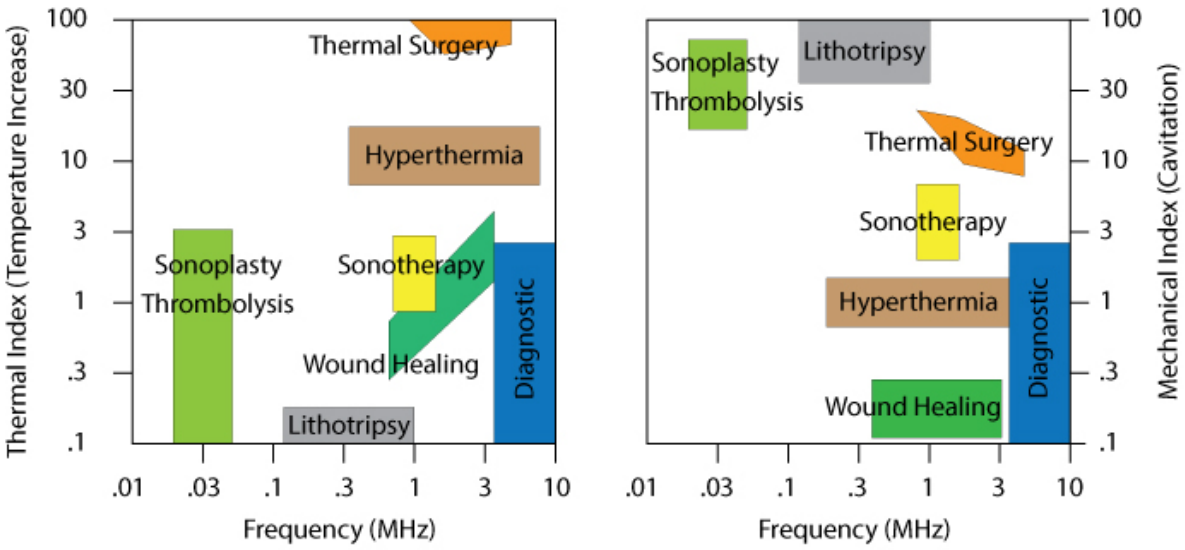

Figure 2. Sonotherapy in comparison with other therapies. Left: thermal index. Right: mechanical index [1].

radially radiating element 8 mm in length at the tip of a catheter that was inserted into the lumen of the stent directly after implantation. The ultrasound was delivered in a pulsed mode at 700 kHz with a mechanical index of 3.9. In the sham group, the catheter was inserted for the same treatment time, but the ultrasound was never actuated. SMC proliferation was assessed seven days following sonotherapy and neointimal thickness was recorded at 28 days. In the experimental group seven days after therapy, there were significantly fewer SMCs proliferating in the intima than in the control group. At 28 days, there was a substantially smaller percentage of stenosis in the treated group than in the sham group.

A second study using a coronary stent swine model showed inhibited neointimal growth in addition to reporting no evidence of thrombi during or after treatment. The study showed complete endothelialization on the luminal surface of implanted stents [37].

A third, specially circumstanced, case study took place at the Texas Children's Hospital in 2003. A two-year-old boy was suffering from recurring pulmonary vein stenosis after a reparative operation. Within the previous 17 months, the boy had undergone two surgical procedures to recanalize both pulmonary veins. After obtaining special FDA approval, the boy was treated with sonotherapy. Using the 700-kHz catheter system, the patient underwent a 10-minute exposure in both pulmonary veins. Three months after the treatment, the patient showed significantly better clinical, radiographic, and echocardiographic assessments. After the same amount of time passed subsequent to prior interventions, he had manifested severely discouraging clinical and analytical indicators [38].

These results sparked increased interest and a set of clinical trials to evaluate the safety of the procedure on human subjects generally. Prior to the initiation of clinical trials, the operating frequency was adjusted to 1 MHz and three 6-mm long elements replaced the single element on the catheter. The therapy procedure for clinical trials was similar to the preclinical studies. The trial results reported late lumen loss, defined as the minimum lumen diameter immediately after stenting and the minimum lumen diameter at a six-to-eight month follow-up, and neointimal growth similar to conventional approaches at six months after the procedure [39].

In spite of the fact that there was significant late lumen loss, a successful safety evaluation and the promising results from the initial studies spurred a randomized, double-blind set of clinical efficacy studies to be initiated. Later revisions of the catheter system included 3-6 operating elements and operating frequencies of 1.0 to 1.4 MHz. The SILENT (Sonotherapy for In-Lesion Elimination of Neointimal Tissue), SWING

(Sound Wave Inhibition of Neointimal Growth), EuroSPAH (European Sonotherapy Prevention of Arterial Hyperplasia), and SPLASH (Sonotherapy Prevention of Later Arterial In-Stent Hyperplasia) trials were performed to evaluate the range of efficacy and confirm initial safety findings [40].

Despite the promising case study and preclinical results, the trials failed to meet their primary endpoints for long-term efficacy [41], as explained next.

2.4.1.3 Discussion

The results of the trials have had various interpretations. Although the specified endpoints for late lumen loss were not met, sonotherapy performed better than sham treatments. Dr. Patrick Serruys, the principal investigator of the EuroSPAH trial, said of the results, "EuroSPAH is one of the very few double-blind studies in interventional cardiology. This is important to understand, especially when reviewing the variance observed between the clinical and angiographic results. That is, the physicians in this trial, who were truly blinded, chose to reduce interventions by more than 40% based on their clinical and angiographic assessment" [42].

Dr. Karl R. Karsch of Bristol University acted as a discussant for the trial. He noted that, notwithstanding the movement in the right direction, the trial still came to a negative conclusion. "So if we go back and look at the experimental…data for a technique then used in a randomized trial, in my opinion…this has not been shown and analyzed thoroughly enough to really go to a clinical experiment" [42].

Sonotherapy treatments were most likely proposed and studied as nonrepetitive treatments because of their invasive nature. The *in vitro* studies suggested that sonication

of the SMCs would produce a transient effect on migration and adhesion [32]. As cells multiply and reproduce *in vivo*, the effects of a sonotherapy treatment would likely not be long-lasting. It is this author's opinion that a repetitive therapy based on the same principles would be more likely to produce more efficacious, long-term effects.

There has been at least one other documented alteration proposed for sonotherapy: that it may be a good candidate for the enhancement of localized pharmacological or gene therapy treatment [1]. At the time of this thesis publication, Cybersonics, Inc. [43] owned the intellectual property related to sonotherapy, but is not currently pursuing its development.

2.4.2 Far Infrared Therapy

2.4.2.1 Background

Far Infrared Radiation (FIR) is a class of electromagnetic radiation which has wavelengths in the 5.6-1000-μm (longer than visible light) range. Its effects are essentially thermal when introduced to biological tissue [44]. In the following studies, this radiation is therapeutically applied with an unfocused laser source.

In 2001, Kipshidze *et al.* published data that described the effect of short-pulsed, nonablative, laser irradiation on vascular cells *in vitro* and hyperplasia in a rabbit balloon injury model [45]. Using ultra-short, low-power (160 ns at 260 mJ) bursts of FIR-dosing delivered with optical fibers, cell cultures of SMCs and ECs were exposed. In contrast to unexposed control groups, SMCs that underwent FIR-dosing experienced nearly 50% destruction three hours after exposure. Moreover, cell proliferation was abidingly inhibited nine days following radiation. ECs on the other hand were not as sensitive to

FIR. None of the experiments produced any thermocouple-detectable heating above 37°C (control temperature).

In a rabbit model, hyperplasia was induced with a balloon injury in the iliac artery. In an experimental group, laser irradiation (10 pulses of 260 mJ for 160 ns) was performed intravenously immediately following the balloon injury during the same intervention. The sham group experienced the same balloon injury, but the laser source was not activated. After 60 days, the intimal growth was significantly arrested in the experimental group when compared with the control.

2.4.2.2 Methods and Results

Advancing from the foundational work in [45], Chih-Ching Lin *et al.* developed a noninvasive treatment using FIR for hyperplasia in AV fistulae [46]. A clinical trial was performed in which patients who were receiving four hours of hemodialysis (HD) treatment three times weekly also received 40 minutes of FIR therapy. The FIR was performed using a commercial FIR device emitting 5-12-μm infrared radiation 25 cm above the surface of the AV fistula.

Using blood flow as a measure of fistula stenosis, patients who underwent FIR therapy exhibited significantly better flow rates than patients in a control group (no FIR). Results indicated that noticeable differences occurred after just one treatment, and encouraging performance continued for one year of FIR therapy.

2.4.2.3 Discussion

The underlying physical mechanism ascribed to the success of FIR is has not yet been definitively determined. There have been numerous theories presented regarding the effect of laser irradiation on cellular processes, but in these conditions, following Occam's razor, the most probable mechanism is radiative heating. This suggests that heating by other means such as ultrasound could have similar effects on NH. Focused ultrasound, in addition, could provide selective heating by focusing and leveraging favorable acoustic properties.

2.5 Conclusions

The literature presented in this chapter provides a solid foundation for the pursuit of an ultrasonic therapy to prevent or inhibit neointimal hyperplastic growth in vascular grafts. The research suggests that there may be thermal as well as nonthermal effects of ultrasound on the cells that make up hyperplasia in vascular grafts. In addition, there have been therapies in the same arena using thermal and nonthermal ultrasound that have exhibited success in inhibiting hyperplastic growth in stents and fistulae, although the experimental research in this thesis does not cover those issues.

CHAPTER 3

ACOUSTIC PROPERTIES OF RINGED ePTFE

3.1 Abstract

Purpose: There are significant variations in the literature regarding the acoustic properties of ePTFE. This study measures acoustic properties of ePTFE and provides explanation for the differences in published values. Benefits and limitations of the known-substrate, cutback, and single-sample methods are presented, especially for thin samples.

Methods: Using the known-substrate method, the speed of sound (c), density (ρ), acoustic impedance (Z), and attenuation (α) were measured. Measurements were performed on an ePTFE sample soaked in a water bath, evacuated in a water bath, and evacuated in an alcohol bath.

Results: ePTFE acoustic properties in a water bath: c = 1467 m/s, Z = 0.478 MRayl, ρ = 326 kg/m^3, α = 1.78 Np/cm·MHz; evacuated in a water bath: c = 1442 m/s, Z = 1.17 MRayl, ρ = 811 kg/m^3, α = 2.41 Np/cm·MHz; evacuated in an alcohol bath: c = 1075 m/s, Z = 1.49 MRayl, ρ = 1382 kg/m^3, α = 0.77 Np/cm·MHz.

Conclusion: The bulk acoustic properties of ePTFE are heavily dependent on the solution in which the sample is immersed. The extrusion process used to produce ePTFE

can be engineered to produce a wide range of values for bulk density and porosity. The presence of pores is a likely explanation for why the immersing medium causes a wide variation in acoustic properties.

3.2 Introduction

Acoustic wave propagation is theoretically governed by the densities, speeds of sound, and the values of acoustic attenuation of the concerned media. These quantities are derived from the mechanical properties of a medium. Most biological tissues, excepting bone and calcific deposits, are classified as fluid media; shear waves are damped so rapidly that they are not considered in analysis. Only pressure waves, waves whose displacement is in the direction of travel, are taken into account in most acoustic wave formulae describing motion in soft biological tissue. The phase velocity, or speed of sound, of a fluid medium is a result of its bulk modulus and density. Acoustic attenuation is a quantity that represents acoustic absorption, due to a material's viscosity, and acoustic scattering, due to a material's local deviations from homogeny. In order to invoke a therapy based on acoustic wave propagation, it is requisite that the relevant mechanical properties, herein termed acoustic properties, be understood.

There are accepted, average values for the acoustic properties of the biological tissues (muscle, fat, blood, venous tissue, and skin) through which ultrasound must be transmitted to reach an implanted vascular access. In contrast, only two studies have been conducted with the intent to examine the acoustic properties of synthetic ePTFE [3] [48] used for vascular access. The two studies came to divergent conclusions regarding the speed of sound, density, and acoustic impedance of the material. The intent of this

study is to: (1) give reason and explanation for the differences between [3] and [48], and (2) determine the acoustically relevant properties of the ePTFE in ringed vascular grafts. These properties will then be used in the numerical simulations of Chapter 4

3.3 Methods and Results

3.3.1 Acoustic Property Measurement Methods

3.3.1.1 Cutback Method

The most common method for measuring the acoustic properties of a material is the cutback method. This involves measuring the speed of sound and transmission signal magnitude through a thick piece of the material, cutting the sample to a smaller thickness and measuring the same parameters again. A variation involves using two samples of the same material with differing thicknesses where one of the samples is not a derivative of the other. From these measurements, the speed of sound and attenuation can be determined. The cutback method, as presented here, involves coupling the test transducers directly to the sample. Another common version of the cutback method involves placing the sample(s) in liquid medium with well-known acoustic properties. In the latter case, the measurements are dependent on the accuracy of the acoustic properties of the well-known medium, but transducers do not have to be moved while replacing the samples of different thicknesses. That version is also useful for samples that may deform under the pressure from coupling. In the case of ePTFE, the version of the cutback method presented here involves fewer external dependencies and is therefore used for comparison to other methods.

It is important to note that the measurement of the speed of sound and the

measurement of the attenuation of the material of interest do not depend on values for the speed of sound of a coupling medium, assuming that the coupling medium has negligible thickness. Neither are the measurements dependent on the density of the sample or absolute sound pressure level calibration of the test transducers (as long as the same set of transducers is used for both tests).

Care must be taken to prepare the sample with smooth, flat, parallel faces and position the transducers such that the beam is perpendicular to the sample faces. Subsequently, when calculating acoustic impedance using the speed of sound as determined by the cutback method, the density of the sample must be determined independently using Archimedes' principle for example.

When a sample is so small that it cannot be reliably be cut to a smaller thickness, or its properties are dependent on the thickness, i.e., the thick and thin samples are not be from the same extrusion manufacturing process, the experimenter is left to methods which are dependent on other known or published values, like the single-sample method described next.

3.3.1.2 Single-Sample Method

The single-sample method used in [3] involves measuring transmission through a sample and comparing the results to transmission through water. This requires calculating the reflection coefficient, Γ, between the transmission medium and the material of interest, with Γ defined as

$$\Gamma_{a-b} = \frac{Z_b - Z_a}{Z_b + Z_a}. \tag{1}$$

where Z_a and Z_b are the acoustic impedances of materials at an interface where

transmission begins in material a, water in the case of [3] , and propagates to material b, ePTFE in [3]. Note that as the acoustic impedances of *a* and *b* become dissimilar, the magnitude of the reflection coefficient increases. The acoustic impedance is defined by

$$Z = \rho c \tag{2}$$

where c is the speed of sound in m/s and ρ is the density in kg/m^3.

The acoustic attenuation, α, commonly measured in Np/cm·MHz, is defined as

$$\alpha = \frac{log_e\left(\frac{|\,p_i\,|}{|\,p_o\,|}\right)}{f_{MHz}d} \tag{3}$$

where $|\,p_i\,|$ and $|\,p_o\,|$ are the amplitudes of the pressure at an arbitrary input plane and output plane, respectively, d is the transmission length between the input and output planes in cm, and f_{MHz} is the operating frequency in MHz. The input and output planes are usually the front and back faces of the sample material. The reflection coefficients are defined by the acoustic impedance mismatch on either side of these planes.

In the case of the single-sample, method the attenuation in Np/cm·MHz is calculated by

$$\alpha = log_e\left(\frac{|1-\Gamma_{tm-sample}|^2|\,p_{tm}\,|}{|\,p_{sample}\,|}\right)\frac{1}{df_{MHz}} \tag{4}$$

where *tm* signifies the transmission medium or coupling medium in which the tests are performed, p_{tm} is the acoustic pressure measured at the receiver when the beam travels through the transmission medium and p_{sample} is the acoustic pressure measured at the receiver when the beam travels through the sample. The coupling medium is usually water but ultrasonic coupling gel, alcohol, or other media can be used.

The accuracy of the single-sample method is influenced primarily by the ability to accurately estimate $\Gamma_{tm-sample}$ which is a function of Z_{sample}. To determine Z_{sample}, c is acquired during the test and ρ is determined by some other approach, usually Archimedes' principle. Additionally, because most transducers have a matching layer on the transmission face, the test is also subject to a correct measurement of the travel time through the matching layers of both the transmitting and receiving transducers.

3.3.1.3 Known-Substrate Method

The substrate method presented in [48] allows the measurement of Z, c, α, d, and ρ in one experimental setup but requires that the parameters Z, c, and ρ of a reflective substrate material are known. A good ultrasonic reflector is a practical substrate material choice. The substrate should also have well-known density and speed of sound (i.e., brass or a common grade of stainless steel). The method proceeds as follows:

- The substrate and the thin sample are prepared with smooth, flat faces. The substrate is sufficiently thick to prevent reflections from its far face from interfering with reflections from the sample. The sample is attached on the substrate, leaving enough room of bare substrate area to acquire measurements in a number of locations. The substrate is placed in a test fixture which maintains perpendicularity to the acoustic beam of the test transducer and a fixed distance to the transducer.
- As a reference, reflections are measured (amplitude and transit time) from a bare substrate through the transmission medium.

- Reflections (amplitude and transit time) are measured from the sample-substrate combination through the transmission medium. A diagram of the reflections can be seen in Figure 3.
- Using the amplitudes and transit times measured, the speeds of sound and reflection coefficients can be calculated.
- The acoustic impedance can then be calculated from the reflection coefficient.

p_{in} is the incident pressure wave pulse. It is analogous to p_{tm} in (4). p_{in} has a peak amplitude, A_{in}, and is initiated at time $t = 0$. p_0 is the received pressure wave echo from the bare substrate. p_1 is the first pressure wave echo received when transmitting over the sample. It is due to the reflection from the transmission-medium-to-sample interface. p_2 is the second echo received when transmitting over the sample. It is due to the reflection from the sample-substrate interface. In Figure 3, p_2' is shown to indicate energy loss when p_2 crosses the sample-to-transmission-medium interface when returning to the transceiver. p_0, p_1, and p_2 have peak amplitudes A_0, A_1, and A_2, respectively.

The equations to determine the thickness of the sample, *d*, and the speed of sound of the sample are:

$$d = \frac{1}{2}(t_0 - t_1)c_{tm} \tag{5}$$

where c_{tm} is the speed of sound in the transmission medium,

$$c = c_{tm}\frac{t_0 - t_1}{t_2 - t_1} \tag{6}$$

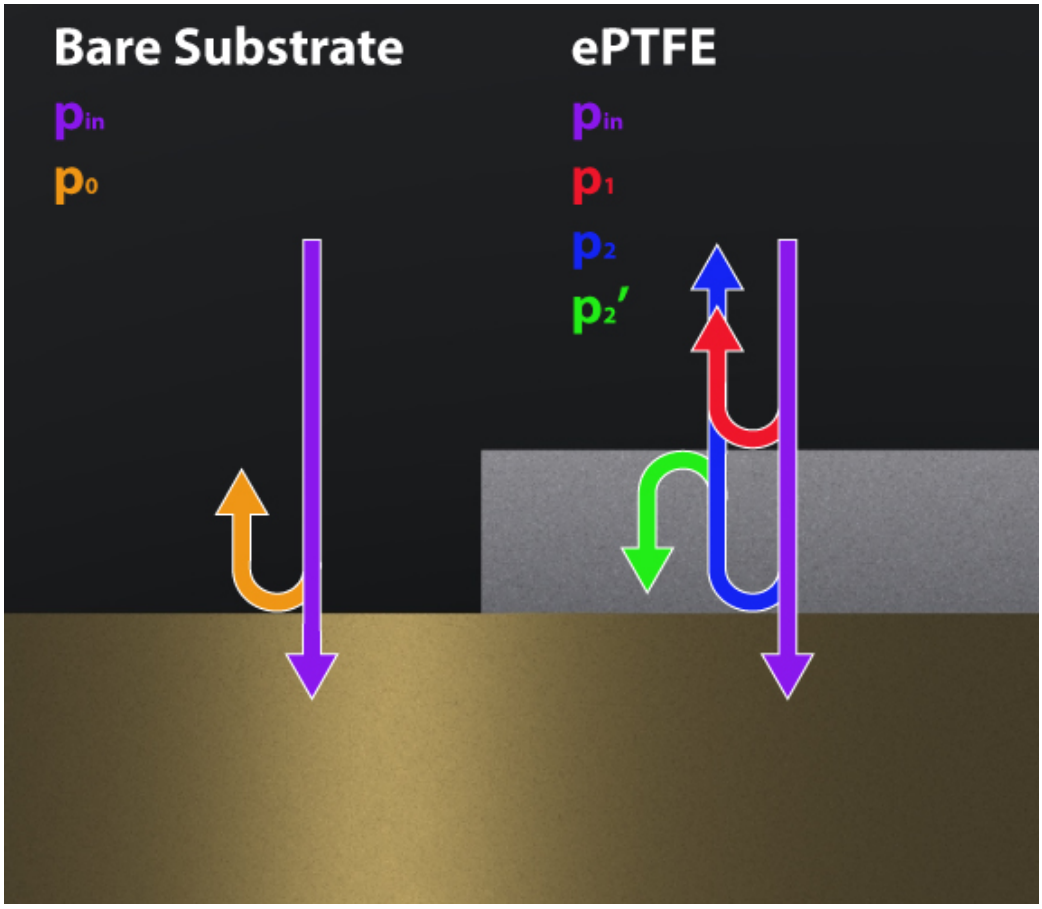

Figure 3. Diagram of reflections in the known-substrate method.

where c is the speed of sound of the sample and t_n is the arrival time of the pressure wave, p_n.

To begin calculations to find the various reflection coefficients, a reference, A_{in}, representing the peak amplitude of the pressure of the acoustic wave before any reflections at the sample or the substrate must be defined:

$$A_{in} = \frac{A_0}{|\Gamma_{tm-sub}|}. \tag{7}$$

If the transceiver transducer is not calibrated to infer actual pressure from

measured voltage for transmission and reception at the desired operating frequency and temperature and with the proposed transmission media, the various amplitudes are measured in units of volts, although they are representative of units of pressure.

Once A_{in} is found, the magnitude of the reflection coefficient at the sample-to-medium interface can be calculated:

$$\left|\Gamma_{tm-samp}\right| = \frac{A_1}{A_{in}}. \tag{8}$$

Note that as long as A_1 and A_{in} are unsigned values, only the magnitude of $\Gamma_{tm-samp}$ can be calculated. It is often the case that the phase of the reflection coefficient is uncertain in manual detection schemes and almost always the case for threshold detection. The employment of more sophisticated DSP algorithms can provide more phase information, but for reasons that will be seen in the discussion section, this thesis will consider the phase of the reflection coefficient to be unknown at this stage in the calculations.

Knowing only the magnitude of the reflection coefficient, there are two possible Z values:

$$Z = Z_{tm}\frac{1 \pm \left|\Gamma_{tm}\right|}{1 \mp \left|\Gamma_{tm}\right|}. \tag{9}$$

In one case $Z > Z_{tm}$ and in the other $Z < Z_{tm}$. Unless the transmission medium and the sample have very similar properties, qualitative observation, for instance whether or not the sample floats in the immersing medium, regarding which medium is denser can lead to quantification of Z. If that fact is not apparently obvious, phase of the reflection coefficient must be determined to determine the correct value of *Z*.

Once Z is known, the density of the sample can then be calculated:

$$\rho = \frac{Z}{c}. \tag{10}$$

Once a determination is made for the value of Z_{samp}, the magnitude of the reflection coefficient, $\Gamma_{samp-sub}$ can be calculated by (1). Assuming negligible attenuation in the transmission medium, A_2 can be defined:

$$A_2 = A_{in}\left(1-\left|\Gamma_{tm-samp}\right|\right)^2\left(1-\left|\Gamma_{samp-sub}\right|\right)e^{-2d\alpha} \tag{11}$$

Solving (11) for α yields:

$$\alpha = log_e\left[\frac{A_2}{A_{in}}\left(\frac{1}{\left(1-\left|\Gamma_{tm-samp}\right|\right)^2\left(1-\left|\Gamma_{samp-sub}\right|\right)}\right)\right]\frac{1}{2d}. \tag{12}$$

α of (12) can be modified to include a linear dependence on frequency with units of Np/cm·MHz:

$$\alpha = log_e\left[\frac{A_2}{A_{in}}\left(\frac{1}{\left(1-\left|\Gamma_{tm-samp}\right|\right)^2\left(1-\left|\Gamma_{samp-sub}\right|\right)}\right)\right]\frac{1}{2\,f_{MHz}d}. \tag{13}$$

3.3.2 Measuring ePTFE Properties with the Known-Substrate Method

3.3.2.1 Experimental Setup

In [48], a numerically controlled scanning acoustic microscope was used to acquire measurements. During the set of experiments performed in this thesis, general laboratory equipment and generic fixturing were used. A brass substrate was constructed from a 4-inch-diameter pipe cap. The inside was milled flat and polished smooth to remove machining marks. A reservoir made from plastic housing was mounted on the

brass substrate and sealed and secured with silicone grease. The rings were removed from a 1-cm section of ringed ePTFE graft. The graft was cut radially, and then slices were cut 3 cm in length and approximately 4-mm wide. One slice at a time was attached to the brass substrate with 5-minute epoxy. The graft was held flat and under pressure for at least 15 minutes while curing.

Measurements were acquired with a 10-MHz A-Probe (Constantine Technologies, LLC, Salt Lake City, UT). The sensor had an active element 4.7 mm in diameter and a focal point of 25 mm. The A-Probe was driven with a 200-V negative pulse generated by an Olympus 5077PR pulser-receiver. The receive channel of the pulser was connected to a Tektronix TDS 2014C oscilloscope, which was triggered externally from the pulser's sync output.

The substrate and fluid container were placed on a 3-axis, linear translational stage. The A-Probe was mounted on a tilt micropositioner pointing down at the substrate. The tilt stage was adjusted to produce maximum received amplitude, indicating perpendicularity of the beam to the substrate. The standoff distance of the A-Probe was adjusted to the focal point by locating maximum received amplitude after perpendicularity. To verify flatness of the substrate and perpendicularity between the acoustic beam and the substrate, the translational stage was maneuvered along both axes perpendicular to the beam to check that the transit-time of the received signal remained constant over an area of bare substrate. An image of the test setup is found in Figure 4.

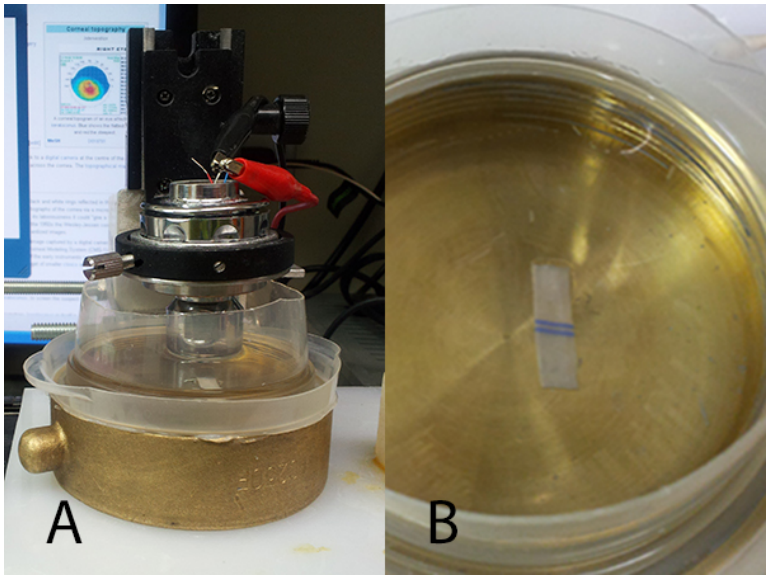

Figure 4. Known-substrate method test fixture. A. Substrate on translational positioning stage. B. ePTFE sample bonded to substrate.

3.3.2.2 Transmission Media

Because ePTFE is a porous, hydrophobic material, the transmission medium is an important consideration. ePTFE readily absorbs some media like alcohols, but not water. Prior to acoustic experiments, some brief observations were made to this point.

> *A sliced sample of ePTFE was weighed dry. Its volume was measured in water by Archimedes' principle, then its mass was measured on a precision balance. The slice was then placed in a water/alcohol mixture. Its mass was measured again. The slice was completely dried, then submerged in pure methanol and the measurements were repeated.*

Table 1 contains these results. The translucency is illustrated in Figure 5.

These observations lead to three test conditions used in the known-substrate method: (1) sample soaked in water, (2) sample evacuated in water, and (3) sample evacuated in alcohol. In the first case, the sample was allowed to soak in water for approximately one hour before testing. In the second and third cases, the sample sub-

Table 1. Bulk density of ePTFE in various media

	Mass (g)	Density (kg/m^3)
Unsoaked	.293	651
Alcohol and Water (40% Alcohol by Volume)	.392	871
Pure Methanol	.494	1098

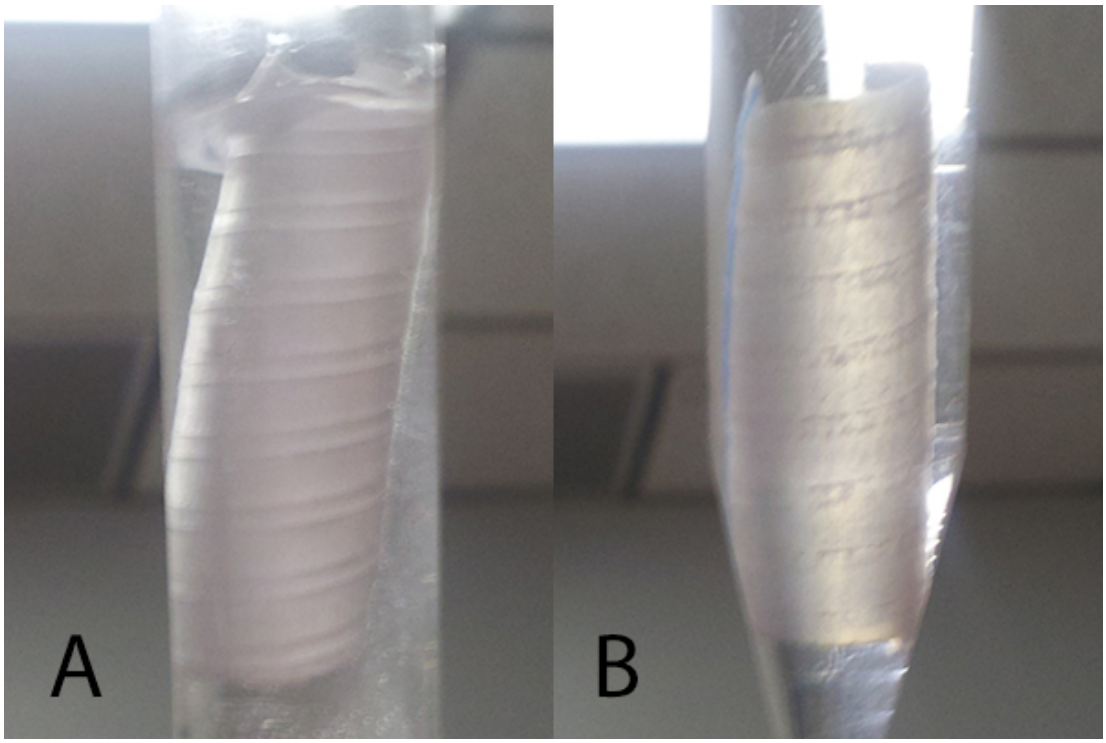

Figure 5. Translucency of ePTFE in water and methanol. A. Water: opaque sample, floating in medium. B. Pure methanol: translucent sample, denser than medium.

merged in the respective medium was put under a vacuum of 25 mmHg for two minutes.

Arrival times were measured manually by the threshold method in combination with zero-crossing observation. The detection process followed these instructions:

- Set the oscilloscope trigger averages to a maximum (128 on the TDS2014C).
- At an analog-to-digital converter (ADC) gain at which the whole envelope of the signal can be seen, find an approximate arrival time using the oscilloscope cursors.
- Maximize the ADC gain then find the first peak above the noise floor.
- From the time values of the subsequent 3-4 zero crossings, calculate the average half-period.
- Project that half-period time value forward from the first of the zero-crossings after the first peak to determine arrival time.

Amplitudes were measured with the scope peak-to-peak amplitude measurement function. A typical screen capture from the oscilloscope can be seen in Figure 6. Measurements were taken at five locations along the graft sample by adjusting the translation stage. Care was taken to steer clear of the ridges where the rings had been attached because the method of attaching the rings to the graft was unknown. Additionally, the areas where the sample was bonded to the substrate were avoided. Tables containing the reference mechanical and acoustic properties and the measured properties can be found in Table 2 and Table 3, respectively. Property values for alcohol, water, and brass were obtained from through-transmission measurements performed by Constantine Technologies, LLC in Salt Lake City, UT.

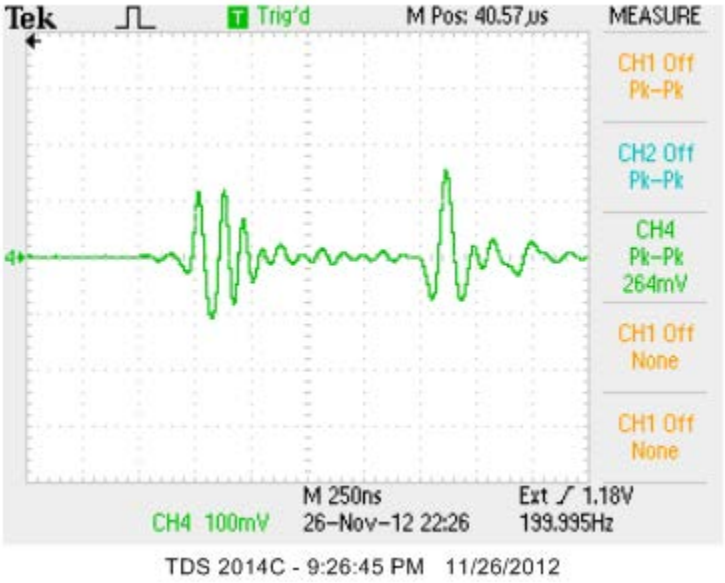

Figure 6. Oscilloscope screen-capture showing p1 (left-most envelope) and p2 (right-most envelope) (see Figure 4). Measurements were taken through a typical ePTFE sample attached to the brass substrate submerged in alcohol.

3.4 Discussion

3.4.1 ePTFE Material Properties

The results indicate that the acoustic properties of ePTFE are in large part dependent upon the immersing medium. This is probably due to the porous, hydrophobic nature of ePTFE. ePTFE is created from PTFE by an extrusion process that stretches the material rapidly. The temperature, pressure, and tooling size can be adjusted to create a range of densities and porosities in ePTFE. A nonporous, full-density fiber has a density of approximately 2100 kg/m^3, while a low-density version can have a pore volume of 90% and an apparent bulk density of only 200 kg/m^3 [49]. This means that in clinical

Table 2. Input acoustic property values for the known-substrate method.

	$c(m/s)$	$\rho(kg/m^3)$	$Z(MRayl)$
Water	1500	1000	1.5
Alcohol	1225	792	.970
Brass	3475	8730	30.3

Table 3. ePTFE mechanical properties as measured with the known-substrate method.

	$d(mm)$	$c(m/s)$	$Z(MRayl)$	$\rho(kg/m^3)$	$\alpha(Np/cm{\cdot}MHz)$
Water Soaked	$0.638 \pm 1.35 \times 10^{-2}$	1467 ± 33	$0.478 \pm 1.43 \times 10^{-2}$	326 ± 16.8	1.78 ± 0.111
Water Evacuated	$0.638 \pm 3.65 \times 10^{-2}$	1442 ± 14	$1.17 \pm 6.66 \times 10^{-2}$	811 ± 42.7	2.41 ± 0.24
Alcohol Evacuated	$0.624 \pm 3.93 \times 10^{-2}$	1075 ± 22	1.49 ± 0.149	1382 ± 158	$0.77 \pm 1.1 \times 10^{-2}$

practice, the consistency of acoustic properties of ePTFE grafts would be tied to the consistency in manufacturing processes between ePTFE graft manufacturers.

Attenuation in a homogenous material can be predominantly attributed to absorption as a result of viscosity. In contrast, in a porous material like the ePTFE graft, attenuation due to scattering and refraction within the material cannot be omitted. The different values of attenuation measured in ePTFE in Table 3 may be evidence of variations in attenuation due to scattering and refraction. Because the peak reflection amplitude, A_1, was smallest in the alcohol-evacuated sample, it is likely that this sample is the one most representative of attenuation due to absorption in the PTFE fibrils. If the ePTFE pore volume had a substantial amount of air in the water-soaked and water-evaporated samples, there would be much more scattering. The attenuation measured in those samples is a combination of absorption in PTFE fibrils and scattering and refraction away from the beam.

3.4.1.1 Comparison to Vickers [3]

The measured properties in this study agree partially with [3] (see values in Table 4). The measurements in [3] were made with a 6-mm block of ePTFE using the single-sample method in water but after the ePTFE sample was wetted in a solution of 95% by volume ethanol-to-water. The density measurement method was not clear. The closest correlation to this study is found in the evacuated alcohol measurements. The α values are identical to the degree of standard deviation reported, and the c value falls in between water and alcohol, which likely corresponds to the alcohol-wetted sample being placed in a water bath. The density value is approximately 10% lower than the density

Table 4. ePTFE acoustic properties reported by Vickers in [4] and Jørgensen in [48].

	***c* (m/s)**	***ρ*** *(kg/m^3)*	***α*** *(Np/cm·MHz)*
Vickers	1237	1230	.77
Jørgensen	1111	3360	.166

measured in this study. This could be a result from variations in the manufacturing processes of two different grades of ePTFE. It is also possible that the difference could be a result of not evacuating the ePTFE sample in [3] as none was reported.

3.4.1.2 Comparison to Jørgensen [48]

In [48], Gore Stretch ePTFE was used as opposed to nonstretch graft material, so some possible variations in the material properties between this thesis and [3] were expected. The values reported by Jørgensen *et al.* can be found in [48]. Experiments were performed in a bath of pure ethanol. Comparison to the results of this study's experiment in evacuated alcohol show close agreement on the c value but very significant differences in the values of Z and ρ and α. Noting that the density value is over 150% of the manufacturer's full-density specification, it is the author's opinion that this discordance can be attributed to either mathematical or experimental error, as explained below.

As pointed out during the description of the known-substrate method, the phase of reflection coefficient could be measured inaccurately, especially if using a manual

threshold detection technique. A potential experimental error could occur; if there happened to be one half-cycle of the incoming pressure wave signal under the noise floor before arrival detection, the measured phase would be inaccurate by 180˚, leading to a sign-reversal in the reflection coefficient. The recorded arrival time, however, would only suffer by half the period of the fundamental frequency. The sign-reversal in the reflection coefficient would lead to an incorrect Z value in Equation (9). When using a threshold detection method, it is better to measure unsigned amplitudes and then calculate Z with the aid of a qualitative density observation.

Trying the theory that the sign of the reflection coefficient was reversed in [48] leads to a Z of .255 MRayl (instead of 3.73 MRayl from the published ρ and c) and subsequently a ρ of 230 kg/m^3. Neither set of values agree well with this study's alcohol evacuated test, but the latter falls within the manufacturer's specifications [49].

Another likely source of error in [48] is mathematical. The author does not describe the calculation of a reference signal, A_{in}. If the reflection coefficient were incorrectly defined as

$$|\Gamma_{tm-samp}| = \frac{A_1}{A_0}, \tag{14}$$

instead of the definition in (8), the Jørgensen's calculations for Z and ρ can be reproduced. Using the correct definition of the reflection coefficient in conjunction with Jørgensen's data values (including the PMMA substrate), the two possibilities for acoustic impedance are calculated to be 1.86 MRayl and 0.46 MRayl. The resulting two density possibilities are 1670 kg/m^3 and 410 kg/m^3, respectively. These are both within the manufacturer's specification for ePTFE. Those densities, in turn, lead to

attenuation values of 1.2 Np/cm·MHz and 2.7 Np/cm·MHz, respectively. The densities and attenuation values are all in closer agreement with this study and with Vickers when using this calculation method.

The qualitative observations of ePTFE density compared to water and compared to alcohol are of interest as well. Jørgensen reports a bulk density of ePTFE that is greater than water and would therefore sink in a water bath. That was not the observation of the sample used in this thesis. Additionally, the reported density value is 50% larger than common published book values for unextruded PTFE. It seems very unlikely that the output material of an extrusion process would be a denser than the material input to that process.

A third potential source of error is the preparation of the sample. Aside from the cutting method, [49] did not record any information about sample preparation. In this study, care was taken to evacuate the samples (excepting the water-soaked sample) to remove air in the ePTFE pore volume. A substantial amount of air left in the pore volume would lead to a dramatically lower density measurement. This in conjunction with the potential mathematical error described above could be behind the discrepancy in [49].

In addition to removing air for the sample pore volume, care must be taken to avoid measurements near areas where the sample is bonded to the substrate. In this study, qualitative observations were made that showed much greater reflection coefficients near bonding areas. This is due to the bonding agent being absorbed into the pore volume of the sample and then curing and hardening in that location. In [49], bonding was reported to be at the ends of the sample, but the location of testing relative to the end of the sample

was not clearly indicated. Measurements taken in bonding areas would not be representative of bulk ePTFE properties. Density measurements would be greater and speed of sound measurements would also likely be greater because the speed of sound in the cyanoacrylate is faster than PTFE.

3.5 Biological Conclusions

Noting the material property dependence on the transmission medium and manufacturing process, it becomes increasingly important to understand the ePTFE graft in biological context in order to make judgments about acoustic properties. A detailed consideration of the cellular processes as an *in vivo* implanted graft matures is out of the context of this work, but a brief note can be made. Several studies indicate that over the course of a few weeks, and depending on the porosity of the sample and location of the prosthesis, cells and biological material will infiltrate ePTFE membranes [50] [51] [52]. This suggests that early in the course of a graft lifetime, ePTFE pores will begin to be cellular/biological materials. As this happens, the acoustic impedance of the graft will become progressively similar to the surrounding tissue. It is therefore reasonable to consider the three cases examined in this study as acoustic models for an ePTFE graft at various stages of maturity.

CHAPTER 4

SIMULATIONS AND *IN VITRO* PHYSICAL MODELS OF RINGED GRAFTS

4.1 Abstract

Purpose: To ensure adequate but not excessive ultrasonic heating, power deposition and the corresponding heat rise must be modeled and simulated in ringed ePTFE vascular grafts before proceeding to clinical experiments.

Methods: Ultrasonic power deposition was simulated with three sets of acoustic properties (see Chapter 3), two graft geometries, and two beam foci. Simulations were performed with the Hybrid Angular Spectrum (HAS) algorithm using MATLAB. The thermal reaction is simulated using the Finite Element Method in COMSOL Multiphysics. Simulations were verified by a thermocouple-implanted tissue phantom model and using magnetic resonance temperature imaging (MRTI).

Results: Power deposition varied in the walls of the graft significantly depending on the ePTFE graft acoustic properties. The resulting heating patterns were likewise affected. The rings in ePTFE grafts were an acoustically significant feature leading to beam refraction and absorption.

Conclusion: Graft heating in ringed ePTFE grafts sufficient to potentially inhibit or prevent neointimal hyperplasia is possible, but controlling heating reliably requires *in*

vivo studies of graft acoustic properties.

4.2 Introduction

It has been shown that neointimal hyperplasia can potentially be inhibited or prevented by mild, ultrasound-induced hyperthermia [2]. The reliability of delivering known temperature doses in such a treatment is critical. Although it can be done in an MRI, in a practical clinical setting, it is not possible to directly monitor subsurface temperature noninvasively. Additionally, in the case of high-intensity focused ultrasound (HIFU), subsurface temperatures cannot be easily inferred from surface temperatures because the focus of the incident beam is usually subdermal. In order to develop a safe, reliable treatment, subsurface temperature must be predicted based on electrical power readings from ultrasound instrumentation and information about the efficiency of the transducer converting electrical power to acoustic power. Making the leap to therapeutic effectiveness and safety requires a detailed foreknowledge about the acoustic and thermal traits of the biological and synthetic materials to be treated. This chapter will be concerned with the acquisition of data sufficient to produce a reliable *in vivo* thermal treatment for ringed ePTFE grafts by numerical simulation and physical phantom models.

Numerical simulation of ultrasound necessitates solving the acoustic wave equation. The acoustic wave equation can be modeled using any number of numerical techniques to predict acoustic pressure patterns and power deposition in a physical domain. This study employed the hybrid angular spectrum (HAS) [53, 54] computed with MATLAB. Thermal rise due to ultrasound is a result of ultrasonic power deposition. The power deposition in a material is a function of the incident acoustic

pressure and the acoustic absorption of the material. With known power deposition and material thermal properties, commercial modeling packages such as COMSOL Multiphysics can be used to estimate the thermal response due to deposited power.

To be practical, numerical models are incomplete. Intricate geometrical details or less-than-dominant physical phenomena are simplified or omitted entirely to enable convergence with finite computational resources. Therefore, prior to clinical trials or *in vivo* experiments, it is always informative to perform material experiments with lifelike geometry and substance.

In a physical phantom model, it is almost impossible to place hydrophones in the model to measure ultrasonic power deposition at enough data points to confirm acoustic propagation simulation results independently. Even if it were possible to fit a sufficient number of hydrophones in the model, they would likely interfere with the beam's propagation. Temperature, however, can be measured with enough spatial resolution to draw conclusions about the results of a thermal simulation in a domain with geometrical features on the order of a graft and bulk hyperplastic growth. So, rather than evaluating the reliability of a simulation following its incremental stages, the end thermal results and predictions must be contrasted and inferences made about acoustic power deposition.

In these experiments, the method chosen to measure temperature had to be compatible with an ultrasonic transducer running nearby, but could not interfere with the ultrasound beam. The method also had to be capable of gathering readings below the model surface. Two suitable methods were chosen: implanted thermocouples and real-time temperature mapping using magnetic resonance temperature imaging (MRTI).

4.3 Methods and Results

4.3.1 Building the Numerical Models

Simulations were performed in two phases: first, the acoustic wave propagation and second, the heat transfer. The acoustic wave simulations were performed with HAS. HAS requires a regularly spaced grid describing the discretization of model geometry and material properties. COMSOL Multiphysics, used for temperature simulations, requires a finite-element representation of model geometry and properties. The interface between these two representations is described in Appendix B.

Models were originally drafted using SolidWorks®. The following were modeled as SolidWorks parts: a bare graft, the graft rings, hyperplasia in the graft lumen, and water in the graft lumen. The parts were mated together in a SolidWorks assembly. The assembly can be seen in Figure 7. A mechanical drawing of the assembly with relevant dimensions can be found in Appendix C. In the case of HAS, the computational domain was created by the interface described in detail in Appendix B. Briefly, the model was

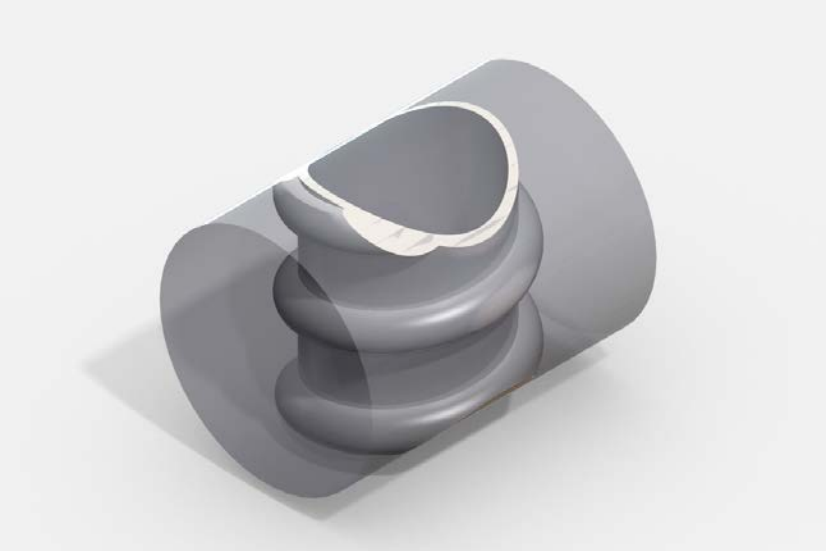

Figure 7. SolidWorks graft model and cylindrical computational domain.

discretized into a volumetric, tetrahedral mesh using the SolidWorks Simulation Add-in. The mesh was then converted to a regularly spaced Cartesian grid.

For COMSOL, a cube or cylinder was modeled to contain the graft assembly in a computational domain. The assembly and parts were then loaded into COMSOL via the SolidWorks LiveLink interface. In COMSOL, the geometry was verified and each imported domain was assigned the correct material.

4.3.2 HAS Acoustic Simulations

4.3.2.1 HAS Overview

The Hybrid Angular Spectrum method derives from the traditional angular spectrum method. In the traditional angular spectrum method, the propagation of sound is treated as a superposition of plane waves with different wave vectors. The Fourier transform is used to compute the sound pressure fields in the spatial-frequency domain [55]. The angular spectrum method, however, lacks the ability to account for inhomogeneous media between the input and output planes. The HAS method accounts for inhomogeneity by discretizing the computational medium. At each discrete plane, the propagating wave is multiplied by an attenuation term and phase shift term in the spatial domain. The attenuation and phase shift terms are not required to be homogenous over a given plane. The wave is then transformed into the spatial-frequency domain, propagated by the angular spectrum to the next plane and transformed back to the spatial domain. The process is repeated until the wave propagates through the domain. At each planar step, the reflection is calculated. After the “forward wave” transmits through the whole domain, the “backward wave” propagates in the reverse direction starting with a

magnitude of zero and adding the reflections iteratively at each interface [53] [54].

The method has a distinct advantage over traditional methods like the finite-element or finite-difference time-domain methods in the use of computational resources. The finite-difference time-domain method is limited by the necessity of time-discretization and resolution. The finite-element method suffers from the requirement of solving large systems of potentially nonlinear equations, leading to costly matrix inversion or pseudo-inversion. The computational bottleneck of the HAS algorithm is calculating Fourier transforms, which, in comparison with time-discretization and matrix inversion, is computationally cost-effective.

The HAS algorithm, unlike the traditional angular spectrum, is limited by the requirement to fulfill the Nyquist criterion in the spatial discretization. Finite-difference time-domain has this requirement. It should be noted also that the HAS algorithm has not yet been adapted to address transient response simulations.

4.3.2.2 HAS Input

The input to the HAS algorithm is an arbitrary complex pressure on one planar boundary of the computational domain. Because the transducers used in HIFU are curved, a secondary method must be used to calculate the resultant pressure at a plane a distance away from the transducer. The pressure on the input plane was calculated by discretizing and directly integrating the Rayleigh-Sommerfeld integral. This was done using MATLAB with code developed by Dr. Douglas A. Christensen at the University of Utah. Parameters were chosen so that the resultant Rayleigh-Sommerfeld plane matched the resolution of the HAS computational domain.

4.3.2.3 Simulation Profiles

A parameter matrix was constructed based on the three sets of material parameters, two transducer focal point locations, and two geometrical permutations for a total of twelve simulation profiles. The material parameters were held constant except for the density and attenuation values in the graft wall. The three variations in the graft wall were determined by the results of Chapter 3 contained in Table 3. Parameters for the remaining materials can be found in Table 5. The two transducer foci were (1) the middle of the near graft wall and (2) the middle of the far graft wall. Each of the above was considered in two geometries: (1) with the transducer beam passing directly through a winding and (2) with the beam passing directly between two windings.

Attenuation in a homogenous material can be predominantly attributed to absorption as a result of viscosity. This is the case for the tissue phantom and PTFE windings. In Table 5, the attenuations and absorptions of these materials are equal. In contrast, in a porous material like the ePTFE graft, attenuation due to scattering cannot be omitted. In Chapter 3, the transmission was best into the alcohol-evacuated ePTFE sample. It is likely that the attenuation measured in that sample is closest to the value of absorption. For this reason, the value for absorption in ePTFE for all simulations was chosen to be 0.77 Np/cm·MHz.

4.3.3 HAS Simulation Results

The relevant output of the HAS simulation is volume power density, *Q*, typically measured in W/m^3. *Q* is calculated by:

$$Q = \alpha_{abs} \frac{\left| p^2 \right|}{\rho c} \tag{15}$$

Table 5. HAS simulation material parameters.

	$c(m/s)$	$\rho(kg/m^3)$	$\alpha(Np/cm\cdot MHz)$	$\alpha_{abs}(Np/cm\cdot MHz)$
Tissue phantom	1588	950	0.0667	0.0667
Water	1500	1000	0	0
PTFE winding	1413[1]	2170[1]	0.958[1]	0.958[1]
ePTFE graft	----------	See Table 3	----------	0.77

1) Properties from Vickers [3]

where

α_{abs} is the material acoustic absorption,

ρ is material bulk density,

c is speed of sound, and

p is pressure.

Figure 8 contains a matrix of plots of Q at the different geometries, properties, and foci. The simulations indicate that power is deposited readily in the near wall of the graft for all near foci and all ePTFE property variations. In contrast, even when the graft's bulk acoustic properties are most similar to the phantom, there is less than half the power in the focus at the far wall than the focus at the near wall. In the cases of water, where the graft bulk properties are much more dissimilar to the phantom, the Q of the near wall focus and the Q of the far wall focus are dissimilar to a greater extent.

Another telling aspect of the simulations is that when the rings are within the focus of the beam, they absorb and reflect a significant amount of acoustic power. It is

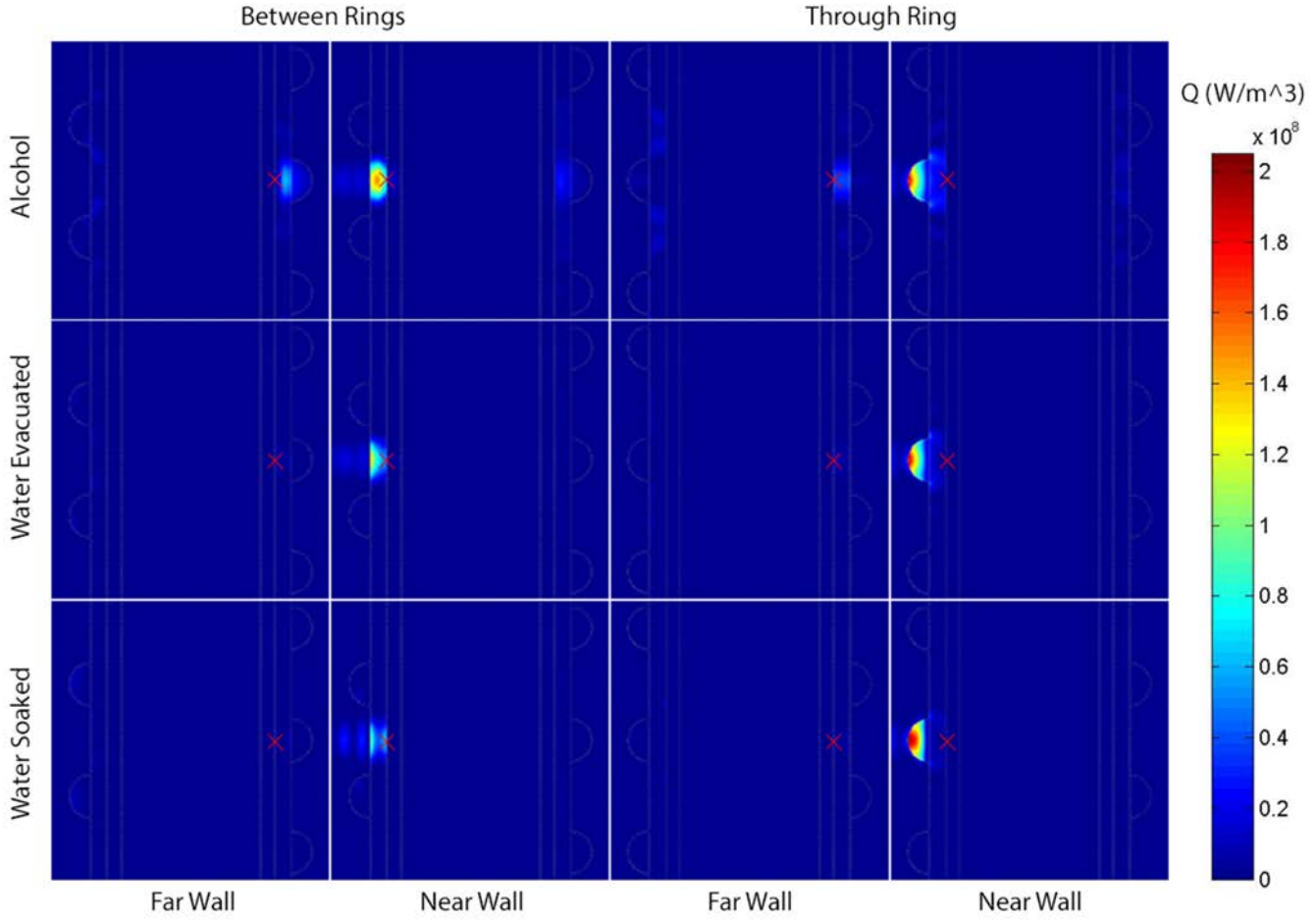

Figure 8. HAS simulation of acoustic power deposition, Q. The image is at a cross-section dissecting the graft at the center of the beam generated from 1 W of acoustic power at the input plane. The beam approaches the domain from the left. Three ePTFE conditions are shown: evacuated in alcohol, evacuated in water, and soaked in water. Two beam paths are shown: beam-through-rings and beam-between-rings. Two foci are shown: near wall and far wall (marked in red).

most apparent when contrasting the two different geometries, with a graft evacuated in alcohol, when the beam focus is on the far wall. In the case in which a ring is in the path of the beam, the beam is refracted at the far wall. When the beam travels between rings, the focus is relatively tight at the far graft wall.

4.3.4 COMSOL Thermal Simulations

Before creating a COMSOL simulation, the Q pattern from the HAS simulations needed to be converted to a COMSOL-compatible format. The "grid" format was chosen. A script was written in MATLAB to export the "grid" format to a .txt file. In addition to exporting, and in order to prevent large, time-consuming file transfer, the script down-sampled the Q pattern from 301x301x301 to 151x151x151. The script is contained in Appendix E.

The material parameters for the thermal simulations are contained in Table 6.

The process for setting up and running a COMSOL simulation followed these steps:

1. Create a 3D COMSOL model with the Bioheat transfer physics interface.
2. Add a time-dependent study step.
3. Import the geometry, created in SolidWorks, with the SolidWorks LiveLink interface.
4. Create materials for ePTFE, PTFE, phantom, and water with respective properties.
    a. Assign each region to a material type.
5. Define an interpolation function for Q import. Name the function Q.

Table 6. COMSOL thermal simulation material parameters.

	Specific Heat Capacity $c_p (J / kg \cdot K)$	Thermal Conductivity $k(W / m \cdot K)$
Tissue phantom	3140[1]	.5[1]
Water	4181	.58
PTFE winding	1300[1]	.35[1]
ePTFE graft	1172[1]	.35[1]

1) Properties from Brinton[2]

a. Select the .txt file created by the conversion script.

In the Bioheat Transfer interface, add a Heat Transfer in Solids and a Heat Transfer in Fluids node.

b. Assign water to the Heat Transfer in Fluids node.

c. Assign other regions to the Heat Transfer in Solids node.

6. Add an Open Boundary node for free heat conduction at the computational domain boundaries.

   a. Assign all computational domain boundaries to the Open Boundary node.

7. Add a Heat Source node.

   a. Assign all boundaries to the Heat Source node.

   b. Using a user-defined general source, specify the Q function as the model input: Q(x[1/mm],y[1/mm],z[1/mm])*0.4*(t<=20). Include a step function to turn the source off after 20 or 30 seconds depending

on simulation profiles. Include a scaling factor for the acoustic power to convert from the general 1-W input (occurring in the equation above as 0.4). Also note that the acoustic power at the initial plane of the computational domain is the not the same as the acoustic power measured from the transducer. A significant amount of attenuation occurs through the phantom before the computational domain begins and must be accounted for. This is done by measuring the distance, *d*, before the computational domain and multiplying incident pressure on the model by the attenuation factor $e^{-2d\alpha}$.

8. Generate a mesh for the computational domain using the physics-controlled mesh option with an element size parameter of "fine."
9. Using the default solver parameters, compute the solution. Solution times ranged from 15-45 minutes on a Windows Server with 32 GB of RAM.
10. Export data in grid format for comparison in MATLAB.

The thermal heating simulations generally followed the spatial pattern of the power deposition. Following intuition, heating occurs where power is deposited. A typical example of heating can be seen in Figure 9. There was negligible heating in the far wall in the cases of grafts soaked and evacuated in water. This was true when the beam was focused at the near wall and at the far wall whether or not there was a ring directly in the path of the beam.

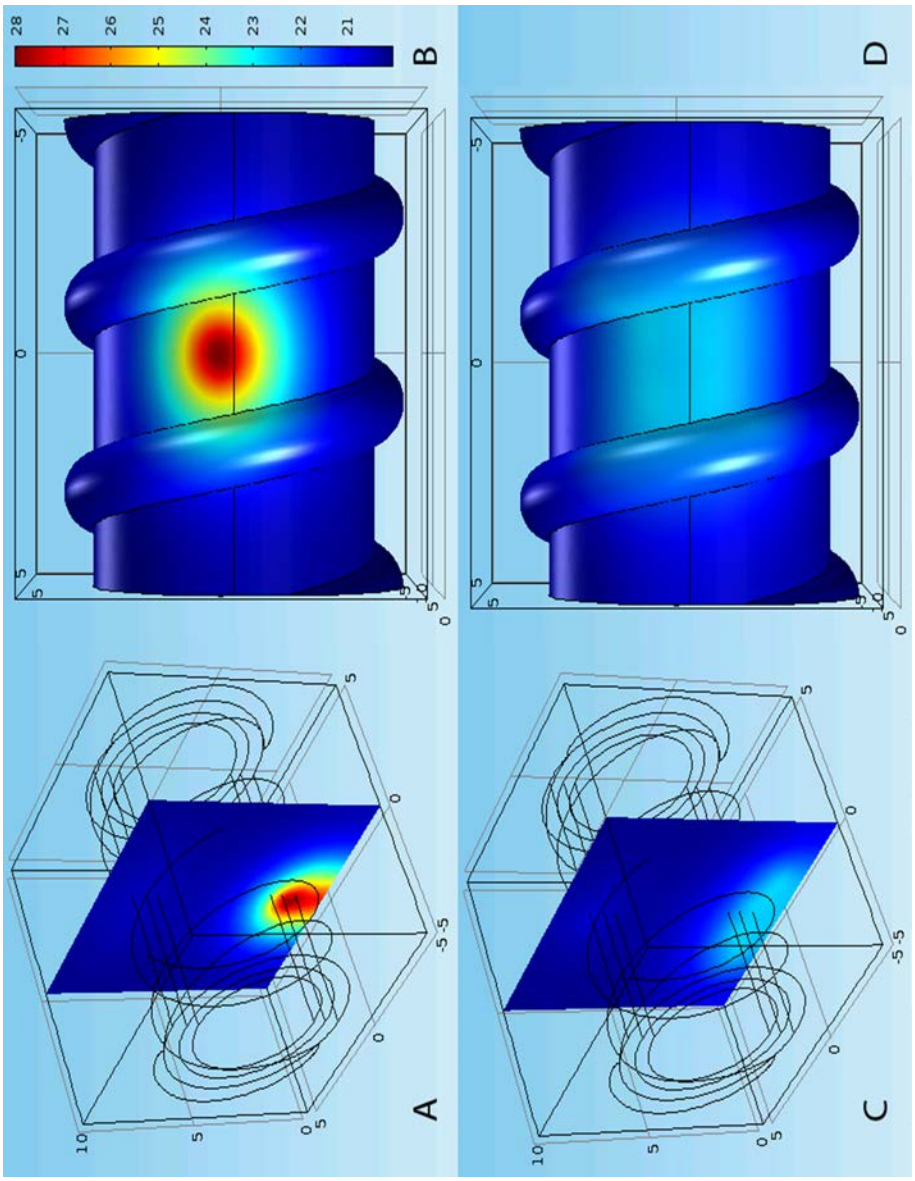

Figure 9. COMSOL simulated heating (in °C) profiles in a graft with water-soaked acoustic parameters. A. Slice with focus at front of graft. B. Heating on near wall of the graft with focus at near wall. C. Slice of heating with focus at far wall of graft. D. Surface of graft at near wall with focus at back. Input acoustic power = 0.4 W. Physical dimensions are in mm.

4.3.5 Building the Physical Phantoms

4.3.5.1 Preparing the Model Housing

Two phantom models of a graft and tissue phantom were built: one with thermocouples and one without thermocouples for use in the MRI. Housings were constructed by beginning with a 7.5-cm polycarbonate cylinder open at both ends. Opposing holes were drilled on either side of the cylinder to allow the ringed graft to traverse the cylinder and protrude out the holes. Holes were placed 2.5 cm from one end and 5 cm from the other. In the case of the thermocouple model, holes were drilled slightly larger to accommodate thermocouple leads. A third hole for filling the housing was drilled 90˚ around the cylinder from both graft placement holes.

In the thermocouple model housing, a band saw was used to cut a slot out of the cylinder from the top end to the graft placement holes. This was so that thermocouples could be attached outside the housing, and the graft and thermocouples could be set in the housing without needing to thread each set of leads through the graft placement hole, preventing the risk of detaching the thermocouples.

4.3.5.2 Preparing and Securing the Grafts

Grafts were cut with enough length and to span the polycarbonate cylinder and then attached to couplers used to mate with flow tubing (see Figure 10). ePTFE and other Teflon materials are notoriously difficult to bond to. In this case, cyanoacrylate, or generic super-glue (LOCTITE®), was sufficient if pressure was applied while the bond cured. In the case of the thermocouple model, prior to connecting the couplers, the thermocouples were installed. Eight locations were chosen (see Figure 11).

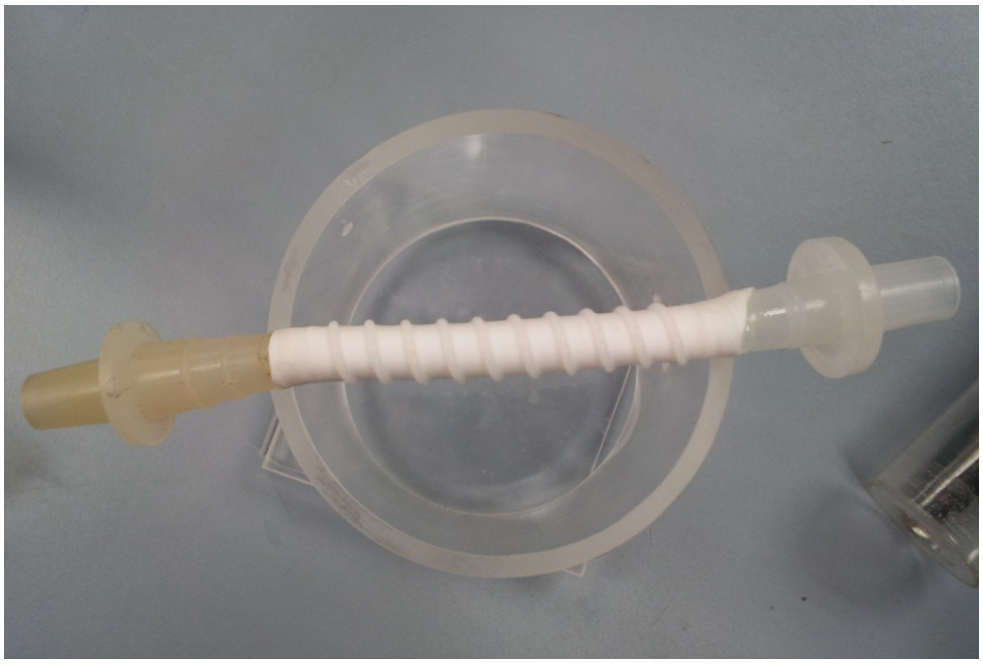

Figure 10. Graft attached to couplers. At this stage, the thermocouple graft would already have had the insertion slits cut and thermocouples installed.

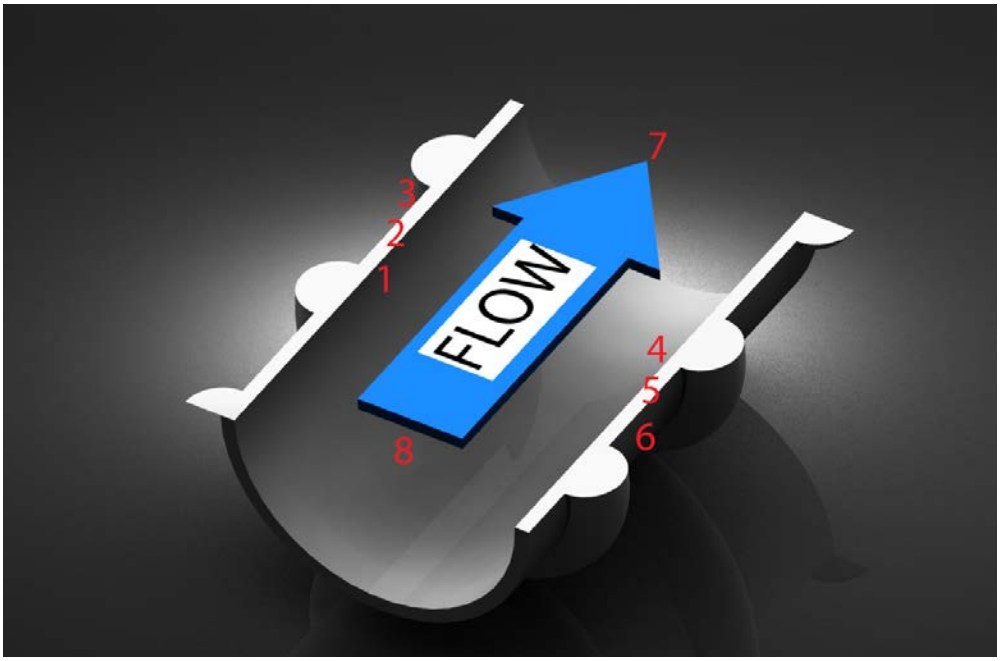

Figure 11. Section rendering of thermocouple placement in graft model. The transducer (not shown) is transmitting below and to the right of image.

Thermocouples 4-6 were placed on the outside, within, and on the inside of the graft wall nearest the transducer. Thermocouples 1-3 were placed on the outside, within, and on the inside of the graft wall furthest from the transducer. Thermocouples 7 and 8 were placed in the flow downstream and upstream, respectively. Thermocouples 1-6 were fine T-type Omega thermocouples. They were placed by cutting oblique slits on either side of the graft between two windings with a surgical scalpel. The incisions were made as long as was allowed by the distance separating windings. The angle of the slit on the first wall followed a line drawn through the numbers 1, 2, and 3, consecutively.

The angle of the slit on the second wall followed a line drawn through the numbers 4, 5, and 6, consecutively. Once the thermocouples were in place, a slit was bonded back in place with cyanoacrylate administered sparingly with a micropippette. The bond was kept under pressure during the curing cycle.

Thermocouples 7 and 8 were handmade, T-type thermocouples: copper and constantan thermocouple wires were stripped and soldered together at a point. They were verified to read temperature within 0.1˚C of the Omega thermocouples. To ensure stable placement in the center of the flow, leads were drawn through two small puncture holes just large enough for the leads on opposing sides of the graft wall. The tip of the thermocouple was then bonded to the graft at the puncture site thereby sealing the puncture. Pressure was applied during curing. Before adding the tissue-phantom, the graft was verified to hold water without leaking.

4.3.5.3 Filling the Model with Tissue Phantom Material

Once the graft was in place, both the bottom and top ends of the cylinder were covered with thin Mylar® (DuPont Tejin Films) sheets so as not to obstruct ultrasound. The Mylar sheets were placed on the faces of the polycarbonate cylinder after hot glue was used to fill the cut out slots. The sheets were sealed with silicone and clamped flat and tight while the silicone cured (see Figure 12).

After the silicone cured, but while the model was still clamped, it was filled with ATS (ATS Laboratories, Inc., Bridgeport, CT) tissue phantom material. When pouring the heated-to-liquid ATS material into the housing, it is important to take care to pour evenly and gently to avoid bubbles in the model. The graft lumen was filled with water and then plugged to keep the graft moist. The tissue-phantom-fill hole was plugged and then the model, while still clamped, was placed in the refrigerator while the ATS phantom set up.

Numerical models of a bare graft [2] showed that heating occurred more evenly when a thin layer of hyperplasia was forming on the lumen of the graft. To simulate this in phantom models, after the first round of ATS phantom set up, a wooden shaft just smaller than the graft's inner diameter was placed inside the graft. A small amount of molten ATS was poured in the graft. The model was then placed back in the refrigerator for the ATS to set. A picture of the final thermocouple model can be seen in Figure 13.

Figure 12. Mylar sheets curing. The graft placement slots are being filled with silicone (although this model does not show thermocouples).

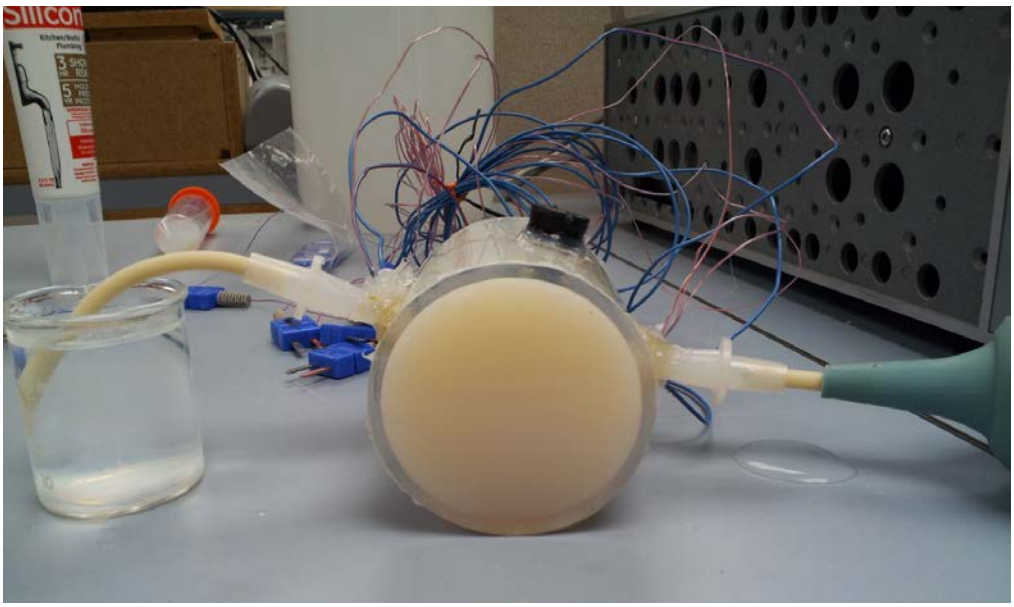

Figure 13. Complete thermocouple phantom model.

4.3.6 Thermocouple Model Exposures

4.3.6.1 Experimental Setup

The model was placed in a water bath and secured with generic optical mounts and an acrylic holding fixture. Channels 4, 5, and 6 were placed closest to the transducer. A focused, 1.443-MHz, transducer with a 13-cm radius of curvature was submerged in the tank and mounted onto a 3-axis translational micropositioner. The transducer was driven by a 55-dB radio frequency amplifier that was triggered with an HP 33120 arbitrary waveform generator. The waveform used to power the transducer was a 1.443-MHz sine wave modulated by a square wave with a duty cycle of 50% and a period of 40 seconds. The input generated 20 seconds of heating followed by 20 seconds of cooling. The thermocouples connected to an 8-channel A/D converter which took readings at a 12-Hz sample rate.

The power amplifier had a 50-ohm output. A custom transducer matching network was placed in series with the transducer. Electrical input power of 5 W was measured by an analog power meter connected between the power amplifier and the matching network. Acoustic power was calculated to be 4 W by the product of electrical power and transducer efficiency (see Appendix A).

4.3.7 Data Acquisition

The micropositioner was adjusted until a maximum change in temperature was recorded at the near wall graft. This was assumed to correspond to the focus of the ultrasonic beam being placed at the near wall of the graft. Visual observation supported this assumption. A comparison of simulated and experimental temperature rise in the

thermocouple model with the focus at the near wall can be seen in Figure 14. Because ambient temperatures differed between the thermocouple model and the MRTI model by about 4˚ C, comparisons are made by the metric of temperature rise.

Numerous attempts were made to maximize temperature in the far wall of the graft by repositioning the transducer. Regardless whether the focus was at the near or far wall, there was never a temperature rise in the far wall of the graft (Channels 1, 2, and 3) that was larger than 1˚ C.

Only limited observations were made with regard to the effect of flow in the thermocouple model. With a constant flow rate of 100 mL/min, there was a 1-2˚ C temperature difference seen between the upstream thermocouple in the flow, Channel 8, and the downstream thermocouple, Channel 7, with Channel 7 being warmer. Channel 8 maintained the ambient temperature. Temperature changes measured at the thermocouples in the beam (numbers 1-6) were approximately 2˚ C lower in the presence of 100 mL/min flow compared to models without flow.

4.3.8 MRTI Model Exposures

4.3.8.1 Experimental Setup

A custom phased-array (Imasonic, Voray sur l'Ognon, France) 1.35-MHz transducer was used in conjunction with an MRI machine at the University of Utah to perform the exposures. The model without thermocouples was placed in a water bath over the center of the transducer.

A peristaltic pump was connected to the model with tubing sufficiently long to allow the pump to be placed outside the MRI room. The MRI data capture and trans-

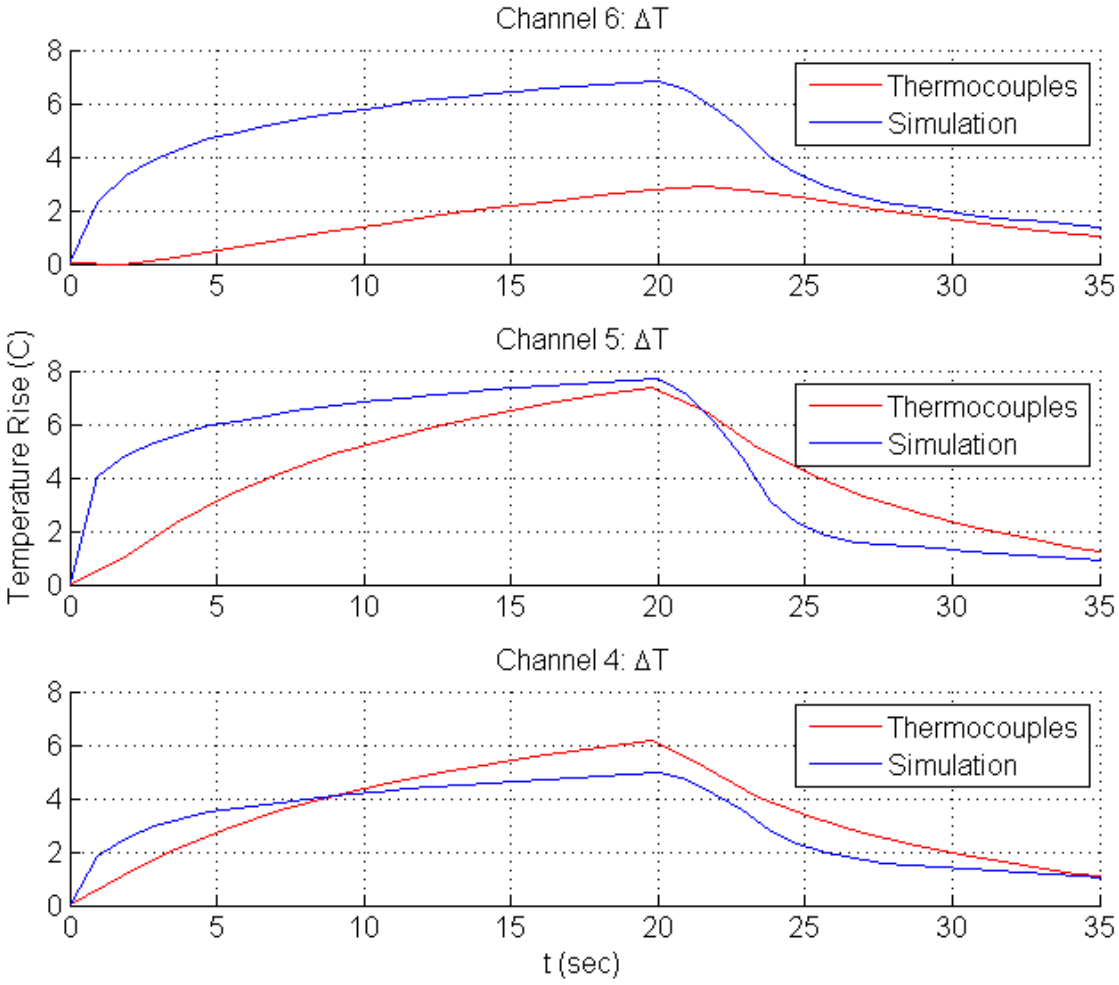

Figure 14. Temperature rise in simulations compared to thermocouple model with focus at near wall. Channels 4-6 (see Figure 11) are compared to simulation results for a model with water-soaked ePTFE parameters and 0.716 W of input acoustic power.

ducer exposure were timed manually by the staff.

4.3.8.2 Data Acquisition

Four exposures were performed. The details of the exposures are shown in Table 7. The results are displayed in a number of figures in Appendix D.

The transducer has not yet been calibrated by the MRI staff for efficiency, so power is reported in electrical watts. Without knowing the efficiency of the transducer, the assumption was made that the actual efficiency fell in the range of 20-50%. This will be addressed in further detail in the discussion section.

For each exposure, 30 seconds of heating was followed by 30 seconds of cooling. Images and temperature data were captured every 3 seconds at the system maximum sample rate. Temperatures were recorded using magnetic resonance temperature imaging (MRTI). MRTI is performed by observing the proton resonant frequency which changes with temperature. Original MRTI resolution was 1.2 mm x 1.2 mm x 3 mm. MATLAB was used to zero-fill interpolate the original data to produce a 1 mm x 1 mm x 3 mm

Table 7. MRTI exposure profile.

	Electrical Power	**Focal Depth**	**Flow**
Exposure #1	8 W	Far wall	No
Exposure #2	15 W	Far wall	No
Exposure #3	15 W	7 mm behind far wall	No
Exposure #4	15 W	7 mm behind far wall	Yes

rendering. Because the graft geometry is smaller than the MRTI resolution, it is important to consider the effects on the data of temperature changes within a voxel. A voxel represents a spatial average of the temperature contained within that voxel. The averaging occurs as a sinc function in all directions, with the peak of the sinc in the middle of the voxel with respect to space. This means that temperatures at the edges of the voxel have little impact on the voxel's temperature value. The flow in Exposure #4 was identical to the flow in the thermocouple experiment: 100 mL/min.

4.3.8.3 Overview of Appendix D

Appendix D shows MRI images that correspond to the planes at which temperature was acquired. Planes were chosen during the experiment to get data in front of the graft, at the near graft wall, at the center of the graft, at the graft far wall, and behind the graft.

Additionally, Appendix D contains the MRI images overlain with MRTI temperature maps for the planes in front of the graft and at the graft near wall for Exposure #1. This single figure is representative of all other heating data at that plane because there was no clear localized heating that area for all power levels and focus placements.

Finally, Appendix D contains MRI images overlain with MRTI temperature maps over the course of the exposure period at various depths. The scaling for temperature across all figures is consistent.

4.3.9 Misaligned Focus Simulation

The results show that the transducer was misaligned. The actual focus appears to be at the focal depth, but 2-3 mm to the lateral side of the graft. A second simulation was performed with the focal point 3 mm laterally away from center of the beam but at the correct focal depth.

4.4 Discussion

The power deposition and thermal models revealed a number of design hurdles that need to be cleared before a successful therapy for hyperplasia in vascular accesses can be pursued. After some commentary on the two experiment modalities individually, the following will be discussed collectively: heating in the far graft wall and power, acoustic power measurement, and absorption in the graft rings.

4.4.1 Thermocouple Model

The heating profiles of the simulations and thermocouple models as shown in Figure 14 contain more differences than correlations. Because of uncertainty with respect to the incident acoustic power in the thermocouple exposure, power input to the computational model was decreased from 4 W to 0.716 W to show some correlation with the temperature profiles (Further discussion on the input power is contained in section 4.4.4.). With a 4-W input, simulated temperature peaks three to four times higher. There are two major differences in the profiles: the temperature peak and the slope of the initial temperature rise. A potential explanation of those differences follows.

The heating time constant, τ, takes the form:

$$\tau = A\frac{c_p}{k}, \tag{16}$$

where c_p is the specific heat capacity and k is the thermal conductivity. A represents values that are constant over this comparison like the masses of the materials involved, the adjoining surface area, and the length of the adjoining barrier. If the pore volume of the graft was filled with air, the thermal conductivity would change drastically: k for air is 0.025 W/m·K while k for ePTFE is 0.35 W/m·K. The bulk specific heat, however, would not change drastically: c_p for air is 1026 J/kg·K while c_p for ePTFE is 1172 J/kg·K as previously listed in Table 6. This, in turn, would make the time constant 8-9 times longer and the peak heating temperature substantially higher. This would also begin to explain why the large decrease in input acoustic power to the simulations was needed to be able to compare heating profiles.

A second difference is the relatively lower-than-predicted temperature measured at Channel 6. This is likely due to the thermocouple sliding away from the graft wall while the cyanoacrylate cured during construction. This would cause the thermocouple to be placed further from the focus of the beam and further into the less-absorbing ABS medium.

The thermocouple model shows that there was negligible temperature rise in the far wall. The simulations predict minimal temperature rise for water-soaked ePTFE acoustic parameters. However, this phenomenon could be worsened by the method of attaching the thermocouples to the graft. The cyanoacrylate that was used to bond the thermocouple to the graft cured to a hard plastic consistency. Although great care was taken to only bond to the section of the thermocouple leads that was away from the beam

focus, if the cyanoacrylate was absorbed through the pores of the graft, the graft acoustic parameters could have been affected. The hard consistency would produce acoustic parameters that would lead to greater reflection at the graft wall.

4.4.2 MRTI Model

Because the temperature data depend on the proton resonating frequency, areas where there is an absence of resonating protons, corresponding to an absence of water, lead to unreliable temperature values. The air outside the model and the model housing produced unreliable temperature readings. It was for this reason that the figures in Appendix D do not show the full extents of the MRI images.

The transducer used in the MRTI exposures has not been calibrated for acoustic output. The MRI staff has a similar system that has been calibrated at near 20% efficiency using the radiation force method and the fixture described in Appendix A.

For the sake of the following discussions, Figure 15, a figure representative of the results in Appendix D, is placed at this point in the text for reference but the dataset in its entirety is contained in Appendix D. Note that as discussed earlier, the black and white MRI image has been made opaque and overlain on the temperature maps. The overlay is most noticeable in slices which bisect the graft, but it can still be discriminated at the front and back walls of the graft.

4.4.3 Power Deposition and Heating in the Far Graft Wall

Most common vascular access placements will not allow for ultrasound to approach the graft through soft tissue from all sides. It is therefore important to assess

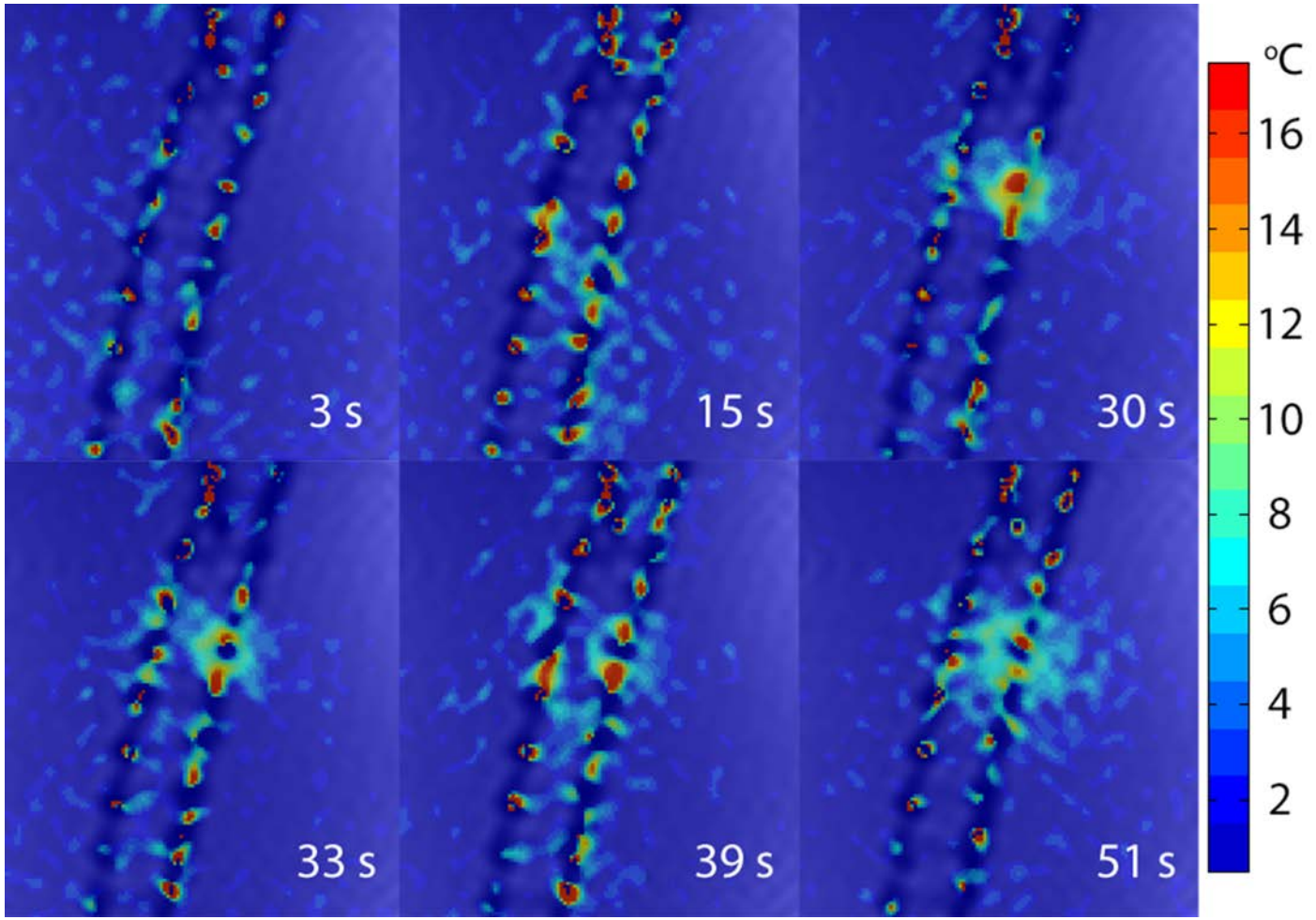

Figure 15. Temperature rise profile with geometry overlay at various times after exposure initiation. Parameters: 15-W electrical input, ultrasound focus at graft far wall, no flow, all planes are 25 mm from front of model. 30 seconds marks the end of ultrasound transmission.

the potential of depositing power in the graft with a single-sided procedure. Figure 8 shows that in simulation, very little power is deposited in the far wall of the graft regardless of acoustic parameters, focus location, or graft positioning. The case with the most heating in the far wall occurs when the graft wall has alcohol filling the porous regions. The thermocouple model is best represented by the water-soaked acoustic parameters. The simulations with these parameters show negligible power deposition and heating at the far wall in all permutations. The observation that no temperature rise could be seen in the far wall of the graft in the thermocouple model regardless of the transducer position supports the simulation results.

It is difficult to draw conclusions from the MRTI results about heating in the far wall. The simulation of the off-center focus shows a different thermal pattern than the centered-focus simulations. In addition, the voxel size along the axis parallel to the beam is more than four times the thickness of the graft wall, so contributions of the surrounding media are averaged in (according to a sinc function, see 4.3.8.2) with data at the plane of far graft wall. In spite of the limitations of resolution, heating can still be discriminated on the temperature images behind and at the graft far wall.

Material properties of the graft play a major role in the efficiency of power deposition in the far wall. Grafts which have been recently implanted in patients will have material properties similar to ePTFE soaked or evacuated in water. They will likely have a significant amount of air remaining in the ePTFE pores. The air remaining in the pores causes scattering and bulk reflection due to a stark contrast in acoustic impedance. The resulting negative effects are two-fold: there is little power deposition in the far wall and extra power deposition in the tissue in front of the near wall (from reflections). This

could lead to potential under-heating in the far wall and overheating in the surrounding tissue.

In counterpoint, it has been shown that after time, the graft is infiltrated by proteins and other biological materials [50] [51] [52]. Acoustically, this means that, a short period of time after installation, the graft will likely become a medium more susceptible to transmitting ultrasonic waves. Clinical experience is necessary to determine if the potentially transient graft wall properties will be a concern.

4.4.4 Acoustic Power Measurement and Simulations Compared to Thermocouple Models

The remainder of this discussion will rely heavily on the information about the radiation force method of measuring acoustic power. The method and some measurements are provided in Appendix A.

The input acoustic power used in the simulations that produced Figure 14 was 0.716 W from the transducer while the acoustic power measured from the transducer was 4 W (review 4.4.1 for an explanation of these values). In addition to the previously proposed explanation due to difference in thermal parameters, there are a few more possible reasons for this discrepancy: overestimated acoustic efficiency, incomplete beam representation in the computational domain, and small air bubbles at the Mylar face of the phantom.

The efficiency of the transducer used in the thermocouple models was measured by radiation force to be 78%. This efficiency is likely artificially high. In practice, efficiencies of transducers are assumed to normally fall in the range of 30-60%,

depending on the piezoelectric material used, transducer housing, and operating frequency.

If the radiation force system used to measure acoustic power uses an absorbing target, as is the case here, but the target is not perfectly absorbing, the acoustic output and in turn efficiency of the transducer can be overestimated by as much as two times. If the transducer efficiency was 30%, then with 5 W of electrical power, the acoustic output would be 1.5 W.

The input plane of the computational domain was 10 x 10 mm. The plane representing the input acoustic field was the same size. In calculating the magnitude of the pressure field at that plane, it was assumed that all of the acoustic power from the transducer was distributed over that plane. In reality, the beam contains some small amount of acoustic power in multiple side lobes that were neglected from the input plane.

The reflection coefficient at an interface between water and phantom is negligible. However, a thin Mylar sheet and some small air bubbles could cause reflection as well. Care was taken to construct the phantom in such a way that air was able to escape when the phantom material set up. Even with these precautions, after days of settling more air could have been released from the phantom and accumulated at the face of the Mylar.

4.4.5 Attenuation and Absorption in the Graft Rings

One of the important findings of this study is that the graft rings have a significant effect on the acoustic heating pattern. The simulations indicate that ultrasonic power is significantly different when the beam transmits directly through a winding at the near wall and when it passes between windings. This can be observed in Figure 14.

The MRTI temperature maps also indicate that the graft rings have an effect on the acoustic heating pattern. The maps show that the relatively hottest locations occur in the windings. It is worthwhile to discuss the reliability of those results. As mentioned earlier, the accuracy of temperature readings depends on the presence of resonating protons. Because the graft rings are of a solid construction, there is less water and fewer resonating protons present inside them. Therefore, the temperature readings inside a winding are less dependable. That fact does not discount the results entirely at those locations, however. Heating due to radiation around the graft rings in the phantom and water are considered reliable. For an illustration of this conclusion, consider Figure 16. After only 3 seconds of 8-W electrical exposure (probably ~2-W acoustic), it is unlikely that there has already been a 17 degree temperature rise in the rings as the figure indicates. In fact, some of the rings, which after 3 seconds show a 17˚ temperature rise, show no temperature rise at their center after 15 seconds. This suggests that there is noise in the data at the center of the rings. Consider further: after 30 seconds, rings at the bottom of the image away from the heart of the focal zone have begun to show a temperature gradient in the surrounding media. This observation indicates that there is appreciable heating aside from MRTI data fragments.

4.5 Conclusions

Brinton concluded in [30] that the optimum temperature for prevention or inhibition of hyperplasia would be 47˚ C. From body temperature of 37˚ C, that would be a temperature rise of 10˚ C. The thermocouple model suggests that such selective heating is possible, although insufficient acoustic power was used to produce similar temperature

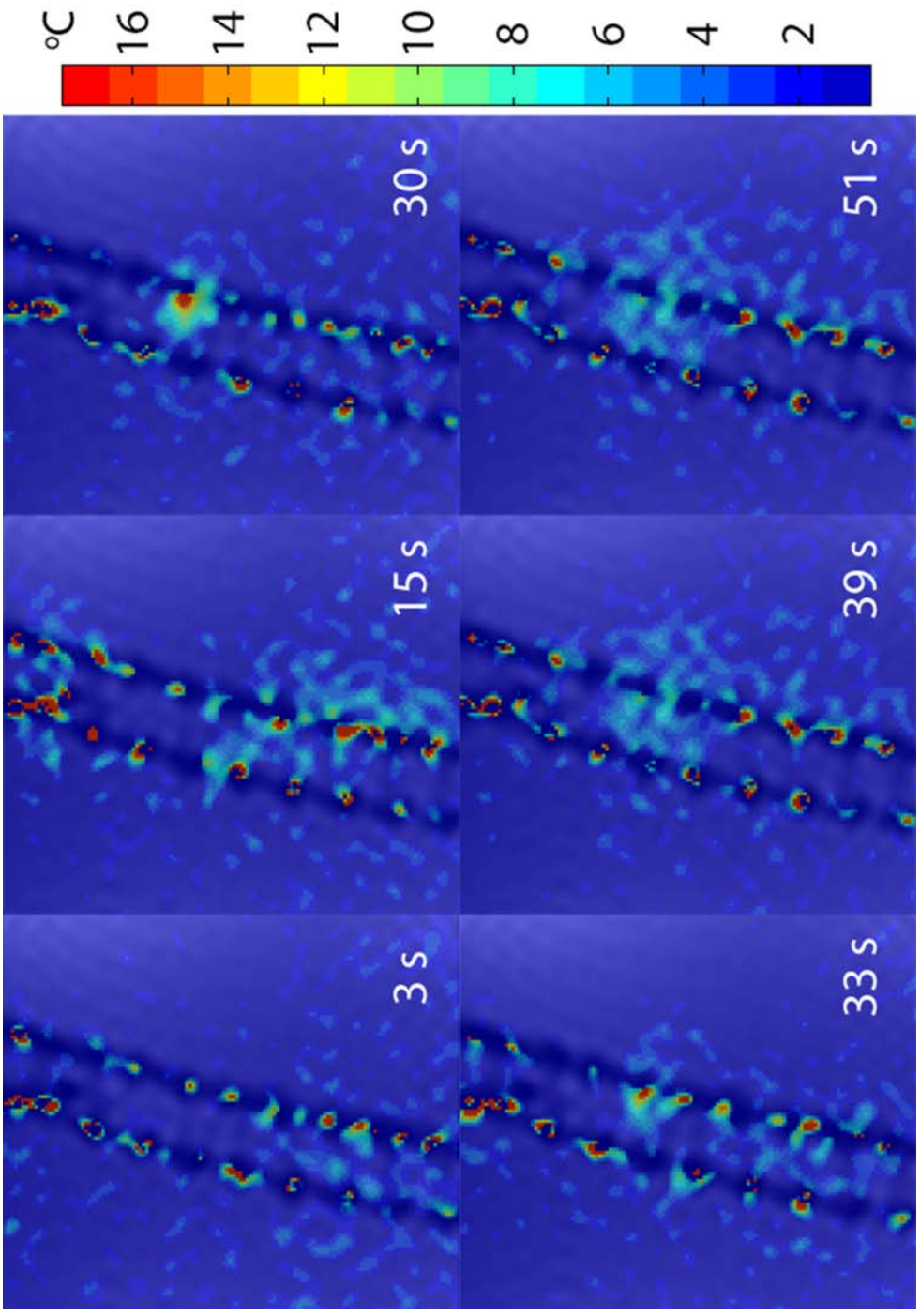

Figure 16. Temperature rise profile with geometry overlay at various times after exposure initiation. Parameters: 8-W electrical input, ultrasound focus at graft far wall, no flow, all planes are 25 mm from front of model. 30 seconds marks the end of ultrasound transmission.

rises. The MRTI model shows that in a lifelike geometry, sufficient heating can be produced. A point of concern in both experiments, however, is the heating in the tissue adjacent to the near wall of the graft.

Overheating blood is one of the pressing biological concerns in a therapy like this. MRTI Exposure #4 indicates that there is not an appreciable heating in the fluid in the graft lumen. As good as this is for the blood, it is important to consider that this may be detrimental to the treatment of hyperplastic growth. If the blood acts as a thermal heat sink, it may be difficult to heat the hyperplasia. The results indicate that there is still heating in the graft wall (see Figure 17 at 30 seconds.).

Because the ultrasound transmission is intimately connected with the acoustic properties of the graft, and it has been shown that those properties can vary dramatically, there is only limited value in *ex vivo* experiments. For this research to continue, it is necessary to conduct experiments in an animal model where the acoustic properties of the graft can be relied on to be biologically accurate.

4.6 Future Work

4.6.1 Frequency Optimization

Laying aside the potentially transient graft wall acoustic parameters, there are a number of adjustments that can be made to increase the ratio of power deposition in the far wall to power deposition in the near wall. A decrease in operating frequency will cause less attenuation due to absorption in all involved materials. This will lead to a greater transmission through the near wall and greater incident power in the far wall. In addition to decreasing attenuation, the thickness of the graft wall will be smaller in

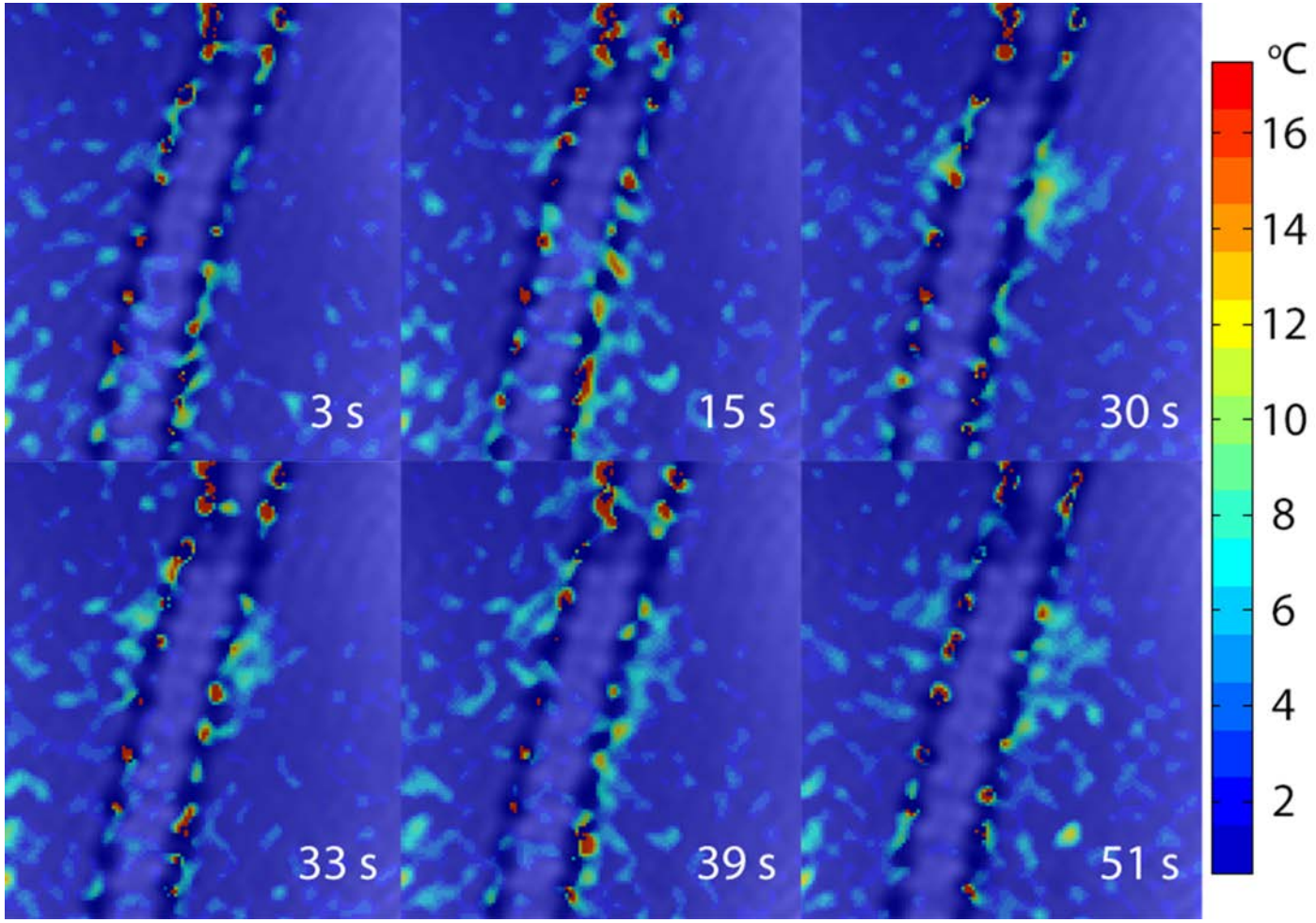

Figure 17. Temperature rise profile with geometry overlay at various times after exposure initiation. Parameters: 15-W electrical input, ultrasound focus 7 mm behind graft far wall, with flow, all planes are 25 mm from front of model. 30 seconds marks the end of ultrasound transmission.

comparison to the spatial wavelength of the ultrasound and will become less significant to transmission. However, as penetration to the far wall increases, absorption at the far wall will decrease. There is likely an optimal relationship between penetration and absorption for this graft geometry.

Another avenue to investigate is to consider the graft wall as a half-wave transformer. The concept of a half-wave transformer is one that is relevant in plane waves and transmission lines. In the realm of plane waves and transmission lines, the concept of a half-wave transformer can be described as follows:

> When propagating from a source medium to a load medium, transmitting through an intermediary, if the intermediary is an integer multiple of a half wavelength the load impedance appears unchanged.

When attempting to maximize transmission through an intermediary, a strategic selection of frequency to make the intermediary a multiple of a half wavelength can be helpful.

In the case of HIFU and the vascular graft geometry, the incident wave is not wholly planar nor is the graft-tissue interface. However, the half-wave concept may still prove advantageous for those portions of the incident wave which approach the graft at near-normal incidence. The portions of the incident wave that approach the graft-tissue interface at angles other than the normal would not be affected by a half-wave optimization.

In any case, a numerical frequency optimization study will provide valuable insight into graft heating. Even in a clinical setting, a narrow-band frequency scan could be performed at diagnostic levels to determine which frequency could “see” the far wall

best. Results of this scan could give some indication of which frequency would be best to perform therapy. If an optimized frequency point could be detected, the results could also provide a rough speed of sound measurement for the graft material, assuming that the optimized transmission point occurred at a half wavelength and knowing the graft wall dimensions. The speed of sound could be used to make inferences about the local infusion of biological material into the pores of the graft.

4.6.2 Animal Models

As stated, in order to make further progress in this research path, ultrasound exposures must be performed in an animal model. Because the acoustic parameters of the graft in its native environment are uncertain and may vary, there is a limited amount of information that can be gleaned from *in vitro* experiments. One of the most productive studies would follow the research path of [37]. Vascular grafts would be implanted in porcine models. The control group would not receive any ultrasound therapy and the experimental group would undergo ultrasound exposure.

Prior to an animal model, it would be necessary to further certify the acoustic output of the various systems used in this thesis. This would provide a more firm indication of the expected temperature rise given an input power. In addition, a method of temperature measurement in the animal must be identified. Using the system in place at the University of Utah, it is possible to measure the temperature with MRTI.

CHAPTER 5

TRANSDUCER DESIGN

5.1 Abstract

A design for a hybrid therapeutic/diagnostic semi-annular array is presented. Using MATLAB, the Rayleigh-Sommerfeld integral is calculated to simulate the pressure at the focal plane. The pressure is compared to that of a classical solid transducer of the same dimensions. An optimization was performed to determine the drive pattern for the elements to produce a pressure pattern as closely related as possible to the pressure pattern of the solid transducer.

5.2 Introduction

Ultrasound has traditionally found its largest clinical contribution to be in the arena of diagnostics. In the last few decades, an increasing number of ultrasound therapies have been developed. The most current developments in ultrasound involve noninvasive high-intensity focused ultrasound (HIFU) for therapeutic applications. As is the case with many noninvasive therapies, one of the challenges is monitoring the treatment that cannot be observed without secondary instrumentation. In the case of HIFU, the safety concerns that need consideration fall into two categories: power deposition control and focal location.

5.2.1 Monitoring Power Deposition

Too little deposited power can render a HIFU treatment ineffective. In contrast, too much deposited power can be a hazardous. Large power deposits can generate excessive heating in native tissue and induce necrotic cell death. Overheating can occur anywhere in the beam path within fractions of a second. There is not currently a noninvasive mechanism known for measuring acoustic power deposition that would be suitable for a clinical setting. Treatment planning involves quantifying the beam shape, the ultrasonic strength of the source under various drive conditions, and the involved materials' acoustic properties. The acoustic power is then calculated at treatment time based on a measured electrical input power.

Different acoustic power levels are appropriate for different applications. The metric most commonly used to compare the thermal component of ultrasound treatments is the thermal index. The thermal index is defined as the ratio of the acoustic power to the power required to raise temperature of the medium through which the acoustic energy travels by 1° C.

Along with the threat of thermal damage, there is also the potential to cause harm by a mechanical effect known as cavitation. Cavitation comes in two forms: stable and transient. Stable cavitation is the rapid, oscillatory expansion and contraction of gas bubbles. Transient cavitation is the rapid expansion and violent collapse of gas bubbles. During the rarefaction of the oscillating ultrasonic pressure, gas in tissues or liquids can expand and combine to form bubbles or enlarge existing gaseous pockets. During the successive compression of the oscillating ultrasonic pressure, the bubbles contract (stable) or implode (transient). The collapse or contraction of the bubbles depends on the

magnitude of the pressure wave.

Cavitation is used as a primary mechanism in a myriad of ultrasound therapies such as tumor ablation and thrombolysis. However, predicting the likelihood and type of cavitation is heavily dependent on material properties and gas concentrations and is very difficult to do in practice. Transient cavitation has the potential to cause calamitous injury to local tissue. If ablative cavitation is the intent, then transient cavitation is a necessity; however, the presence of unintended or misplaced cavitation can be disastrous.

Predicting or preventing cavitation, like power deposition, is a design-time engineering problem. One metric used as an indicator of the likelihood of cavitation is the mechanical index, defined as the ratio of peak negative pressure to the square root of frequency:

$$MI = \frac{PNP}{\sqrt{f_{MHz}}} \tag{17}$$

where PNP is the peak negative pressure and f_{MHz} is the frequency in MHz. For diagnostic ultrasound, a mechanical index of 1.9 is considered to be the upper safety limit. Many of the treatments in which cavitation is employed are pulsed, meaning that the ultrasound waves are not continuously emanating from the transducer for the entirety of the treatment. Only temporally short but usually acoustically powerful bursts are used. This increases the likelihood of cavitation without inducing excessive heating. When designing a primarily thermal therapy like the one this thesis proposes for neointimal hyperplasia, care should be taken to ensure that the threshold for cavitation in the surrounding tissues is safely out of range.

5.2.2 Treatment Target Location

In HIFU treatments, the target location is almost always intended to be at the focus of the ultrasound beam. It is important to distinguish between the focus of the ultrasound beam and the geometrical focus of the ultrasound transducer. Because tissue boundaries and inhomogeneity in the medium can cause beam reflections and refractions, the geometric focus of the ultrasound transducer does not always coincide with the focus of the ultrasound beam.

Because of the potential difference between the beam focus and the transducer focus, simple mechanical dimensions cannot always be relied to predict the focus of the beam. By the same principle, nonacoustic-based diagnostic methods cannot predict the acoustic transformations that a medium will impose on an acoustic beam. The most accurate method to position the focus of a therapeutic transducer is by using diagnostic ultrasound to acquire target position. The diagnostic ultrasound undergoes the same refraction as the therapeutic ultrasound regardless of frequency difference. This chapter will present a transducer design that could be used to accommodate the thermal treatment of neointimal hyperplasia in vascular grafts. The design will detail a combined therapeutic and diagnostic ultrasound transducer.

5.3 Methods and Results

5.3.1 A Diagnostic-therapeutic Hybrid Design

In order to use a diagnostic transducer to position a therapeutic transducer, there must be some mechanical mating or registering that can be used to enforce a spatial relationship between the positioning (diagnostic) and therapeutic elements. This

transducer design proposes mounting a linear phased array in the middle of a focused semi-annular array. An image of the proposed element configuration can be found in Figure 18.

The dimensions of the transducer will be consistent with a large medical handpiece. This allows a technician to position the transducer to apply a therapy without the assistance of numerical control.

In Figure 18, the white rectangle element shows the placement of an "off-the-shelf" linear phased array. The design of the linear array will not be considered in this thesis because sufficient work has already been completed and linear arrays can be

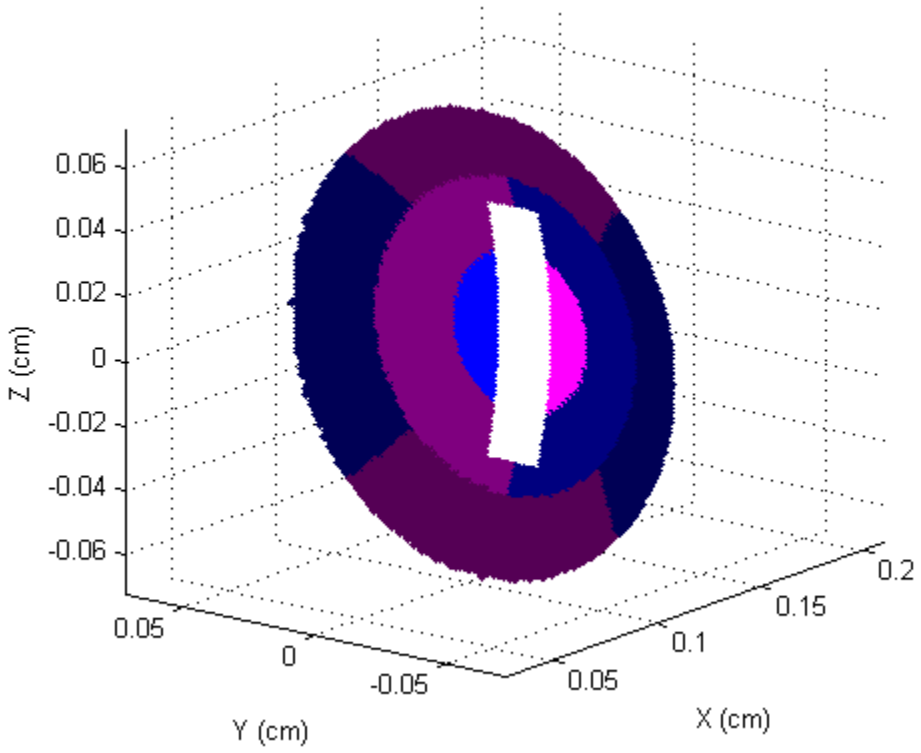

Figure 18. Transducer proposed element configuration. The white rectangle element represents an "off-the-shelf" linear array. The blue and purple elements are therapeutic elements. Dimensions are in centimeters.

purchased commercially from companies like Olympus (Waltham, MA), Blatek (State College, PA), VisualSonics (Toronto, CA), etc. The array will be in all ways similar to linear arrays used in standard diagnostic instrumentation. The dimensions as shown here are representative of typical size for a linear array handpiece without the typical ergonomic housing. The linear array will allow for diagnostic focusing in a plane that is coplanar to the plane that contains the linear array elements (shown here as the z-axis). If the intended focal location is along the other axis (y-axis) perpendicular to the axis of propagation (x-axis), the transducer can be rotated by the operator.

The therapeutic element configuration here is termed semi-annular because the piezoelectric elements would be formed from polarized rings and then separated at three intervals around the ring. There was dual motivation in this design to allow electronic focus-steering along the axis of propagation and create a geometry that could potentially correct for the aberrations in the beam, especially at the focus, caused by the diagnostic "dead zone."

5.3.2 Design Simulations

To determine the pressure pattern at a plane an arbitrary distance away from the transducer, the Rayleigh-Sommerfeld integral was calculated in MATLAB. The Rayleigh-Sommerfeld integral discretizes the transducer elements into infinitesimally small point sources and evaluates each point source's contribution to total acoustic pressure at all points on a user-specified plane perpendicular to the axis of propagation. The individual contributions are then summed in space to create a representation of the complex pressure pattern from a nonplanar source at a plane. Dr. Douglas A. Christensen

at the University of Utah provided the main body of code for calculating the Rayleigh-Sommerfeld integral. The code was modified to include individual contributions from annular elements and the ability to drive elements at different power levels. The capability of adding phase delays to the elements was already present in Dr. Christensen's code. The modified code can be found in Appendix E.

For a control, a transducer of the same arc dimensions as the design transducer but without separate elements and a linear array dead zone was simulated. A plot pressure at the focal plane of the control transducer can be seen in Figure 19. A side view plane is not shown because the focal spot is symmetrical about the axis of propagation. In terms of pressure, side lobes are approximately 41.5 dB lower than the peak.

The pressure pattern at the focal plane of the design transducer can be seen in Figure 20. In the case of the designed transducer, the pressure on the focal plane is not symmetrical about the axis of propagation. This can be seen by noting that the side lobes do not have the same shape or magnitude in the side view as in the front view. The larger side lobes in the side view fall parallel to the dead zone caused by the phased array. The first side lobe ranges from 26-39 dB lower than the peak pressure. The peak pressure of the design transducer is 1.3 dB lower than the peak pressure of the control transducer.

5.3.3 Phase Drive Optimization

An optimization study was performed to determine the ideal phases and magnitudes of each of the eight elements in the design transducer. In MATLAB a function, ERFAdiff, was written to compare two pressure planes. The output of the

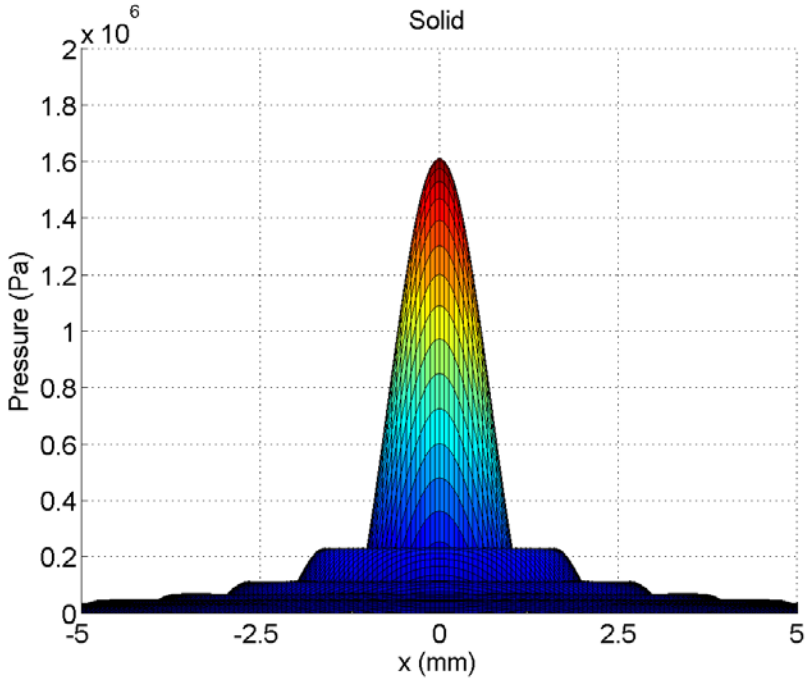

Figure 19. Projection view of absolute value of pressure of solid transducer at focal plane. Total acoustic power input = 1 W.

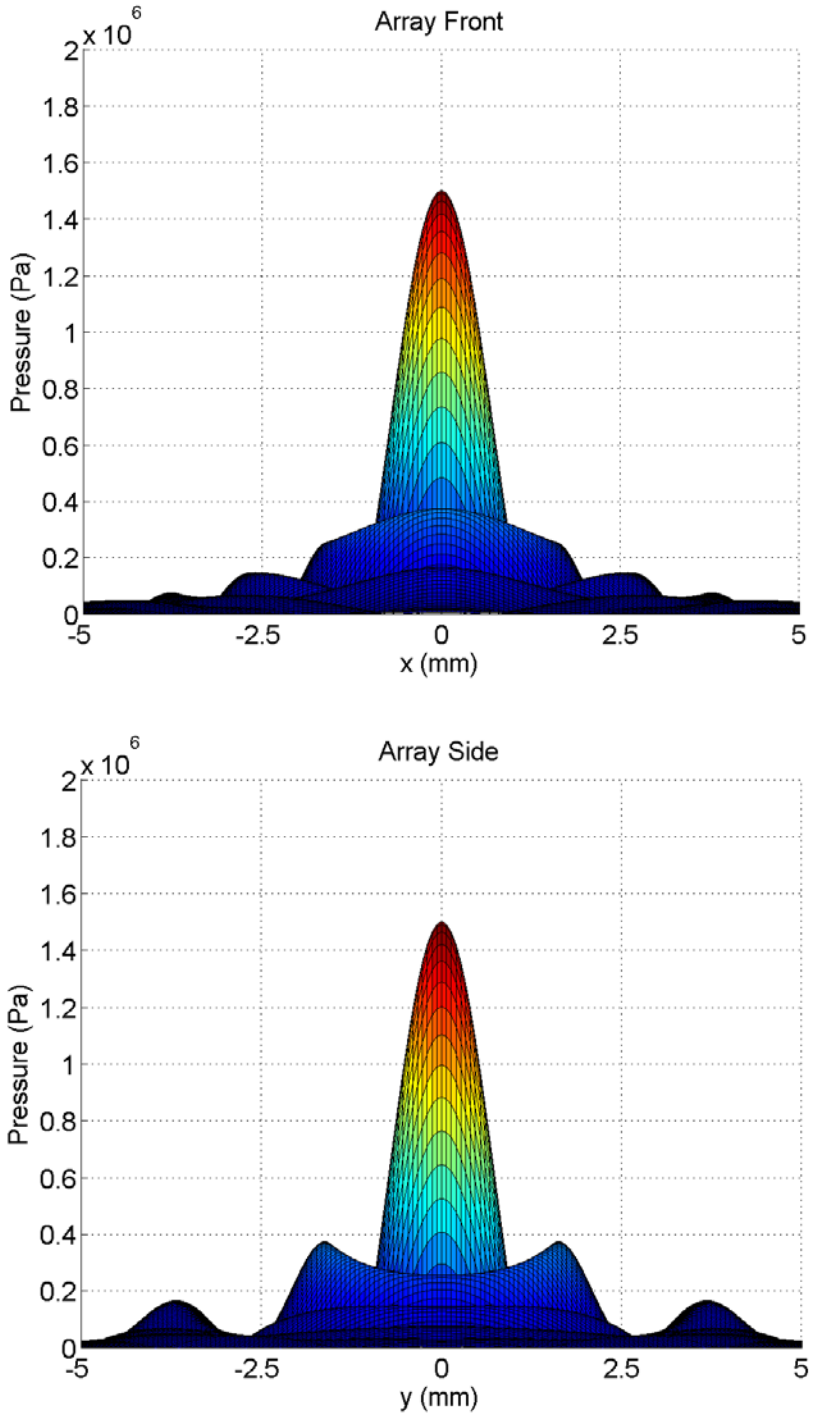

Figure 20. Projection view of absolute value of pressure at the focal plane of the proposed transducer design. Top: Front view. Bottom: Side view.

function was a spatial residual defined as the difference between the magnitudes of the complex pressures for the control and design transducers at the focal of plane. Using the *fminsearch* function in MATLAB, ERFAdiff was minimized with respect to the magnitude and phase of each element in the design transducer. Code used to perform the minimization routine can be found in Appendix E.

fminsearch users the Nelder-Mead polygonal gradient descent minimization routine to find the nearest local minimum of an arbitrary function. Because *fminsearch* only finds local minima, it is important to provide the algorithm with an educated initial guess.

Two initial guesses were tested: (1) all elements given unit magnitude and zero phase and (2) the top and bottom (with respect to *z* in Figure 18) elements' magnitude scaled by 2 and driven together, 180° out of phase with the other elements scaled at unit magnitude. The first initial guess converged to the same minimum residual as the guess. The second initial guess converged to a solution that had a greater error than the first initial guess, meaning that it was a local minimum, but not globally as accurate as the first initial guess. Those results suggests that, given the proposed design configuration, driving all elements in phase and at the same power level will cause the fewest aberrations in the pressure pattern at the focal plane.

5.4 Discussion

5.4.1 Clinical Phased Array Placement

The difference between the pressure patterns at the focal plane of the control and design transducers did not contain as many aberrations as were expected. This means that

in clinical practice, a hyperthermia treatment could likely be performed sufficiently by a transducer with the proposed design. The most important area of the beam, the geometric focus of the transducer, suffered the least change resulting from phased array placement. This geometry assumed that the phased array was placed flush with the back arc of the transducer. In clinical application, that geometry might not be the most advantageous option. To facilitate coupling the linear array with tissue, it may be better to move the transmission of the array slightly closer to the tissue so that the edges of the array were not so far sunken behind the arc of the therapeutic elements. The adjustment, if slight, would only marginally affect the beam pattern, but if too large, the phased array would begin to interfere with the beam pattern of the therapeutic array.

5.4.2 Optimization Comments

Although this thesis only considered one configuration of elements, the optimization study suggested that no phase arrangement could be used to improve aberrations over the solid transducer equivalent (with dead zone). While it is possible to iteratively solve the Rayleigh-Sommerfeld integral in reverse by Fourier spatial propagation from a given focal plane to determine the phase and magnitude of an arbitrary geometry of elements, this study followed an optimization approach. An iterative minimization routine was used to find a nearest match. MATLAB's *fminsearch* minimization routines used require a good initial guess. Another option for minimization is to compare all possible combinations inputs, but this approach is rarely used because it requires unrealistic convergence time. A bounded set of possible inputs can be used to decrease redundant solutions, but in this case, a bounded set would still be very large.

Qualitative observation does support the minimization results. The only adjustments that can be made at each element are phase and magnitude. A phase shift at each element can be analogized to a translation in the spatial domain parallel to the axis of propagation. The translation can be calculated knowing the fraction of a period corresponding to the phase shift and the speed of sound of the medium coupled to the transducer. The phase shift allows the element to appear to be in a different spatial position in relation to the rest of the elements. The change in spatial position is restricted to movements parallel to the axis of propagation. Correcting the effects due to the dead zone in this geometry would require a spatial transformation perpendicular to the axis of propagation so that the element appeared to be in the dead zone. In addition, an adjustment in the drive level of each element does not produce an apparent spatial shift.

5.5 Conclusions

It appears that without any compensation, a therapeutic/diagnostic hybrid transducer with the dimensions proposed could be used as a handheld transducer in clinical practice. In the case of mild hyperthermia for hyperplasia, the aberrations in the beam caused by the placement of a linear array would not be problematic.

Because the best drive pattern found for the multi-element arrangement was running the elements in phase and at the same amplitude, the number of elements in the therapeutic portion of the transducer could be reduced to reduce production costs.

If further numerical simulations found a phase pattern that required more detail to reduce aberrations, the costly option of separating the therapeutic portion of the trans-

ducer into finer elements could be explored. The optimization technique described here would be suitable for such a design process.

CHAPTER 6

CONCLUSIONS AND FUTURE WORK

6.1 Conclusion

Developing a noninvasive method of heating implanted ePTFE grafts requires a foreknowledge of graft acoustic properties *in vivo.* Experiments revealed that graft acoustic properties are intimately dependent on the medium in which the graft is immersed. An alcohol-like, fluid medium that infiltrates the graft pores yields an order of magnitude greater acoustic transmission through the graft walls than a medium which does not fill the graft pores, like water. In practice, water is not easily absorbed into the hydrophobic graft walls and with air filling the graft voids, acoustic transmission is hampered. This is due to disparity of acoustic impedance. The acoustic impedance of graft material in alcohol was measured to be 1.49 ± 0.149 MRayl (close to water at 1.5 MRayl). The acoustic impedance of graft material soaked in water was measured to be $0.478 \pm 1.43 \times 10^{-2}$ MRayl. It is likely that the biological surroundings of the graft will yield more alcohol-like results. Experimentation with *in vivo* graft models is needed to quantify acoustic parameters in the relevant biological settings.

Simulations considering the varying graft acoustic parameters, focal locations at the near and far walls of the graft, and with the beam transmitting through and between PTFE rings showed that with a focused acoustic input of approximately 2 W, temperature

rises of 17˚ C could be achieved in the near graft wall. However, ultrasonic power deposition was largely inhibited in the far graft wall in cases where the graft had been modeled as being soaked in or evacuated in water. With regard to heating the graft walls evenly, the graft rings proved to be a hindrance by shadowing the far wall even though the caused localized heating due to higher relative absorption.

Thermocouple and MRTI models of approximately 1 and 3 W (acoustic power), respectively, showed only some correlation between the measured temperature and the simulated thermal rise. The tightness of the correlation to the simulations is dependent on acoustic power measurement techniques and accurate material properties (acoustic and thermal). Measured thermal rises in the graft for the given power range were 8˚ – 17˚ C. The temperature rise is sufficient to potentially inhibit or prevent hyperplasia according to [30]. In the case of the thermocouple and MRTI models, water flow through the graft did not prevent heating in the graft, and did not cause significant heating of the water. This suggests that blood would not be heated substantially *in vivo*.

A hybrid therapeutic/diagnostic transducer design was presented. Pressure patterns at the focal plane compared to a solid therapeutic transducer were shown to have practically negligible differences. An optimization of the individual element drive phases and magnitudes showed that the drive arrangement that produced the fewest aberrations in the focal plane was pattern of equivalent phase and magnitude.

6.2 Suggestions for Future Work

6.2.1 Animal Models

In order to make progress in this research, ultrasound exposures must be performed in an animal model. Because the acoustic parameters of the graft in its native environment are unverified and may vary over a graft's lifetime, there is only a limited amount of information that can be gleaned from *in vitro* experiments. A productive studies would follow the research path of [37]. Vascular grafts would be implanted in porcine models. The control group would not receive any ultrasound therapy and the experimental group would undergo ultrasound exposure.

Prior to an animal model, it would be necessary smooth out the concerns with the efficiencies of the transducer systems used in this thesis. This would provide a more firm indication of the expected temperature rise given an input power. In addition, a method of temperature measurement in the animal must be identified. Using the system in place at the University of Utah, it is possible to measure the temperature with MRTI.

6.2.2 Ultrasound Therapy Enhanced by Contrast Agent

Some of the prior research presented in Chapter 2 suggests that there may be a nonthermal component of ultrasound exposure that could inhibit neointimal growth. Mechanical action could be amplified by the use of an ultrasonic contrast agent of microbubbles. The cavitation could potentially be activated locally inside the graft and monitored readily with diagnostic ultrasound. This might provide mechanical scrubbing action in addition to the thermal therapy presented in this thesis. *In vitro* cavitation ex-

periments could be performed inexpensively in a water bath with passive cavitation detection, a HIFU transducer, and a diagnostic ultrasound monitoring system.

APPENDIX A

RADIATION FORCE BALANCE ACOUSTIC OUTPUT MEASUREMENT

The radiation force balance technique is an experimentally simple method of measuring acoustic power. This appendix presents a brief explanation of the theory and experimental setup. An in-depth treatment of the theory can be found in [56]. Some common experimental pitfalls are addressed. Results of acoustic power measurements for the transducer used in the thermocouple experiment are presented and critiqued.

A.1 Theory

An ultrasound beam propagating through any medium has a given amount of energy that depends on the magnitude of the acoustic pressure and acoustic impedance of the medium. A common term used to describe the energy in an ultrasound beam is intensity, I:

$$I = \frac{p^2}{Z}, \tag{18}$$

where Z is the acoustic impedance of the medium and p is the pressure. The units of I are watts. Considering fundamental physics, acoustic power is due to a transfer of momentum: as a piezoelectric transducer expands and contracts under a sinusoidal

voltage, particles of the medium in contact with the face of the transducer are pushed forward and pulled backward, causing a compression and rarefaction that travels through the medium. Here, the assumption is made that the sinusoid describing oscillation of the source does not have any "dc" component, so the average displacement is 0. Operating under this assumption, the energy contained in the particles can be described by kinetic (due to the particle motion) and potential (due to the pressure gradient in the compressions and rarefactions) Newtonian momentum.

When any object intercepts the ultrasound beam, there is a transfer of momentum. It may appear initially that momentum is not transported by the ultrasonic beam. However, consider a surface, *S*, that just barely encloses the object. Positive momentum is defined to be in the direction of the beam. During compression at the boundary of *S,* matter is transferred into the surface, carrying with it positive momentum. During rarefaction, matter leaves *S,* carrying with it momentum in the opposite direction: removal of negative momentum. Therefore, all momentum transfer is positive and there is a net force enacted by the medium on the object. If the sign convention for momentum is reversed, the resulting force would be in the opposite direction but would be enacted on the medium by the object. The physical effect is the same.

In the case that the object intercepts the entire beam and is a perfectly absorbing ultrasonic target, all of the energy in the ultrasonic beam is transferred to the target. The target feels a force due to this energy transfer:

$$\bar{F} = \bar{E}A \tag{19}$$

where F is the force on the target, E is the mean energy density in the beam, and A is the cross-sectional area of the beam. Following the notation in the literature, a bar over a

variable indicates a time-averaging or a steady-state condition.

$\overline{E}$ is related to the power in the ultrasonic beam by

$$\overline{E} = \frac{W}{cA} \tag{20}$$

where W is the acoustic power, and c is the speed of sound in the liquid medium. Then, $\overline{F}$ is

$$\overline{F} = \frac{W}{c}. \tag{21}$$

In the case of a perfectly reflecting target, no energy is transferred to the target, but there is an increase in the dynamic pressure of the liquid medium. There is a resulting radiation force felt on the target [57]:

$$\overline{F} = \frac{2W}{c}. \tag{22}$$

A.2 Experimental Setup

The Equations (22) and (21) can used to quantify acoustic power with reflecting or absorbing targets in various geometries and configurations. One of the most common, and the one used in this thesis, is to measure the change in apparent mass of an absorbing target in the presence and absence of an ultrasonic beam. The change in apparent mass is related to the acoustic force by the acceleration of gravity. Then using Equation (21), the acoustic power can be written:

$$W = c\Delta mg \tag{23}$$

where Δm is the change in measured mass, and g is the acceleration of gravity.

A.3 Common Pitfalls

In principle, this is a simple experimental procedure. However, there are a few caveats about which the experimenter must be aware. Firstly, it is important to ensure that the target encompasses the whole acoustic beam. Failure to do so will lead to underestimation of acoustic power. Secondly, the target must actually be *absorbing* as opposed to merely *attenuating* acoustic energy. The importance of this can be seen if we consider a situation where the target is constructed from a meshwork of acoustically reflective material. In this case, the momentum is not transferred into the target, but off at various angles, depending on the direction of the incident pressure and the angle of the portion of framework the pressure encounters. Measured force will be somewhere between the results of Equations (22) and (21), meaning that the measured acoustic power could approach double the actual acoustic power. Thirdly, if a target is actually absorbing, the generated heat can cause the target to become more buoyant in the medium in which it is suspended. This can cause a change in apparent mass that is not due to the acoustic power in the beam. Finally, the absorption of a target will change with frequency, so the target properties must be ensured to be absorbing at the frequency of interest.

A.4 Thermocouple Transducer Power Measurements

Using the radiation force setup in Dr. Douglas A. Christensen's lab at the University of Utah, acoustic power measurements were taken for the transducer used in the thermocouple experiment. Measurements were performed at the transducer's resonant frequency at various input power levels. Electrical power was measured with an

analog electrical power meter. The results of the experiment are contained in Figure 21.

In practice, transducer efficiencies above 60% efficient are suspect. For this reason, the quality of the acoustic target used in the radiation force measurements was examined. Using a 1-MHz unfocused transducer from Constantine Technologies, LLC (Salt Lake City, UT), reflections were measured from an aluminum plate and compared to reflections measured from the radiation force target. Reflections from the absorbing target were 20 dB lower than from the reflecting plate. Those reflections, however, only represent sound which was reflected in the receive pattern of the transducer. The reflection of the absorbing target may have been greater than what was measured. Reflections at interfaces in the brush target that were not perpendicular to the axis of

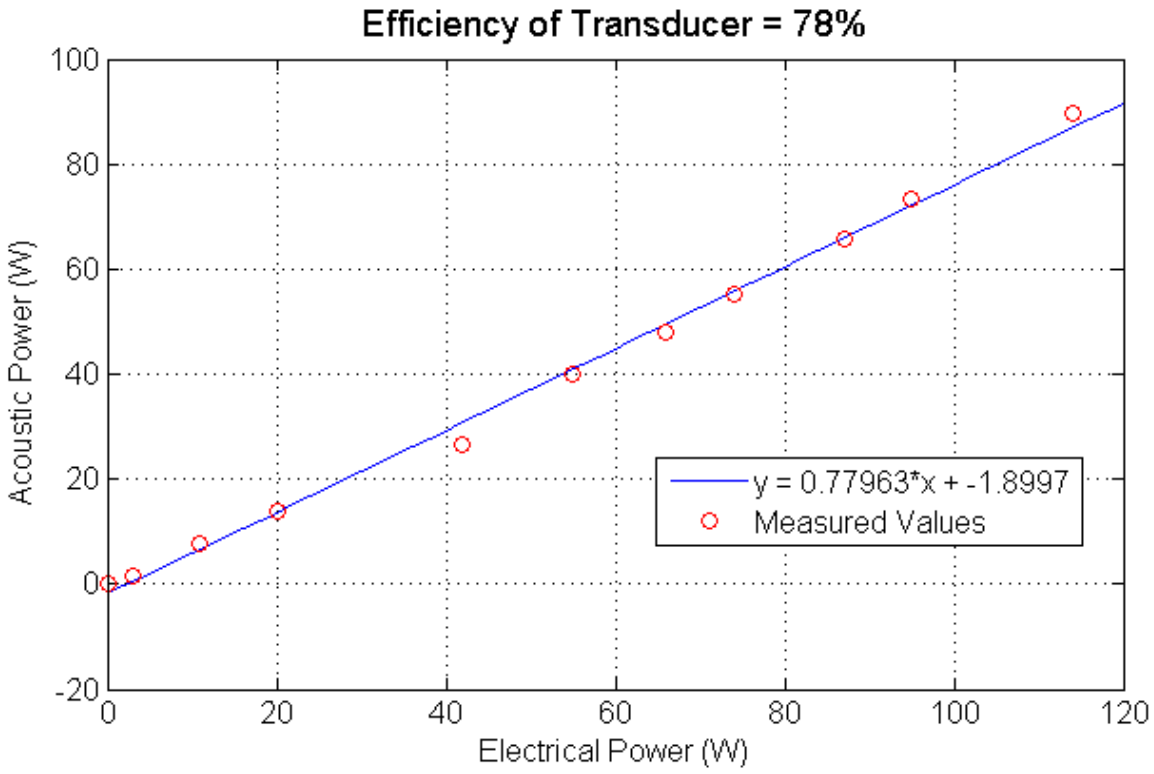

Figure 21. Radiation Force Balance measurements of transducer efficiency. A least-squares fit is shown in blue. The slope of the fit line is the efficiency of the transducer.

propagation would not be measured. Those results suggest that the target has some significant reflective properties and that the acoustic power measurements could be significantly exaggerated.

APPENDIX B

MESH TO GRID CONVERSION ALGORITHM

B.1 Introduction

Finite Element Analysis (FEA) uses the Finite Element Method (FEM) to discretize computational domains in preparation for numerical analysis. Other techniques like the Hybrid Angular Spectrum (HAS) and Finite-Difference Time-Domain (FDTD) simulate wave propagation over a regularly spaced rectangular grid. Solving the wave-equation using with FEM can be computationally expensive compared to HAS, especially in ultrasonics where high frequencies are used. It is useful to perform an ultrasound wave propagation simulation in HAS and subsequent thermal simulation with FEM. A major obstacle to this course of study is converting geometries to and from the regularly spaced grids in HAS and volumetric meshes in FEM. This appendix presents an algorithm and script to generate and mesh geometries in SolidWorks and convert meshes to regularly spaced grids.

B.2 Procedure

1. Create SolidWorks parts for the geometry of interest. The parts should represent different materials and different geometries. For instance, if modeling a graft with a layer of muscle-like tissue on the exterior and a layer

of muscle-like tissue on the interior, three parts should be modeled: one for the graft (assuming its acoustic properties are homogenous over the graft), one for the exterior muscle-like domain, and one for the interior muscle-like domain.

2. The parts should be combined into a SolidWorks assembly.
3. In SolidWorks 2010, the procedure for creating a mesh goes as follows:
    a. Verify that the SolidWorks Add-in SolidWorks Simulation is enabled.
    b. Create a new simulation by clicking on Simulation > Study.
    c. Name the study and click the green checkmark to proceed. Note the study tab that appears at the bottom of the screen.
    d. Create a mesh by right-clicking on Mesh in the Simulation toolbar > Create Mesh…
    e. Expanded the Advanced group in the dialog.
    f. Select the Draft Quality Mesh checkbox. This ensures that mesh elements will be first-order tetrahedral.
    g. Expand the Mesh Parameters group.
    h. Change the mesh element dimension text boxes to make sure that the largest dimension will still fulfill the Nyquist criterion.
    i. Once the mesh parameters are set, click the green checkmark to create the mesh. The mesh will appear on the screen. Verify that the mesh is fine enough to represent the relative geometrical features.
4. Export the SolidWorks mesh.
    a. Select Simulation > Export…

b. Name the file according to your preference and choose the file type .geo

Opening the file in a text editor will show that the file contains:

- Some header information
- A list of nodes specified by "ND". Each node is given one index number and three points.
- Some header information for the element section.
- A list of elements specified by "EL". Each element has an index number, a domain, and four nodes associated with it.

5. Use the MATLAB GridFromMesh.m (see Appendix E) script to specify grid dimensions and then convert the mesh to a grid.

APPENDIX C

MECHANICAL DRAWINGS

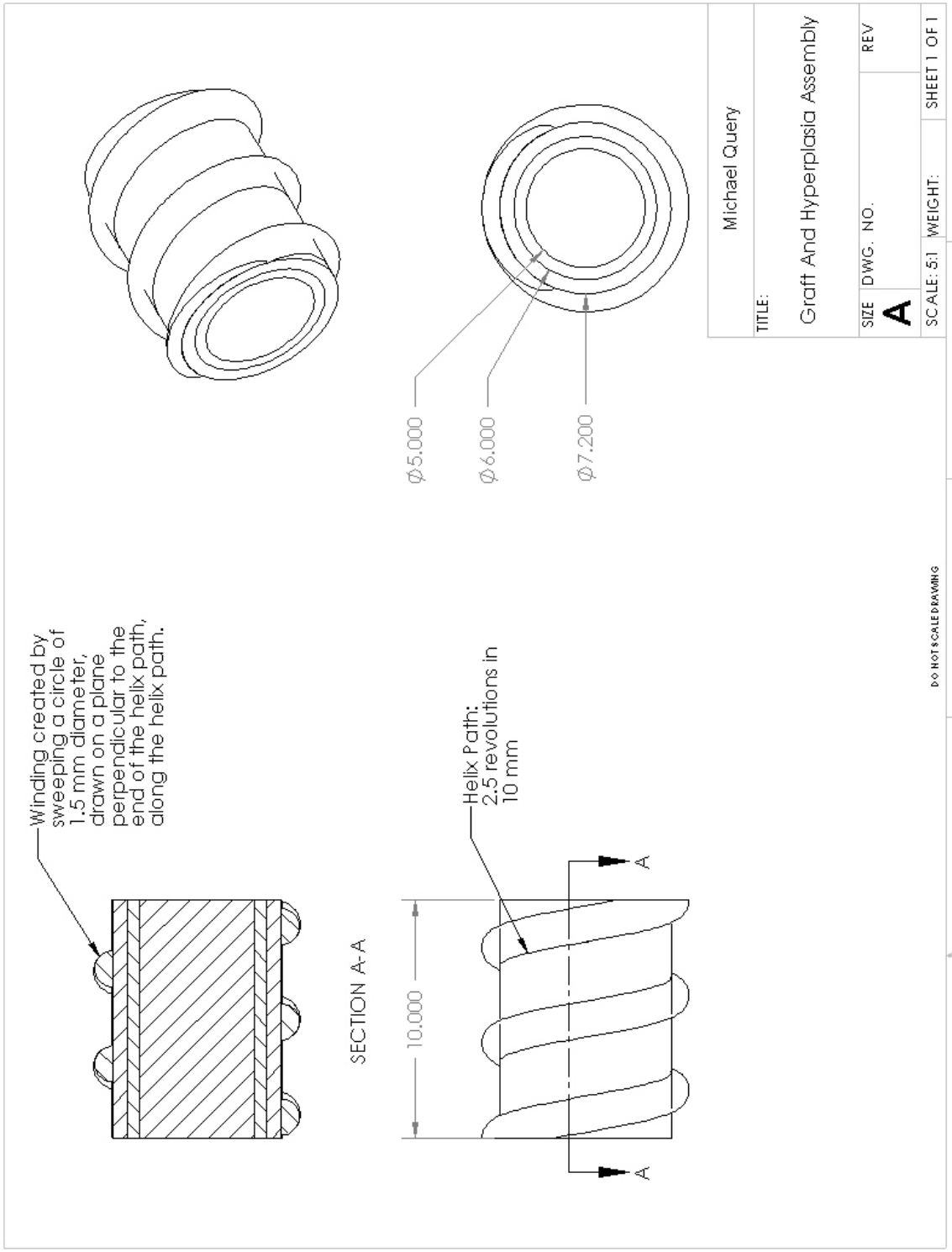
Winding created by sweeping a circle of 1.5 mm diameter, drawn on a plane perpendicular to the end of the helix path, along the helix path.
SECTION A-A
10.000
Helix Path: 2.5 revolutions in 10 mm
A
A
Ø5.000
Ø6.000
Ø7.200
Michael Query
TITLE:
Graft And Hyperplasia Assembly
SIZE
A
DWG. NO.
REV
SCALE: 5:1
WEIGHT:
SHEET 1 OF 1
DO NOT SCALE DRAWING
1
2
3
4
5

APPENDIX D

MRTI RESULTS

Figure 22 shows MRI images that correspond to the planes at which temperature was acquired. Planes were chosen during the experiment to gather data in front of the graft, at the graft's near wall, at the center of the graft, at the graft's far wall, and behind the graft.

Figure 23 contains the MRI images overlain with MRTI temperature maps for the planes in front of the graft and at the near graft wall for Exposure #1. This single figure is representative of all other heating data at that plane because there was no clear localized heating in that area for all power levels and focus placements.

Figures 24 through 35 contain MRI images overlain with MRTI temperature maps over the course of the exposure period at various depths. The scaling for temperature across all figures is consistent.

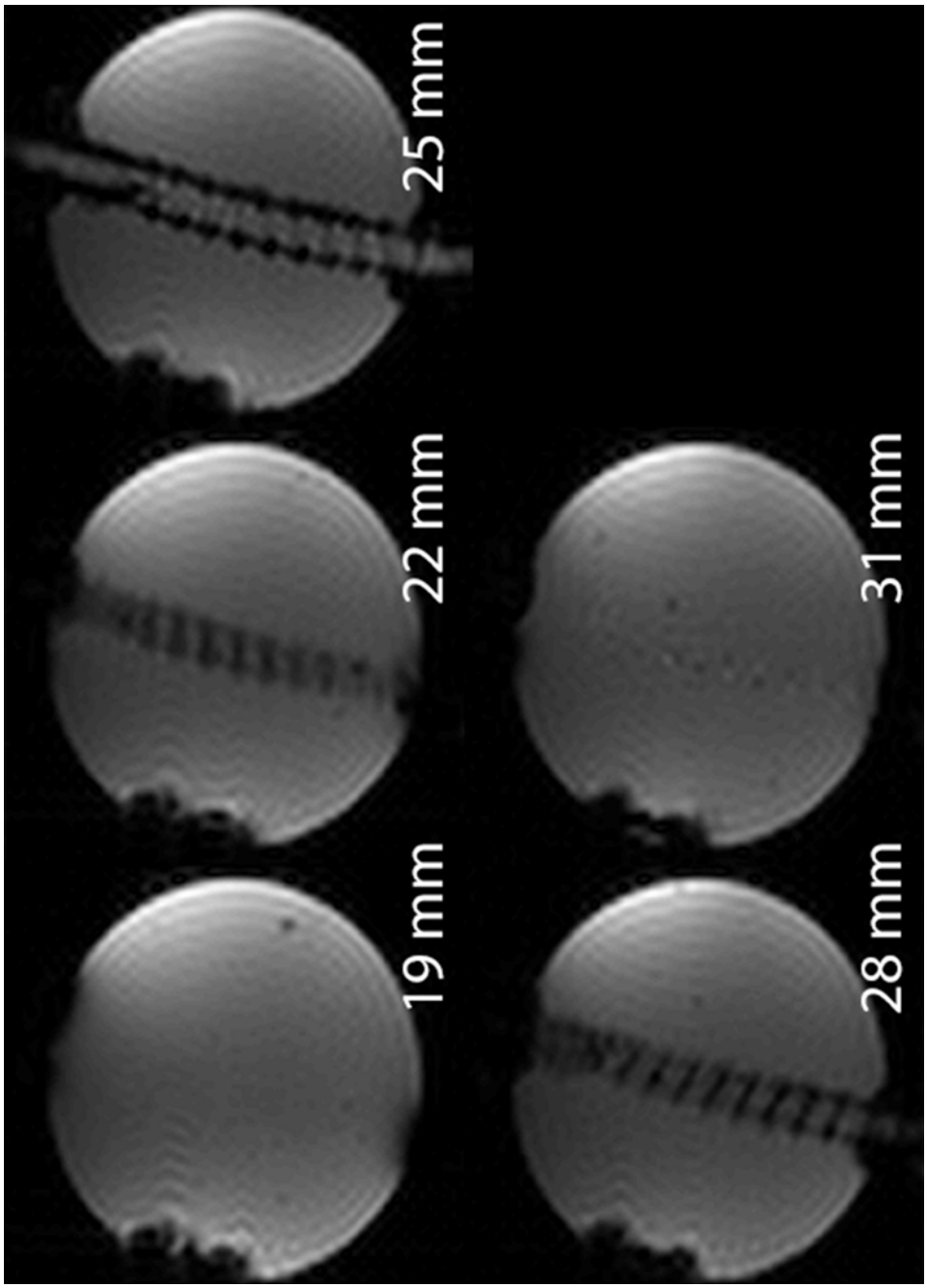

Figure 22. MRI images of graft model at temperature planes. Distances are measured from the face of the graft model nearest the transducer. Images are perpendicular to the direction of ultrasound propagation.

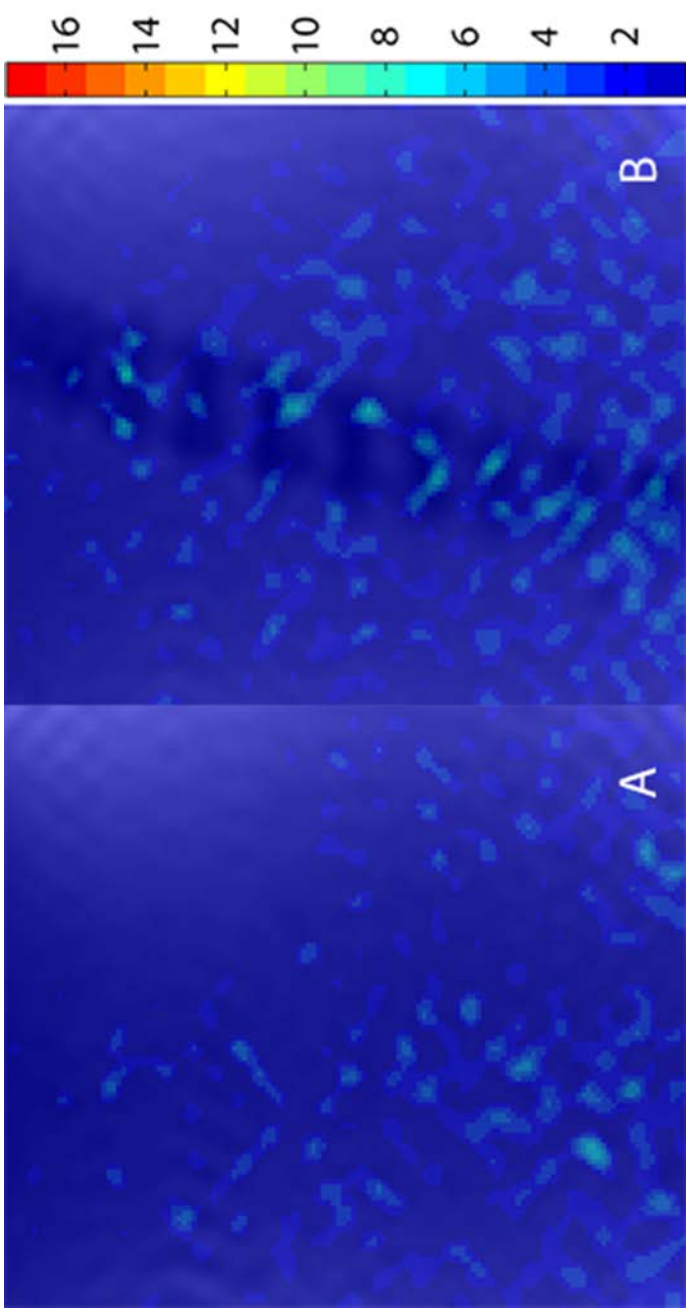

Figure 23. Temperature rise profile in degrees Celsius with geometry overlay after 30 seconds of exposure. Parameters: 8-W electrical input, ultrasound focus at graft far wall, no flow. A. 19 mm from front face of model (before graft near wall). B. 22 mm from front face of model (at graft near wall).

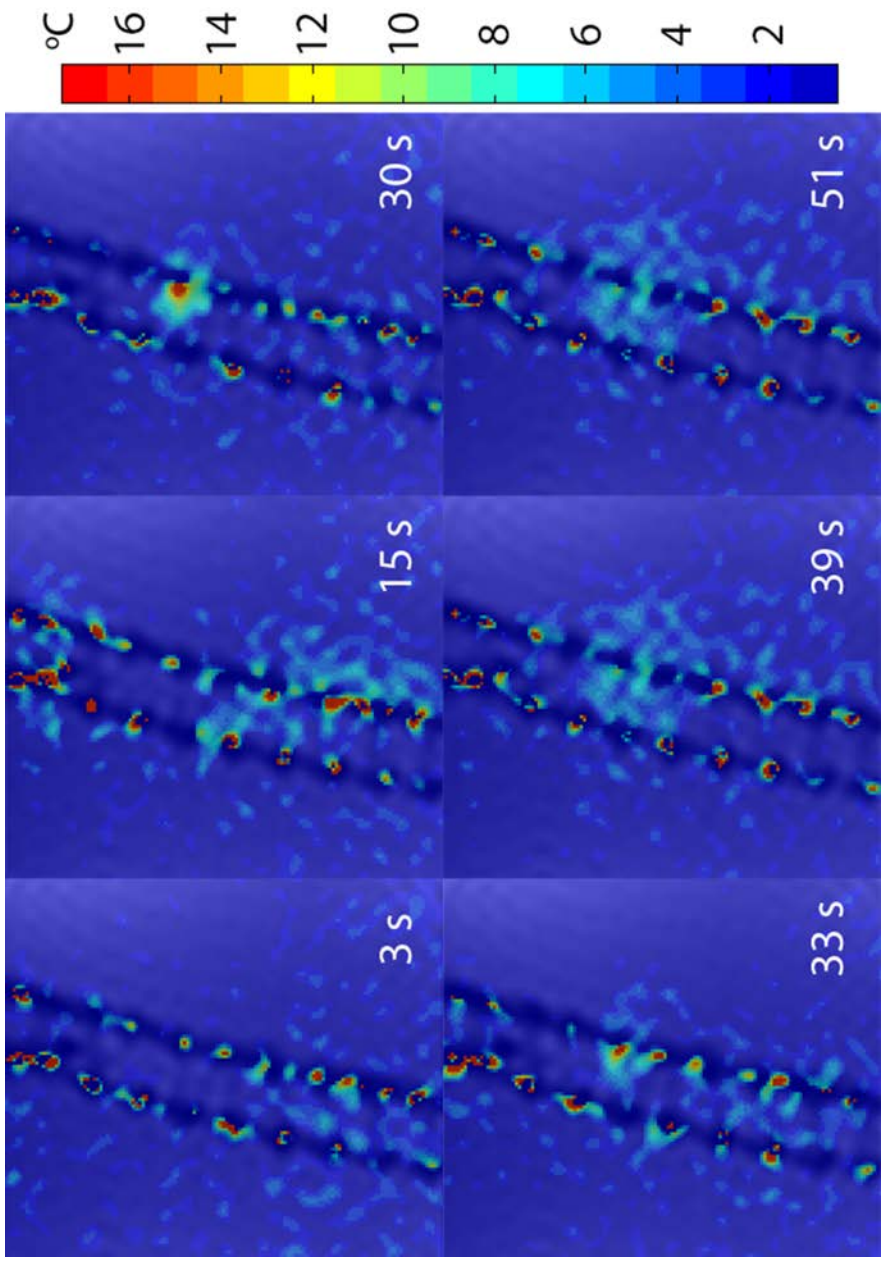

Figure 24. Temperature rise profile with geometry overlay at various times after exposure initiation. Parameters: 8-W electrical input, ultrasound focus at graft far wall, no flow, all planes are 25 mm from front of model. 30 seconds marks the end of ultrasound transmission.

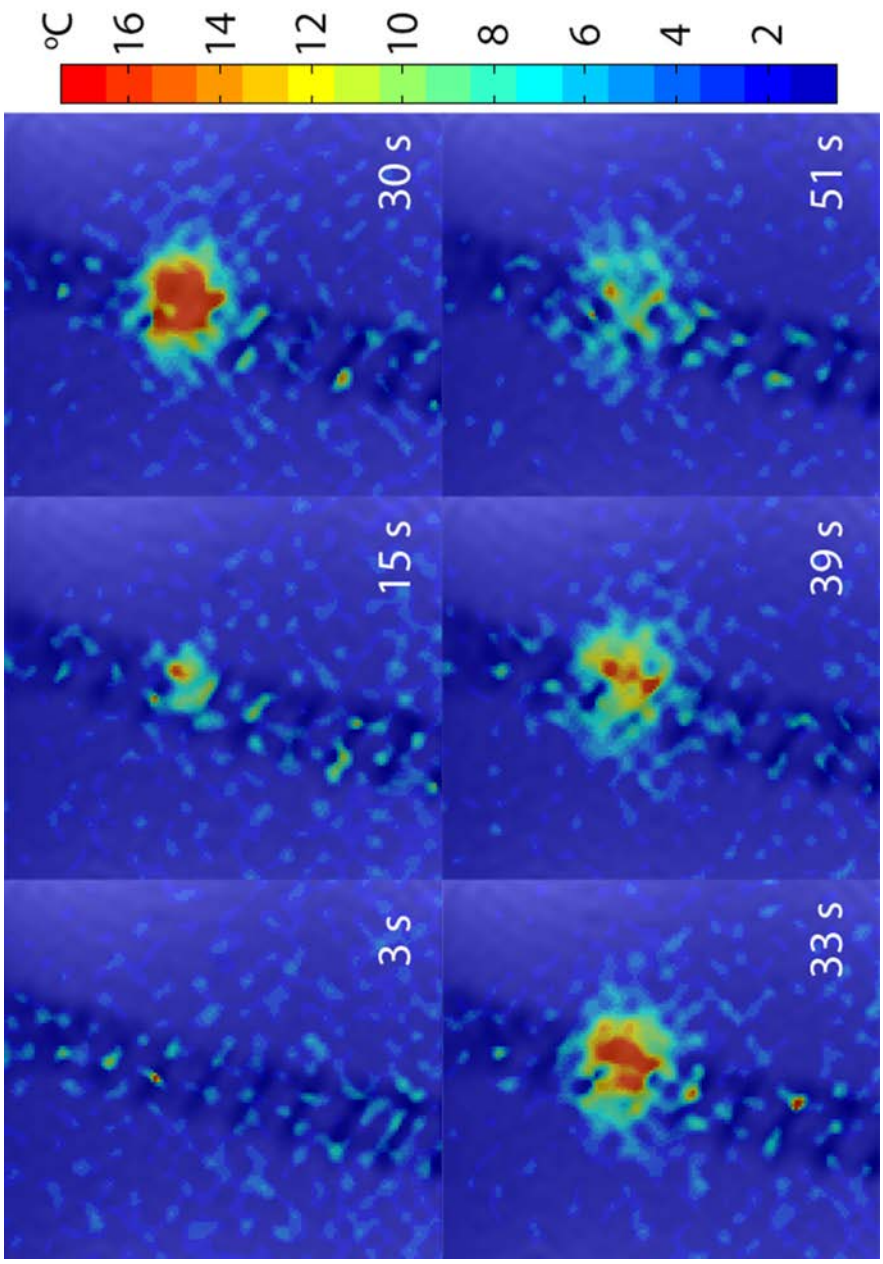

Figure 25. Temperature rise profile with geometry overlay at various times after exposure initiation. Parameters: 8-W electrical input, ultrasound focus at graft far wall, no flow, all planes are 28 mm from front of model. 30 seconds marks the end of ultrasound transmission.

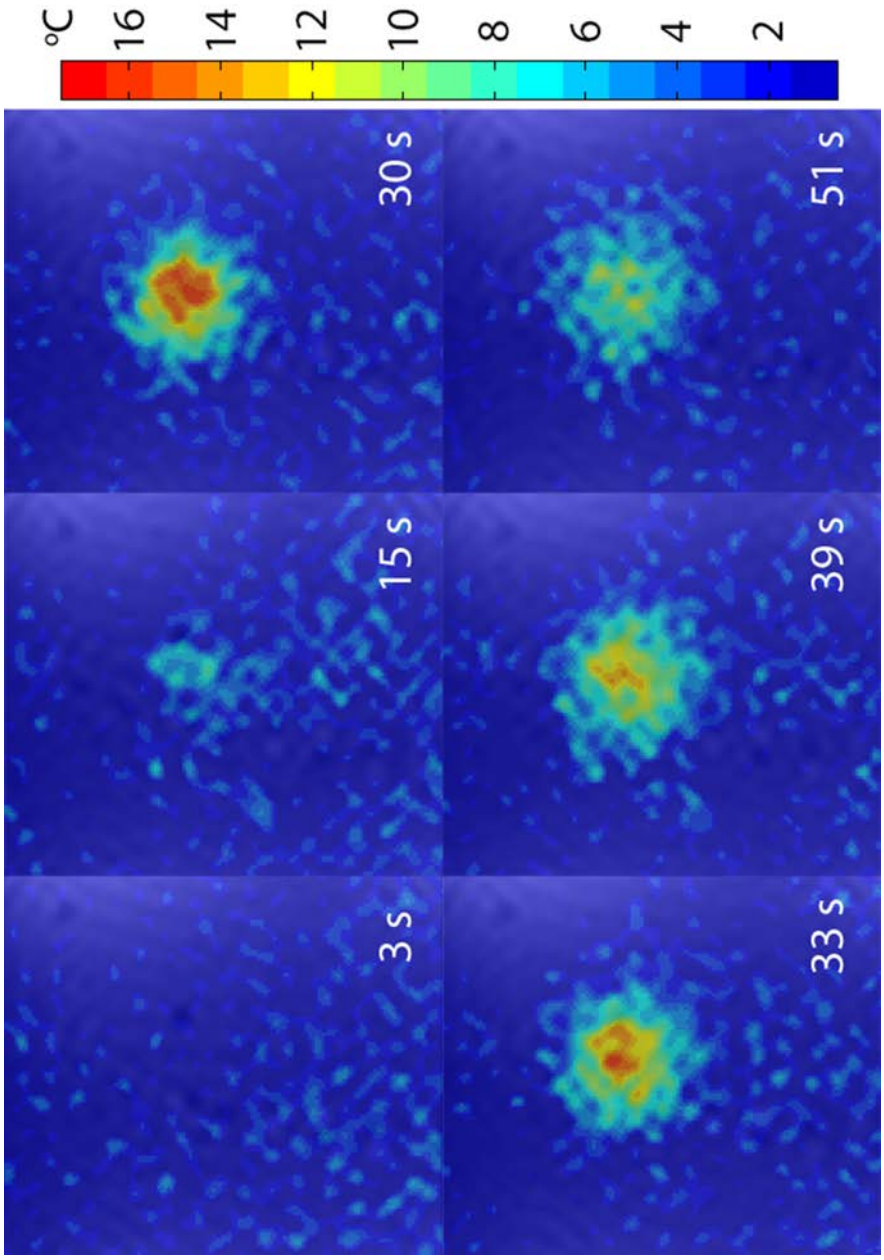

Figure 26. Temperature rise profile with geometry overlay at various times after exposure initiation. Parameters: 8-W electrical input, ultrasound focus at graft far wall, no flow, all planes are 31 mm from front of model. 30 seconds marks the end of ultrasound transmission.

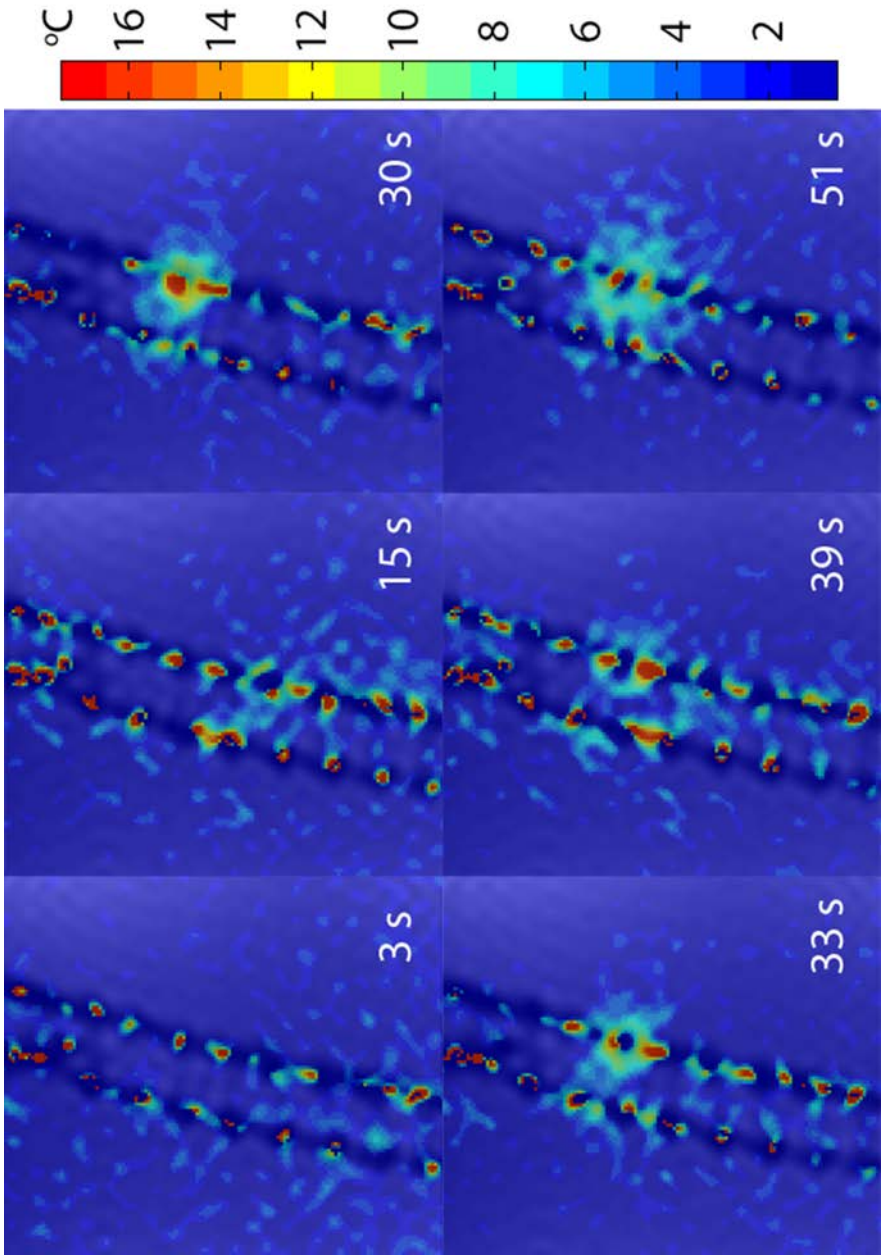

Figure 27. Temperature rise profile with geometry overlay at various times after exposure initiation. Parameters: 15-W electrical input, ultrasound focus at graft far wall, no flow, all planes are 25 mm from front of model. 30 seconds marks the end of ultrasound transmission.

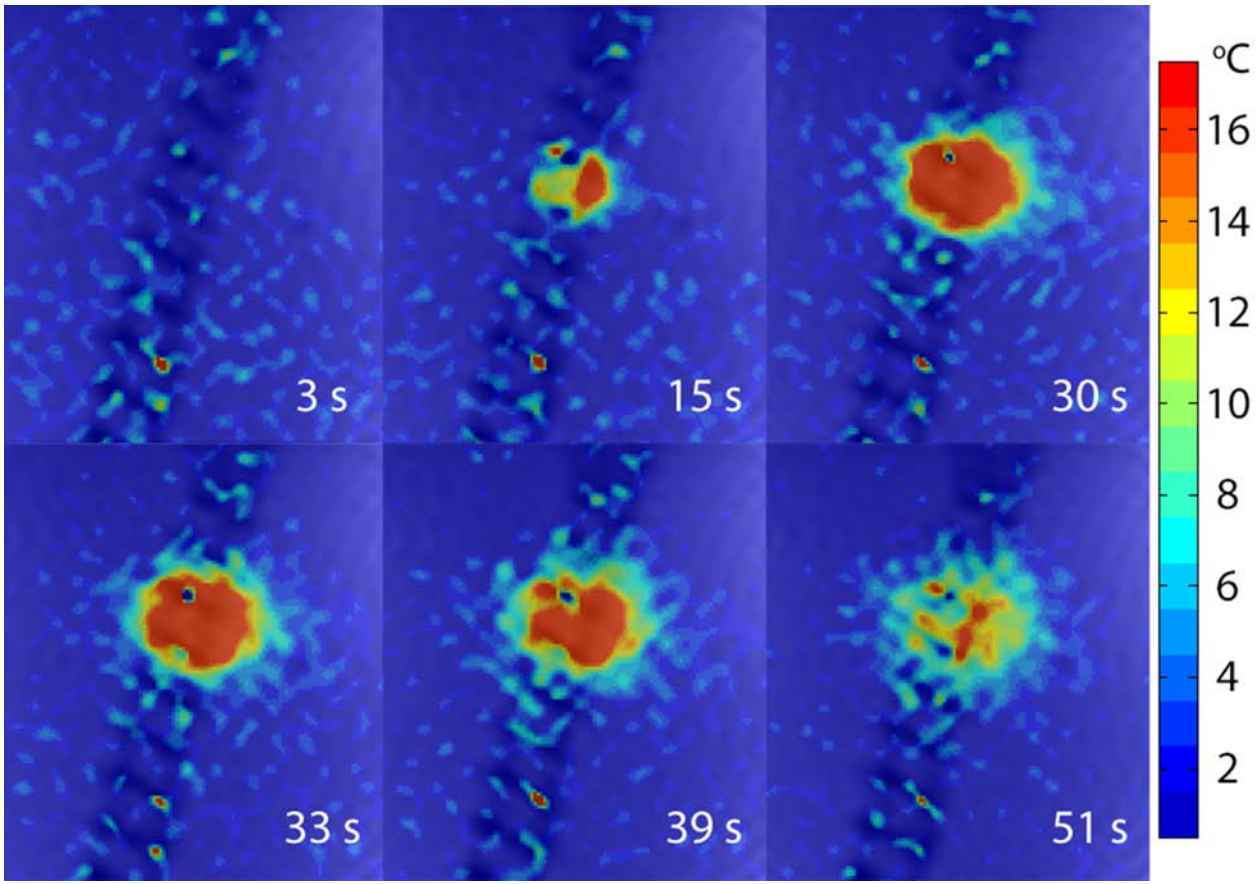

Figure 28. Temperature rise profile with geometry overlay at various times after exposure initiation. Parameters: 15-W electrical input, ultrasound focus at graft far wall, no flow, all planes are 28 mm from front of model. 30 seconds marks the end of ultrasound transmission.

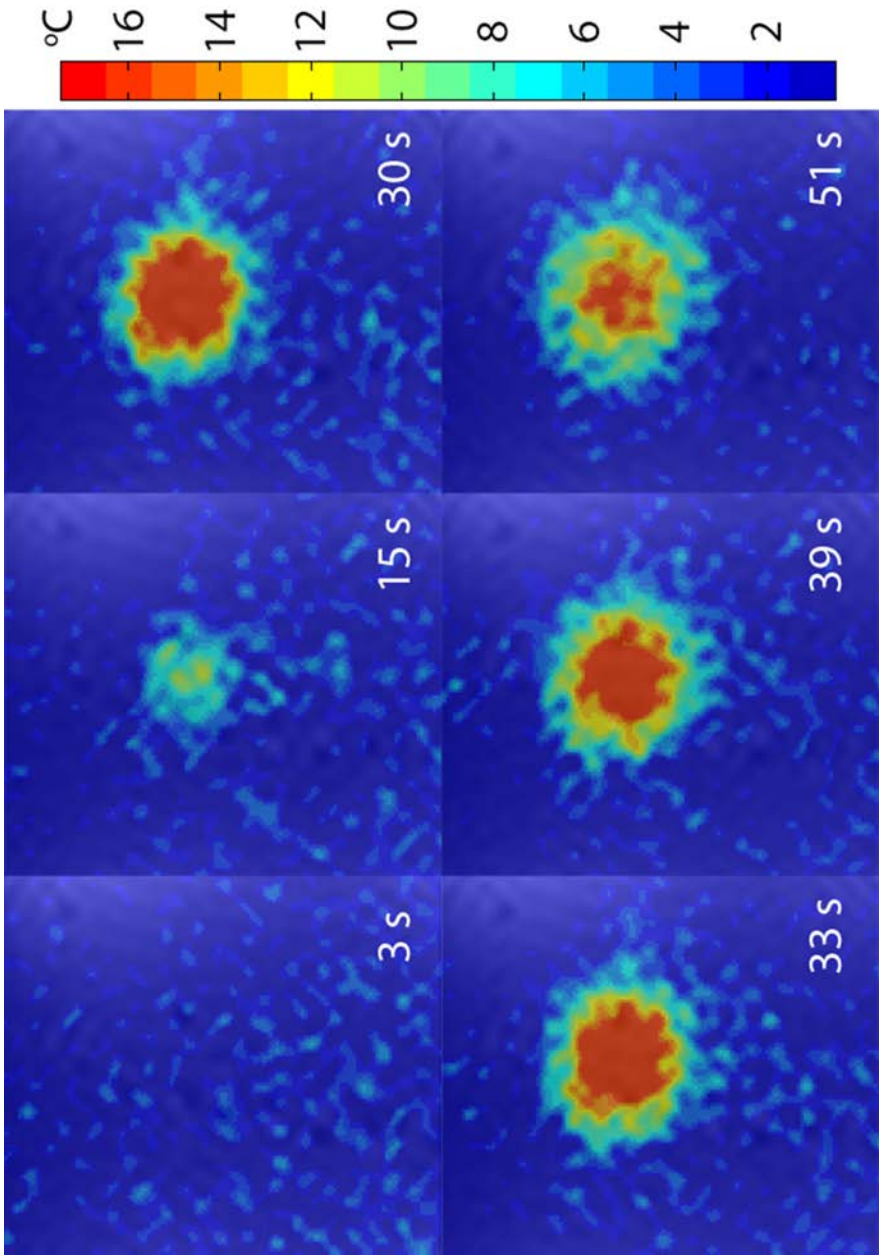

Figure 29. Temperature rise profile with geometry overlay at various times after exposure initiation. Parameters: 15-W electrical input, ultrasound focus at graft far wall, no flow, all planes are 31 mm from front of model. 30 seconds marks the end of ultrasound transmission.

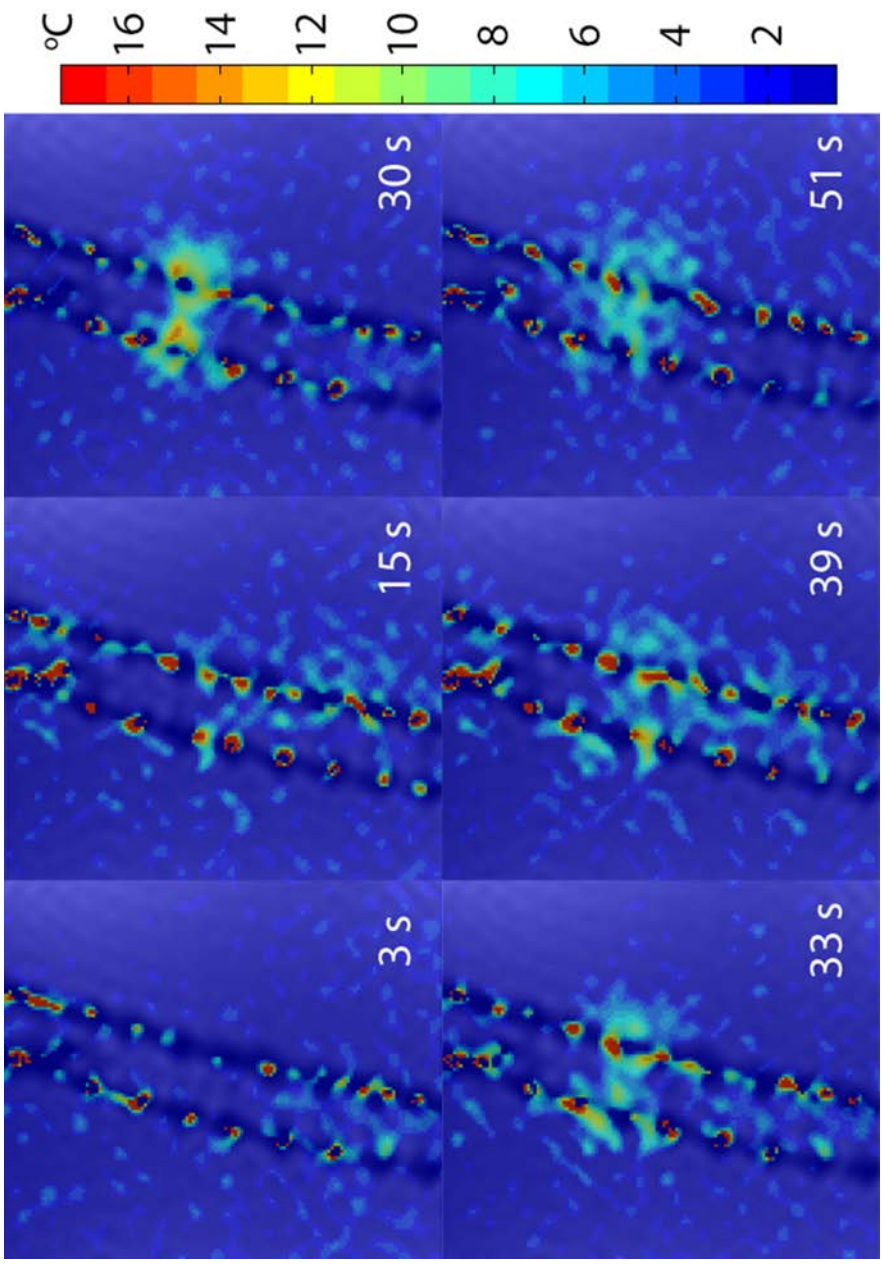

Figure 30. Temperature rise profile with geometry overlay at various times after exposure initiation. Parameters: 15-W electrical input, ultrasound focus 7 mm behind graft far wall, no flow, all planes are 25 mm from front of model. 30 seconds marks the end of ultrasound transmission.

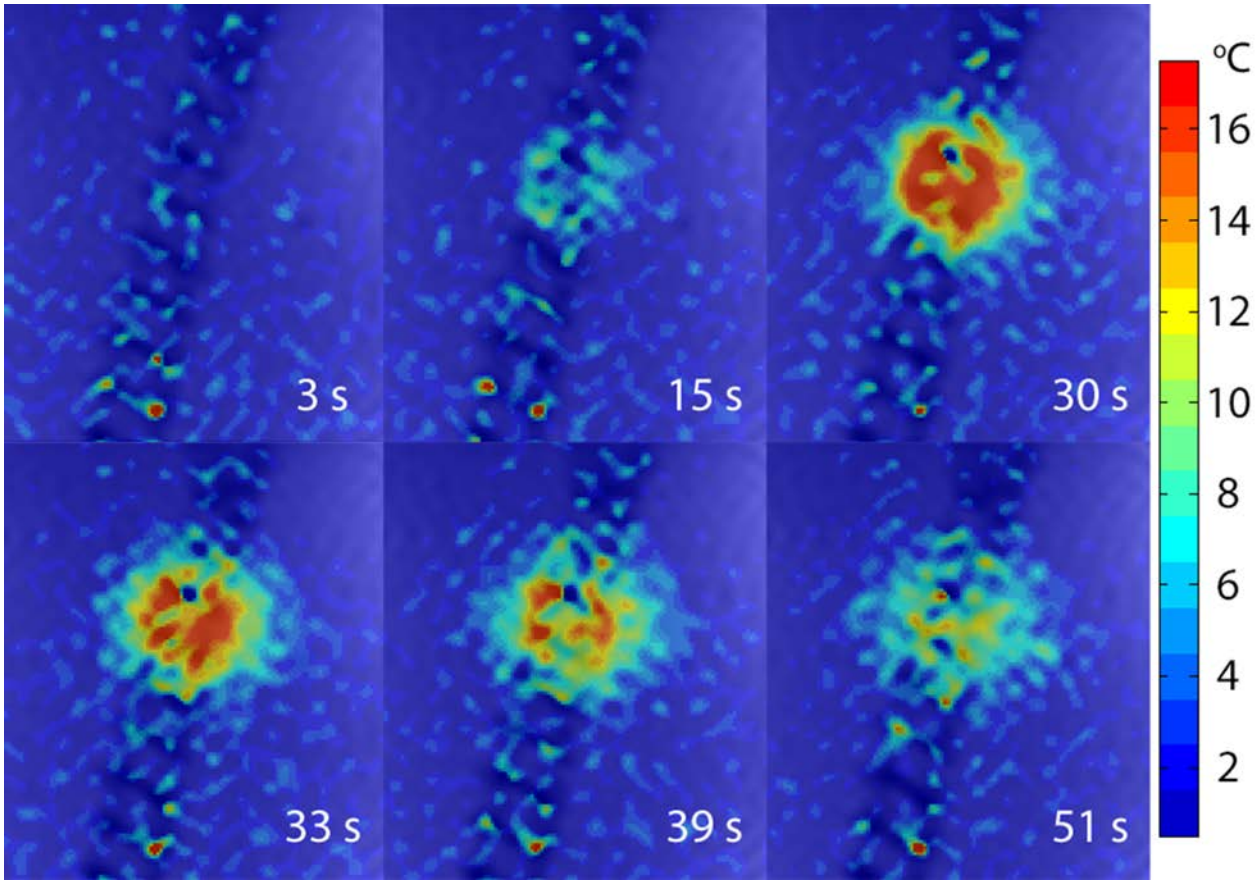

Figure 31. Temperature rise profile with geometry overlay at various times after exposure initiation. Parameters: 15-W electrical input, ultrasound focus 7 mm behind graft far wall, no flow, all planes are 28 mm from front of model. 30 seconds marks the end of ultrasound transmission.

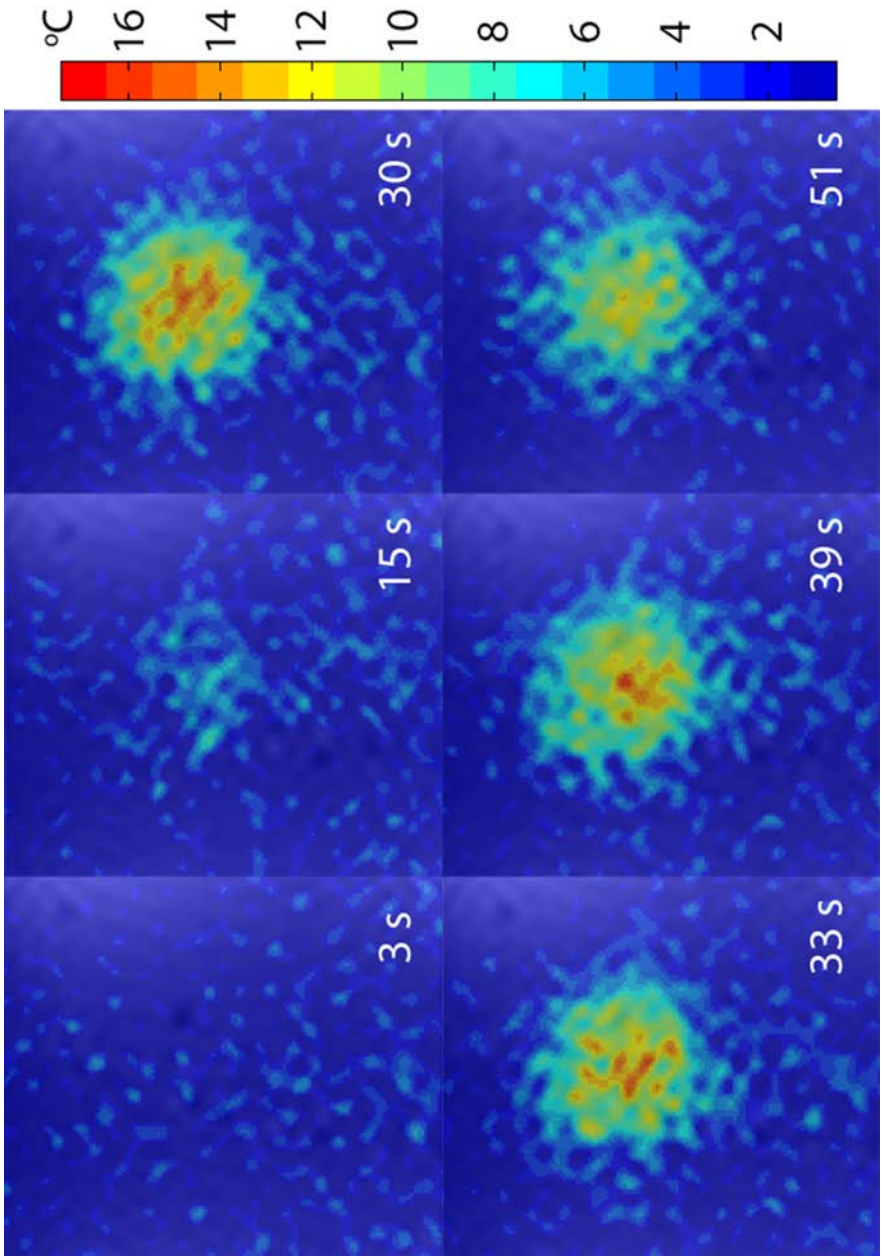

Figure 32. Temperature rise profile with geometry overlay at various times after exposure initiation. Parameters: 15-W electrical input, ultrasound focus 7 mm behind graft far wall, no flow, all planes are 31 mm from front of model. 30 seconds marks the end of ultrasound transmission.

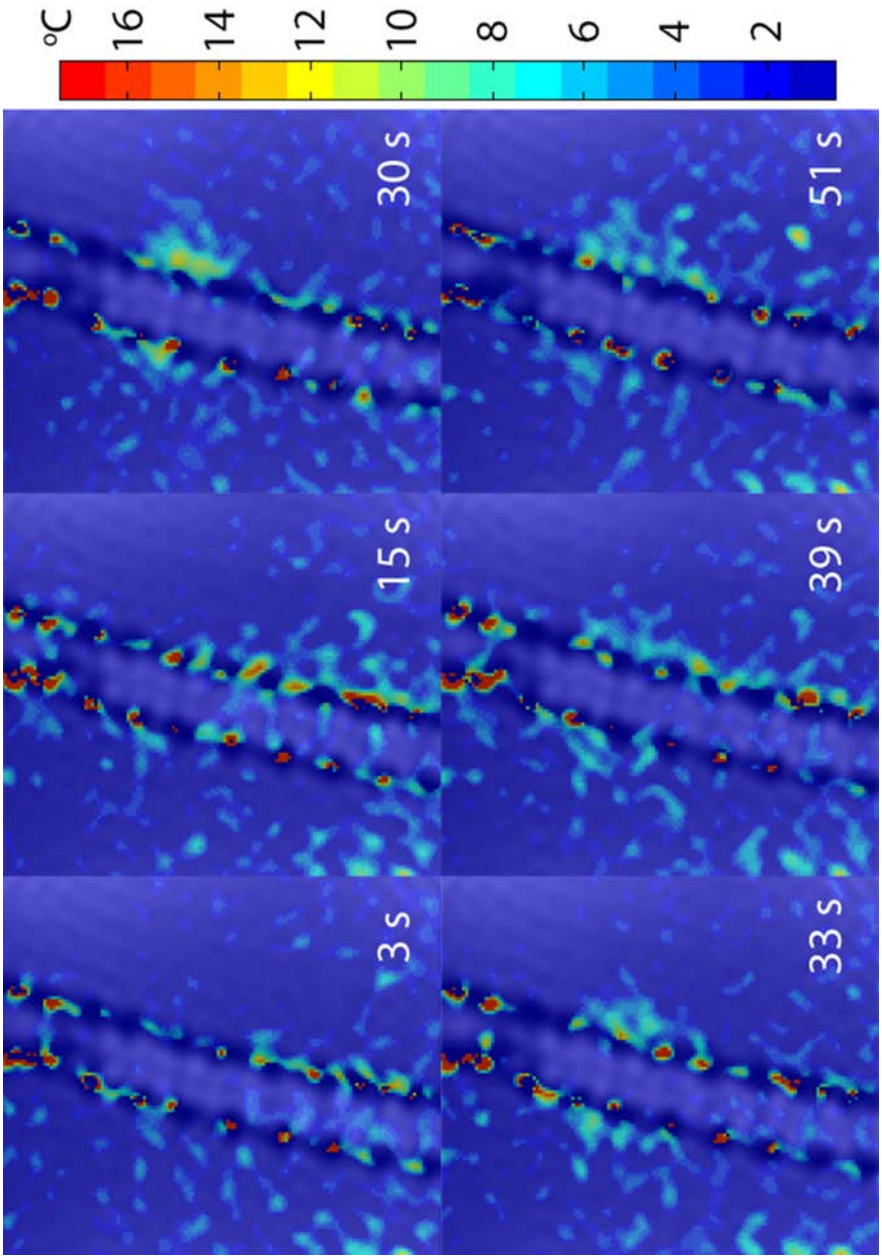

Figure 33. Temperature rise profile with geometry overlay at various times after exposure initiation. Parameters: 15-W electrical input, ultrasound focus 7 mm behind graft far wall, with flow, all planes are 25 mm from front of model. 30 seconds marks the end of ultrasound transmission.

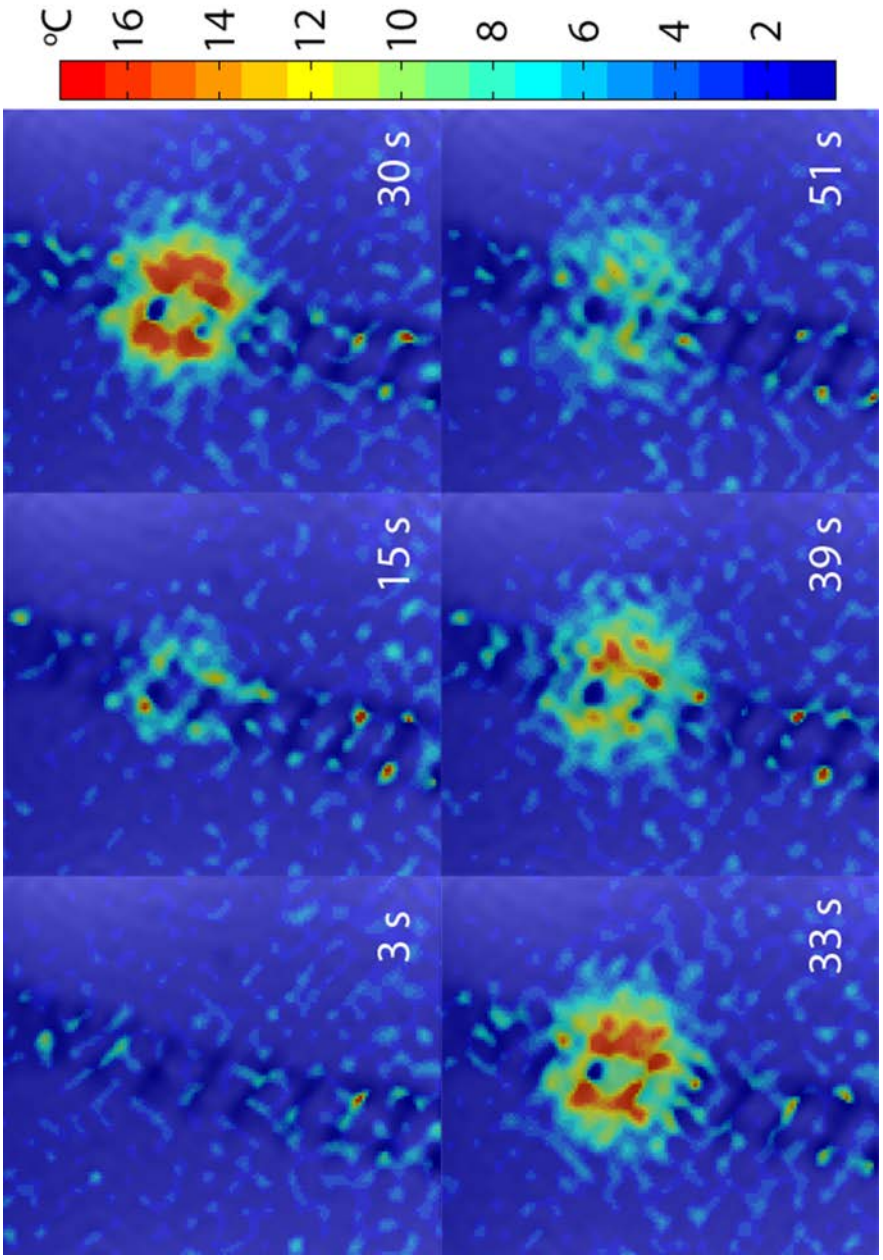

Figure 34. Temperature rise profile with geometry overlay at various times after exposure initiation. Parameters: 15-W electrical input, ultrasound focus 7 mm behind graft far wall, with flow, all planes are 28 mm from front of model. 30 seconds marks the end of ultrasound transmission.

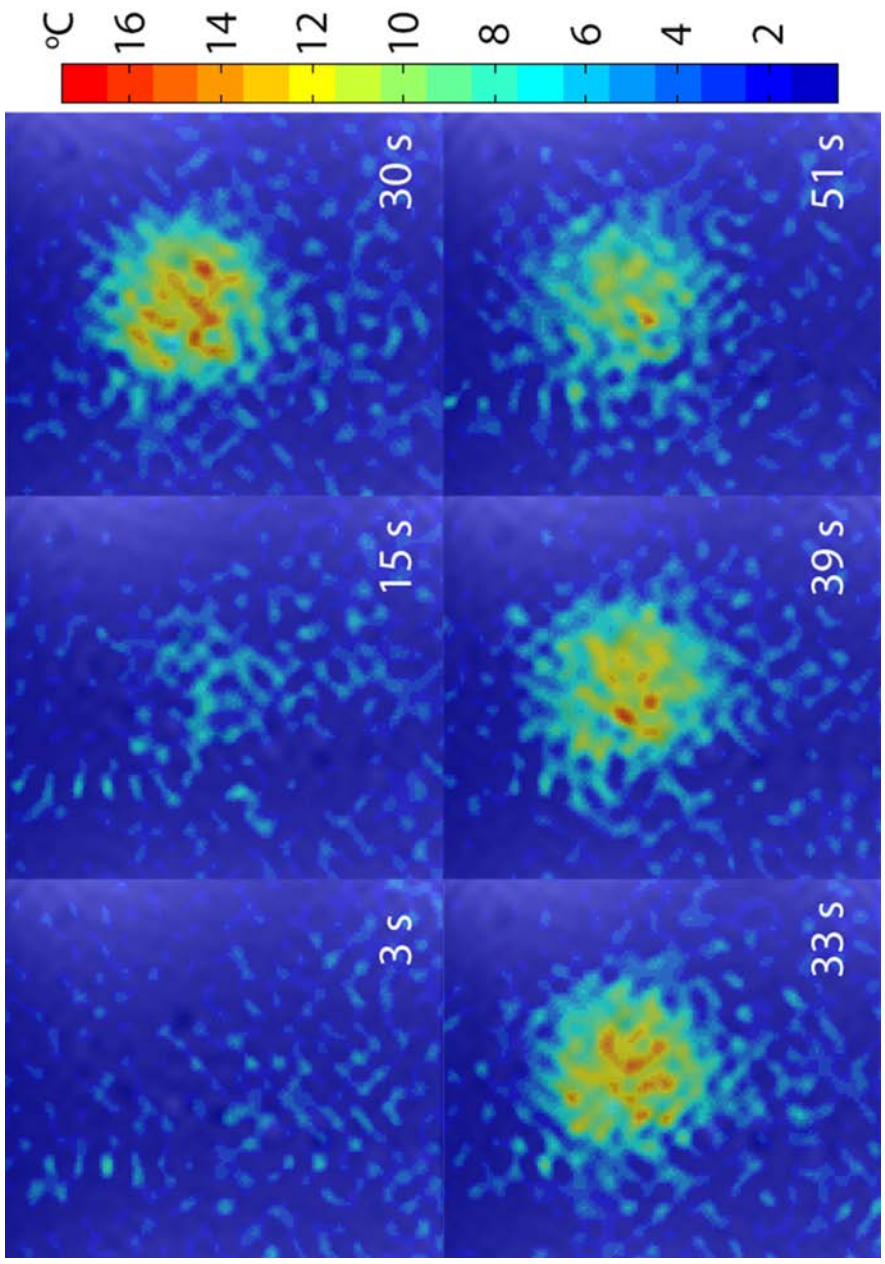

Figure 35. Temperature rise profile with geometry overlay at various times after exposure initiation. Parameters: 15-W electrical input, ultrasound focus 7 mm behind graft far wall, with flow, all planes are 31 mm from front of model. 30 seconds marks the end of ultrasound transmission.

APPENDIX E

MATLAB CODE

E.1 ToComsol.m

```
function ToComsol(input_file, thinfactor)
% Writes a text file for COMSOL from an ERFA file

% INPUTS
% input_file: a string that contains the full path to a .mat file
% containing a 3D Q variable and paramscell, an output from the HAS
% routine which defines the spacing of matrix values.

% thinfactor: the factor by which Q's dimensions are divided.  The
% resulting matrix always has odd numbered dimensions.

% NOTES
% The output file is written the same location as the input file.  The
name
% is the same as the input file except that the extension is changed to
% .txt

% COMSOL Grid File Format:
% %Grid
% x grid points separated by spaces
% y grid points separated by spaces (optional)
% z grid points separated by spaces (optional)
%
% %Data
% Data values separated by spaces

% User defined variables
input_file = input_file(1:end-4); % remove .mat extension
input_file_ext = '.mat';
% Check for cancellation
output_file = input_file;
output_file_ext = '.txt';
bottom_left_coord = [-5 -5 0];     % bottom left coordinate for Modl in
comsol
```

```
% Automation script
input_filename = [input_file input_file_ext];
output_filename = [output_file output_file_ext];
load(input_filename);
w = warning ('off','all');
delete(output_filename);
warning(w);

[xdim ydim zdim] = size(Q);
ds = paramscell{7,2};
dx = ds(1);
dy = ds(2);
dz = ds(3);

% Check if thinfactor is not 1. Perform thinning.
if thinfactor ~=1
    % Find the subscripts of the midpoint in x,y, and z.
    midx = ceil(xdim/2);
    midy = ceil(ydim/2);
    midz = ceil(zdim/2);

    % Find the starting point of the new matrix
    startx = mod(midx,thinfactor);
    starty = mod(midy,thinfactor);
    startz = mod(midz,thinfactor);
    if ~startx; startx = thinfactor; end;
    if ~starty; starty = thinfactor; end;
    if ~startz; startz = thinfactor; end;

    % Write vectors with the subscripts to be used in the downsampled
    % matrix
    xthin = startx:thinfactor:xdim;
    ythin = starty:thinfactor:ydim;
    zthin = startz:thinfactor:zdim;

    temp = zeros(length(xthin),length(ythin),length(zthin));
%     hw = waitbar(0,'Thinning out Q...');
    for i=1:length(xthin);
        for j =1:length(ythin);
            for k = 1:length(zthin);
                temp(i,j,k) = Q(xthin(i),ythin(j),zthin(k));
            end
        end
%         waitbar(i/xdim);
    end

    % Define the spatial value of the origin: matrix value (1,1,1)
    bottom_left_coord(1) = bottom_left_coord(1) + (startx)*dx;
    bottom_left_coord(2) = bottom_left_coord(2) + (starty)*dy;
    bottom_left_coord(3) = bottom_left_coord (3)+ (startz)*dz;
    dx = dx*thinfactor;
    dy = dy*thinfactor;
    dz = dz*thinfactor;
    Q = temp;
```

```
    [xdim ydim zdim] = size(Q);
%     close(hw);
end



% Write the datapoints
fid = fopen(output_filename, 'wt');
fprintf(fid, '%c Grid\n', 37);  % print the percent sign

% Write the x-line
xline = 0:dx:xdim*dx-dx;
xline = xline + bottom_left_coord(1);
for i=1:xdim-1
    fprintf(fid, [num2str(xline(i)) ' ']);
end
fprintf(fid, [num2str(xline(xdim)) '\n']);

% Write the y-line
yline = 0:dy:ydim*dy-dy;
yline = yline + bottom_left_coord(2);
for i=1:ydim-1
    fprintf(fid, [num2str(yline(i)) ' ']);
end
fprintf(fid, [num2str(yline(ydim)) '\n']);

% Write the z-line
zline = 0:dz:zdim*dz-dz;
zline = zline + bottom_left_coord(3);
for i=1:zdim-1
    fprintf(fid, [num2str(zline(i)) ' ']);
end
fprintf(fid, [num2str(zline(zdim)) '\n']);


% Write the data
fprintf(fid, '%c Data\n', 37);
for k =1:zdim
    for j=1:ydim
        for i=1:xdim
            fprintf(fid, [num2str(Q(i,j,k)) ' ']);
        end
    end
end


fprintf(fid, '\n');
fclose(fid);
end
```

E.2 AnnularArrayERFAMaker.m

```
%  Program to calculate the ERFA (Element Response Function Array) for
a given phased-array
%       transducer to speed up ultrasound simulations. The program
performs Rayleigh-Sommerfeld
%     calculations for each element g (all of which are assumed to have
the same pressure and
%      zero phase) separately in a loop, thereby finding the pressure
perfa(g) on an ERFA plane due
%     to that element g. This 2D pressure matrix becomes a page in the
final ERFA 3D array of
%      size=(lmax,mmax,numelem).  Each page in the ERFA array can be
later multiplied by the complex
%      pressure associated with that element, and all pages summed to
get the total pressure on the ERFA
%     plane without repeating any R-S calculations. The ERFA plane is,
by definition here, centered on the
%     transducer coords.
%
%  The program asks for a parameter file such as paramERFA_test.m. The
transducer is spherical with
%     a radius of curvature R and overall dimensions of Dv (vertical) x
Dh (horizontal) as measured along an
%      arc. The angles from the center of curvature to the transducer
face are theta (i=elevation index) and phi
%     (k=azimuth index). The ERFA plane is a distance d away from the
furthest point of the transducer curved
%      face and is defined in cartesian coords (l=vert index, m=horiz
index) of size Lv (vertical)x Lh (horizontal).
%
%   For phased arrays, the program also asks for the element location
file, which has the thetad and phid
%       angles (in Doug's simulation coord system) to the centers of
each element.
%
%  This version is to be used in a generalized ERFA approach where the
square ERFA plane is not coincident with
%     --and is somewhat larger than--the intermediate pp plane.  The pp
pressure is later found by freq-domain
%     propagation and interpolation.  This version stores an ERFA_.mat
file with: perfa, freq, size of the ERFA
%      plane, distance sx between the xducer and ERFA plane, radius of
curvature of the xducer, and location
%     file of the elements.
%
%   If the xducer is solid, then there is only ONE page in perfa and
the location of the 'element' is stored as
%      ElemLoc=[0 0].
%
%   ERFA assumes the total radiated power is 1 W and the face pressure
of each element is set consistent
%       with this; the final pattern pressures are later adjusted in
the simulations to give the actual power in W.
%
%   Improvements:
```

```
%    1/14/11 - Added a warning if the number of samples on the ERFA
plane (lmax or mmax) is not odd (the optimum
%             since it puts the center sample on axis).
%       Changed the calculation of dxp and dyp such that the ERFA plane
length (Len) is now considered from end
%               point to end point, so dxp = Lv/(lmax-1), not dxp =
Lv/lmax. This makes the values of dxp and dyp
%            'neat' values when the number of samples is odd [e.g., if
Lv = 100 mm and lmax = 101, then dxp = 1.0 mm].
%           The Dx and Dy values in a Modl that matches ERFA will also
be 'neat' values.
%        Also saved the name of the parameter file and the dxp and dyp
values in the .mat file

%   11/29/12 - Modificatios to produce annular array elements. -Michael
%   Query
%
%   Copyright D.A. Christensen 2011
%   Jan. 14, 2011.

clear all; close all

[pfilename, pathname] = uigetfile('*.m','Open paramERFA_.m parameter
file:');
if pfilename==0; return; end
ptruncfilename=pfilename(1:length(pfilename)-2);        % strip .m from
name.
cd(pathname); eval(ptruncfilename);             % enter parameter values
into workspace.
Dim=[Dv,Dh]; anginc=[imax,kmax]; Len=[Lv,Lh]; planinc=[lmax,mmax]; %
combine some params.

prompt={'Frequency of transducer (in MHz):',...
    'Overall ARC dimensions of transducer (vert, horiz) in m:',...
    'Number of angle increments to transducer (vert, horiz):',...
    'Radius of curvature of transducer face (in m):',...
    'Is this a phased-array transducer? (1=PA, 0=solid)',...
    ' >Radius of array elements, if applicable (in m):',...
    ' >Ratio of active area to total area of array, if appl:',...
    'Distance from back of xducer to ERFA plane (in m):',...
    'Size of ERFA plane area (vert, horiz in m):',...
    'Number of increments in ERFA plane (vert, horiz):',''};
commentstr='MAKE CHANGES if any, TO VALUES, THEN PRESS OK';
titl='Parameters for ERFA Calculation'; lines=1;
initans={num2str(fMHz),num2str(Dim),num2str(anginc),num2str(R),...
    num2str(isPA),num2str(relem),num2str(activearea),num2str(d),...
    num2str(Len),num2str(planinc),commentstr};
params=inputdlg(prompt,titl,lines,initans);
if isempty(params); return; end
fMHz=str2double(char(params(1)));
Dim=str2num(char(params(2))); Dv=Dim(1); Dh=Dim(2);
anginc=str2num(char(params(3))); imax=anginc(1); kmax=anginc(2);
R=str2double(char(params(4)));
isPA=str2double(char(params(5)));
relem=str2double(char(params(6)));
activearea=str2double(char(params(7)));
```

```
d=str2double(char(params(8)));
Len=str2num(char(params(9))); Lv=Len(1); Lh=Len(2);
if Lv~=Lh; hdb=warndlg('The ERFA plane is NOT SQUARE. Continue only if
that is okay.', 'ERFA Not Square',...
        'modal'); uiwait(hdb);
end
planinc=str2num(char(params(10))); lmax=planinc(1); mmax=planinc(2);
if 2*round(lmax/2)==lmax || 2*round(mmax/2)==mmax;
    hdb=warndlg('The number of ERFA plane increments should be ODD
integers. Continue only if even is okay.',...
        'Not Odd','modal'); uiwait(hdb);
end;

f=fMHz*1e6; % convert to Hz.

i=1:imax; k=1:kmax; l=1:lmax; m=1:mmax;     % set up indices.  Careful:
i used as index here, j is imag number.
dth=Dv/(R*imax); dphi=Dh/(R*kmax);        % incremental size of source
angle (in radians).
dxp=Lv/(lmax-1); dyp=Lh/(mmax-1);   % incremental size of steps in ERFA
plane (in m).  Changed on 1/14/11.
%   Note: In this program, x is in the vertical direction and y is in
the horizontal direction, which often is
%      backwards from other programs that generate models and view
results.  But this orientation of x and y is
%     transparent to other programs since the input and output are put
in terms of 'vertical' and 'horizontal'.
th1=dth*(i-round(imax/2));       % angle row vector, centered; imax and
kmax should be odd for symmetry.
phi1=dphi*(k-round(kmax/2));    % angle row vector, centered.
thmesh1=repmat(th1',1,kmax); % imax x kmax matrix of theta values,
'meshgrid' style, over entire xducer.
phimesh1=repmat(phi1,imax,1);% imax x kmax matrix of phi values,
'meshgrid' style, over entire xducer.

Zm=rho0*c0;     % impedance of medium;
Arc=min(Dv,Dh);    % diameter along arc of circular transducer. NOTE:
only valid for circular transducers.
XducerArea=2*pi*R*R*(1-cos(Arc/(2*R)));   % area of spherical segment.
NOTE: only valid for circular transducers.
ptunif=sqrt(2*Zm*1/XducerArea); % peak pressure for 1 W of total
radiated power, if uniform and solid.


%        [filename2, pathname2] = uigetfile('*.m','Open .m file with
element theta & phi locations:');
%     if filename2==0; return; end
%      truncfilename=filename2(1:length(filename2)-2);        % strip .m
from name.
%     cd(pathname2); eval(truncfilename); valid=1;
%     if ~exist('ElemLoc','var');
%               errordlg('The .m file must contain a variable named
''ElemLoc''.','ERROR','modal');
%     return; end
%       thvect=ElemLoc(:,1); phivect=ElemLoc(:,2); % column vectors of
theta and phi.
```

```
h1=waitbar(0,'Evaluating ERFA transducer pressure pattern...');
%     numelem=size(thvect,1);

% Hand code the elements configurations
numelem = 8;
numrings = 3;
element_ind = cell(numelem,1);
colors = [0 0 1; 1 0 1];
ring_tint = 1:numrings;
ring_tint = ring_tint.^-1;
ring_tint = fliplr(ring_tint);
r = R*ones(size(phimesh1));
[x y z] = sph2cart(thmesh1,phimesh1,r);
z_zeros = find(z==0);
xmin = min(min(x(z_zeros)));
thetaMax = max(max(thmesh1));
ring_bounds_angular = 0:(thetaMax)/numrings:thetaMax;
[ring_bounds nothing nothing_again] = sph2cart(ring_bounds_angular,...
    zeros(1,numrings+1),r(1,1)*ones(1,numrings+1));
clear nothing nothing_again
ring_bounds = fliplr(ring_bounds);


% Outer ring elements
% Top
element_ind(1) = {find(x>=ring_bounds(1) & ...
    x <= ring_bounds(2) & z>=y & z>=-y)};
% Right (sides are slightly smaller due to equality boundary not
containing
% the equal too)
element_ind(2) = {find(x>=ring_bounds(1) & ...
    x <= ring_bounds(2) & z<y & z>-y)};
% Bottom
element_ind(3) = {find(x>=ring_bounds(1) & ...
    x <= ring_bounds(2) & z<=y & z<=-y)};
% Left
element_ind(4) = {find(x>=ring_bounds(1) & ...
    x <= ring_bounds(2) & z>y & z<-y)};

% Middle Ring elements (note that element 5 takes the center row)
element_ind(5) = {find(x>ring_bounds(2) & x<=ring_bounds(3) & y>=0)};
element_ind(6) = {find(x>ring_bounds(2) & x<=ring_bounds(3) & y<0)};

% Inner Ring elements (note that element 7 takes the center row)
element_ind(7) = {find(x>ring_bounds(3) & x<=ring_bounds(4) & y>=0)};
element_ind(8) = {find(x>ring_bounds(3) & x<=ring_bounds(4) & y<0)};

% h= surf(x,y,z);
% set(h,'edgecolor','none');
hold on
for b = 1:4
    hc                                                              =
plot3(x(element_ind{b}),y(element_ind{b}),z(element_ind{b}),'.');
    set(hc,'color',ring_tint(1)*colors(mod(b,2)+1,:));
end
hold off
```

```
hold on
for b = 5:6
    hc                                                                  =
plot3(x(element_ind{b}),y(element_ind{b}),z(element_ind{b}),'.');
    set(hc,'color',ring_tint(2)*colors(mod(b,2)+1,:));
end
axis square
axis equal
hold off

% Inner ring elements
hold on
for b = 7:8
    hc                                                                  =
plot3(x(element_ind{b}),y(element_ind{b}),z(element_ind{b}),'.');
    set(hc,'color',ring_tint(3)*colors(mod(b+1,2)+1,:));
end
axis square
axis equal
hold off

dead_ind = find(abs(y)<.01 & abs(z)<.08/2);
hold on
plot3(x(dead_ind),y(dead_ind),z(dead_ind),'w.')
set(gca,'color','none')
axis square
axis equal
hold off
pause
pts_on_arc = find(x>=xmin);
activearea = 1-numel(dead_ind)/numel(pts_on_arc);
title(['Active area = ' num2str(activearea)])

      % correction of next line on Jan 6, 2011:
ptelem=ptunif/sqrt(activearea);      % adjust pressure to account for
percentage of xducer dead area.
% --- Loop through the elements starting here ---
perfa=zeros(lmax,mmax,numelem);     % preallocation for speed.
ptall=zeros(imax,kmax);            % start a pressure log for entire
transducer.
for g=1:numelem;       % cycle through elements, finding a page of ERFA
for each element.

%
distfromelem=R*acos((cos(thvect(g))*cos(thmesh1)).*cos(phivect(g)-
phimesh1)...
%         +sin(thvect(g))*sin(thmesh1));   % great circle distance from
center of element g.

%       indelemlin= find(distfromelem<=relem);   % find linear indices
inside round element g.
    indelemlin = element_ind{g};
    [indelemi,  indelemk]=ind2sub([imax,kmax],indelemlin);     % convert
to subscripts.
%     is=min(indelemi);  ie=max(indelemi);
```

```
%     ks=min(indelemk);  ke=max(indelemk);
%     th2=th1(is:ie);     % angle row vector only around element.
%     phi2=phi1(ks:ke);     % angle row vector only around element.
%      isize=size(th2,2);       % size of rectangle enclosing element g
only, so only integrate element.
%     ksize=size(phi2,2);
%      thmesh2=repmat(th2',1,ksize); % isize x ksize meshgrid of theta
values, only around element.
%      phimesh2=repmat(phi2,isize,1);  % isize x ksize meshgrid of phi
values, only around element.
    pt=zeros(imax,kmax);        % start with blank pressure over entire
field.
    pt(indelemlin)=ptelem; % pressure consistent with 1W and zero phase
inside round element .
    pt(dead_ind) = 0; % write over the elements for the dead area
%     pt2=pt(is:ie,ks:ke);         % pressure matrix inside the element
rectangle only.
    ss5=R*(cos(thmesh1).*sin(phimesh1));  % 2D matrix: imax x kmax.
    s=repmat(ss5,[1,1,lmax]);           % now 3D array.
    yp=dyp*(m-round(mmax/2));       % vector.

    aa5=R*(cos(thmesh1).*cos(phimesh1));
    a=repmat(aa5,[1,1,lmax]);           % 3D array: imax x kmax x lmax.
    b=R-a;

    tt= R*sin(thmesh1);
    t=repmat(tt,[1,1,lmax]);            % 3D array.
    xxp(1,1,:)=dxp*(l-round(lmax/2));   % turn into 'page' vector, lmax
pages long.
    xp=repmat(xxp,[imax,kmax,1]);       % 3D array.
    term1=(t-xp).^2;
    term3=(d-b).^2;

    cth=cos(thmesh1);                           % cos theta matrix for
spherical integration.
    ppc=pt.*cth;                               % pt is transducer source
matrix (must be imax x kmax).
    pc=repmat(ppc,[1,1,lmax]);            % product of pressure and cos
theta now 3D array.
    kk=2*pi*f/c0;

    ppi=zeros(kmax,lmax,mmax);          % preallocate storage for ppi.

    for mi=1:mmax
        r=sqrt(term1 + term3 + (s-yp(mi)).^2);   % r is 3D array for
each value of yp.
        ppi(:,:,mi)=(f*R*R*dth*dphi/c0)*sum(pc.*exp(1j*(-kk*r          +
(pi/2))).*r);
        % Rayleigh-Sommerfeld integral over xp only here, for one value
of yp.
        waitbar(mi/mmax, h1, ['Element: ' num2str(g)])
    end
    perfa(:,:,g)=shiftdim(sum(ppi));
%     if g==1
% %         figure;
% %         hh1=pcolor(pt); axis equal; shading flat;
```

```
% %          figure; hh2=pcolor(squeeze(abs(perfa(:,:,g)))); axis equal;
shading flat;
%             button6=questdlg('Do you want to continue with Rayleigh-
Sommerfeld calculations?',...
%              'CONTINUE','Yes','Quit','Yes');
%          if strcmp(button6,'Quit'); close all; close(h1); return; end
%      end
    ptall=ptall+pt;
    pp = CombinePlanes(perfa(:,:,g),1,1);
    subplot(2,1,1)
    surf(abs(pp));
    axis equal
    axis square
    title(['Element: ' num2str(g)]);
    xlabel('X');
    ylabel('Y');
    subplot(2,1,2)
    hold on
    surf(x,y,z);
    plot3(x(indelemlin),y(indelemlin),z(indelemlin),'.');
    xlabel('X');
    ylabel('Y');
    zlabel('Z');
    axis square
    axis equal
    grid on
    hold off
end         % end of g loop.

close all;
close(h1);
% pcolor(ptall); axis equal;


button5 = questdlg('Do you wish to save the results?','Save?');
if strcmp(button5,'Yes')
    [newfile,newpath]  =  uiputfile('ERFA_.mat','Save  binary  ERFA_.mat
file:');
    if newfile~=0;
        fullfile=[newpath newfile];
        sx=d;
        % Save key parameters in .mat file

save(fullfile,'perfa','fMHz','Len','sx','R','isPA','pfilename','dxp','d
yp')
    end
end
```

E.3 OptimizationScript.m

```
% Optimization script.
% Assumes that a perfa file has been created for the solid control
% transducer and the semi-annular array design transducer.

% A function erfaDiff has been written to be minimized. erfaDiff
describes
% the error or difference between two pressure planes.

% Load initial files
load ERFA_SolidWithDeadZoneAtFocus_151x151.mat
perfaDead = perfa;  % Load the perfa file for design transducer
load ERFA_SolidAtFocus_151x151.mat
perfaFull = perfa; % Load the perfa file for the control transducer

% Allocate memory for initial magnitude and phase and initial guess for
% minimization routine
m_init = ones(1,8);
p_init = zeros(1,8);

% Concatenate variables to be minimized in an input array
v = [m_init;p_init];

% Function handle to function to be minimized
fun = @(v) erfaDiff(perfaFull,perfaDead,v(1,:),v(2,:));
% Minimization options
options = optimset('MaxIter',10000,'MaxFunEvals',10000);
[v_opt fval] = fminsearch(fun,v,options) % minimzation call

% Extract minimized magnitudes and phases from minimazation array
m = v_opt(1,:);
p = v_opt(2,:);

% Get real pressures from control, design_before, and design_after
pressFull = perfaFull;
pressDead = CombinePlanes(perfaDead,m_init,p_init);
pressDeadOpt = CombinePlanes(perfaDead,m,p);

% Plotting
h = figure;
surf(abs(pressFull));
h1 = findall(h,'type','axes');
zlim = get(h1,'ZLim');
axis equal
axis square
set(h1,'Zlim',zlim);
title('pressFull');

h = figure(2);
surf(abs(pressDead));
h2 = findall(h,'type','axes');
axis equal
axis square
```

```
set(h2,'ZLim',zlim);
title('pressDead');

h = figure(3);
surf(abs(pressDeadOpt));
h3 = findall(h,'type','axes');
axis equal
axis square
set(h3,'ZLim',zlim);
title('pressDeadOpt');
```

E.4 ERFAdiff.m

```
function out = ERFAdiff(soln,optm,m,p)
    % This function controls the definition of residual between to
complex
    % pressure planes of the same size.

    % Residual defined in a least squares approach
%     out = sum(sum(abs(sqrt((soln - CombinePlanes(optm,m,p)).^2))));

    % Residual defined as difference in real pressure
    out = sum(sum((abs(abs(soln)-abs(CombinePlanes(optm,m,p))))));
end
```

E.5 CombinePlanes.m

```
function pp = CombinePlanes(perfa, mags, phases)
% This function takes arguments of a perfa file, a vector of magnitude
% scalars and vector of phases in radians.
% The function output is the resulting complex prssure matrix.
    [px py g] = size(perfa);
    if g~=length(mags)
        error('mags does not contain the same number of elements as the
perfa planes.');
    end
    if g~=length(phases)
        error('phases does not contain the same number of elements as
the perfa planes.');
    end

    % Combine ERFA planes and phase, preallocate for speed
    pp = zeros(px, py);
    for i = 1:g
        pp = pp + perfa(:,:,i).*mags(i).*exp(j*phases(i));
    end
end
```

E.6 MeshFromGeo.m

```
close all;
clear all;
clc;

% Script for reading in a mesh from a .geo file
% The .geo file comes from the export of a SolidWorks mesh.

folder = 'C:\Users\Michael\Desktop\';
[filename pathname] = uigetfile('*.geo','Pick a csv',folder);
if (isequal(filename,0) || isequal(pathname,0))
    return;
end
filepath = [pathname filename];
fin = fopen(filepath,'r');

hw = waitbar(0,'Initializing file...');
% Find number of lines in the file
lineCount = 0;
nodeCount = 0;
elementCount = 0;
line = fgetl(fin);
while(line)
    if(strcmp(line(2:3),'ND'))
        nodeCount = nodeCount + 1;
    elseif(strcmp(line(2:3),'EL'))
        elementCount = elementCount + 1;
    end
    lineCount = lineCount + 1;
    line = fgetl(fin);
end
fclose(fin);
fin = fopen(filepath,'r');

close(hw)
hw = waitbar(0,'Reading in Mesh');
% Read until the beginning of the node listing
lineNumber = 1;
line = fgetl(fin);
while(~strcmp(line(2:3),'ND'))
    line = fgetl(fin);
    lineNumber = lineNumber + 1;
    waitbar(lineNumber/lineCount);
end

% Read in the nodes
count = 1;
nodeCount = 1;
while(strcmp(line(2:3),'ND'))
    node = sscanf(line, '%*s%d,%f%f%f%*s');
    nodes(count,:) = node(2:end);
    count = count + 1;
    line = fgetl(fin);
    lineNumber = lineNumber + 1;
```

```
    nodeCount = nodeCount + 1;
    waitbar(lineNumber/lineCount);
end

% Read until the elements list
while(~strcmp(line(2:3),'EL'))
    line = fgetl(fin);
end

% Read in the elements into meshRegions
count = 1;
regCount=0;
regions = meshRegion;
% elements = zeros(elementCount,4);
while(strcmp(line(2:3),'EL'))
    element = sscanf(line, '%*s%d%*s%*s%d%*s%*d%d%d%d%d%*s');
    if (regCount~=element(2)) % this format assumes that the regions
are grouped together in the file format
        regCount = element(2);
        regions(regCount).Elements = zeros(elementCount,4); % allocate
memory for the next region.Elements (will be trimmed later)
        count = 1;
    end
    regions(regCount).Elements(count,:) = element(3:6);
    count = count + 1;
    line = fgetl(fin);
    lineNumber = lineNumber + 1;
    waitbar(lineNumber/lineCount);
end
close(hw);
for i = 1:length(regions)
    regions(i).Elements(regions(i).Elements == 0) = []; % delete zero
entries in just-completed region see note [1] at bottom of file
            regions(i).Elements = ...
                reshape(regions(i).Elements,...
                numel(regions(i).Elements)/4,4);
    regions(i).Nodes = nodes;
end
```

E.7 GridFromMesh.m

```
clc
% Load a mesh if one doesn't exist already
if (~exist('regions','var'))
    [loadfile loadpath] = uigetfile('.mat','Load a mesh file...');

    if (isequal(loadfile, 0)|| isequal(loadpath,0))
        return;
    end

    load(fullfile(loadpath,loadfile));
end
nodes = regions(1).Nodes;
% Create the grid to overlay
ptsPerSide = 301;

% setup the divisions and grid extents
dx = .01/ptsPerSide;
dy = dx;
dz = dx;
xLen = dx*ptsPerSide;
yLen = dy*ptsPerSide;
zLen = dz*ptsPerSide;

% retrieve model extents
modelxLim = [min(nodes(:,1)) max(nodes(:,1))];
modelyLim = [min(nodes(:,2)) max(nodes(:,2))];
modelzLim = [min(nodes(:,3)) max(nodes(:,3))];

% Find the midpoints with respect to x, y, z
xMid = sum(modelxLim)/2;
yMid = sum(modelyLim)/2;
zMid = sum(modelzLim)/2;

% Set Grid extents
xLim = [xMid-xLen/2 xMid+xLen/2];
yLim = [yMid-yLen/2 yMid+yLen/2];
zLim = [zMid-zLen/2 zMid+zLen/2];

% Set x,y,z vectors
xvec = xLim(1):dx:xLim(2)-dx;    % set up vectors that describe the
three axes
yvec = yLim(1):dy:yLim(2)-dy;
zvec = zLim(1):dz:zLim(2)-dz;

% Set Modl
Modl = ones(ptsPerSide,ptsPerSide,ptsPerSide);  % initialize modl
(everything not set remains a 1)


[xgrid ygrid zgrid] = meshgrid(xvec,yvec,zvec); % setup meshgrid to
avoid explicit looping
```

```
% Loop over regions
for i = 1:length(regions)
    hw   =   waitbar(0,['Evaluating   region   '   num2str(i)   '   of   '
num2str(length(regions))]);
    indices  =  zeros(1,length(nodes));  % initialize indices, will be
trimmed later.
    indPointer = 1;
    % Loop over elements and decide which points they contain
    for j = 1:length(regions(i).Elements)
        inside = zeros(ptsPerSide,ptsPerSide,ptsPerSide); %inside (used
to evaulate points in elements)
        waitbar(j/length(regions(i).Elements));
        element = regions(i).Elements(j,:); % extract the node indices
        points  =  regions(i).Nodes(element,:);  % create a 2D (m x 3)
array of m no. of x,y,z points corresponding to nodes indices

        % Create a local cube
        localmaxx = max(points(:,1));
        localminx = min(points(:,1));
        localmaxy = max(points(:,2));
        localminy = min(points(:,2));
        localmaxz = max(points(:,3));
        localminz = min(points(:,3));

%         t1 = tic;
        localxind = find(xvec>=localminx & xvec <=localmaxx);
        localyind = find(yvec>=localminy & yvec <=localmaxy);
        localzind = find(zvec>=localminz & zvec <=localmaxz);
        [localj              locali              localk]              =
meshgrid(localxind,localyind,localzind);
        locali = reshape(locali,numel(locali),1);
        localj = reshape(localj,numel(localj),1);
        localk = reshape(localk,numel(localk),1);
        localind = sub2ind(size(xgrid),locali,localj,localk);
        localind = reshape(localind,numel(localind),1);
%         t1p = toc(t1)

        %%%%% This is the bottleneck in this algorithm %%%%%
%         t2 = tic;
%         % Find the meshgrid indices that correspond to the local cube
%         localxind = find((xgrid>=localminx) & (xgrid<=localmaxx));
%         localyind = find(ygrid>=localminy & ygrid<=localmaxy);
%         localzind = find(zgrid>=localminz & zgrid<=localmaxz);
%                                                          localind2      =
intersect(localxind,intersect(localyind,localzind));
%         t2p = toc(t2)
        %%%%%%%%%%%%%%%%%%%%%%%%%%%%%%%%%%%%%%%%%%%%%%%%%%%%%%%%%%%%%%%

        % Set local grid to 1
        inside(localind) = 1;

        for k = 1:4 % Compare all four planes
            A = points(mod(k,4)+1,:);
            B = points(mod(k+1,4)+1,:);
            C = points(mod(k+2,4)+1,:);
            D = points(mod(k+3,4)+1,:);
```

```
            % Set the local cube to ones in preparation to eliminate
            % exterior points

            % Solve the equation for a plane ax + by + cz + d = 0;
            normal = cross(C-A,B-A);
            d = -dot(normal, A);

            % assign a sign for values on the inside half-space
            inside_sign = ((dot(normal,D) + d )>= 0);
            inside(localind)  =  inside(localind)  .*  (~xor(inside_sign,
...
                (normal(1).*xgrid(localind)                              +
normal(2).*ygrid(localind)...
                + normal(3).*zgrid(localind))+d >= 0));
        end
        temp = find(inside);

        % Plotting
%
tetramesh(regions(i).Elements(j,:),regions(i).Nodes,'FaceAlpha',.25);
%         hold on
%         plot3(xgrid(temp), ygrid(temp),zgrid(temp),'r.')
% %         hold off
%         grid on
%         axis equal
%         axis square
%         axis equal

        indices(indPointer:indPointer + numel(temp)-1) = temp;
        indPointer = indPointer + numel(temp);
    % End of elements
    end
    indices(indices == 0) = []; % remove zero padding see note [1]
    Modl(indices) = i + 1;
%     plot3(xgrid(indices), ygrid(indices), zgrid(indices) , 'r.');
%     grid on
% End of regions
    close (hw)
end

[savefilename, savepathname] = uiputfile( '*.mat', 'Save as');
if (isequal(savefilename,0) || isequal(savepathname,0))
    return;
end

savefile = [savepathname savefilename];
save(savefile, 'Modl');

% [1]:   setting elements of an array equal to [] deletes those
elements.
```

E.8 GridFromMesh.m

```
% GridFromMesh Script
MeshFromGeo;
GridFromMesh;
```

E.9 meshRegion.m

```
classdef meshRegion
    %   mesRegion: A region of a tetrahedral mesh.
    %
    %   A part of full tetrahedral mesh containing multiple regions.  A
    %   region specifies a continuous domain with homogenous acoustic
    %   properties.
    %
    %   Class Properties:
    %    Nodes: A list of nodes containing indices for all the nodes
used
    %    in the model.   This may include nodes that are not actually
used by
    %   this meshRegion
    %   Elements: A list of elements (made of nodes) that define this
    %   region
    %
    %   Class Methods:
    %    Plot: The region can be viewed in tetramesh form with the Plot
method.

    properties
        Nodes = zeros(1,1);
        Elements = zeros(1,4);
    end

    methods
        function this = meshRegion()
            this.Nodes = zeros(1,1);
            this.Elements = zeros(1,4);
        end
        function h = Plot(this)
            h       =       tetramesh(this.Elements,       this.Nodes,
ones(1,length(this.Elements)), 'FaceAlpha',.25);
            grid on;
        end
    end

end
```

REFERENCES

[1] T. Kataoka, Y. Honda, H. Bonneau, P. Yock, and P. Fitzgerald, "New Catheter-Based Technology for the Treatment of Restenosis," *J Interven Cardiol,* vol. 15, pp. 371-380, 2002.

[2] B. Mark Richard and M. R. Brinton, "Ultrasound-induced thermal therapy of hyperplasia in hemodialysis access grafts," Thesis (M.S.)--Dept. of Electrical and Computer Engineering, University of Utah, 2010., 2010.

[3] D. B. Vickers, "Hyperthermia for treatment of hyperplasia in a hemodialysis access graft," Thesis (M.S.)--Dept. of Bioengineering, University of Utah, 2008., 2008.

[4] A. Asif, F. N. Gadalean, D. Merrill, G. Cherla, C. D. Cipleu, D. L. Epstein*, et al.*, "Inflow stenosis in arteriovenous fistulas and grafts: a multicenter, prospective study," *Kidney international,* vol. 67, p. 1986.

[5] J. A. Vassalotti, W. C. Jennings, G. A. Beathard, M. Neumann, S. Caponi, C. H. Fox*, et al.*, "Fistula First Breakthrough Initiative: Targeting Catheter Last in Fistula First," *Seminars in Dialysis,* vol. 25, pp. 303-310.

[6] S. Hwang, D. H. Jung, T. Y. Ha, C. S. Ahn, D. B. Moon, K. H. Kim*, et al.*, "Usability of ringed polytetrafluoroethylene grafts for middle hepatic vein reconstruction during living donor liver transplantation," *Liver Transpl,* vol. 18, pp. 955-65, Aug 2012.

[7] S. K. Gupta, F. J. Veith, H. B. Kram, and K. R. Wengerter, "Prospective, randomized comparison of ringed and nonringed polytetrafluoroethylene femoropopliteal bypass grafts: a preliminary report," *J Vasc Surg,* vol. 13, pp. 163-72, Jan 1991.

[8] S. Cullen, S. Y. Ho, D. Shore, C. Lincoln, and A. Redington, "Congenital stenosis of pulmonary veins—failure to modify natural history by intraoperative placement of stents," *Cardiology in the Young,* vol. 4, pp. 395-398, 1994.

[9] T. Hodges, M. Fillinger, R.Zwolak, D. Walsh, F. Bech, and J. Crenenwett, "Longitudinal Comparison of Dialysis Access Methods: Risk Factors for Failure,"

Journal of Vascular Surgery, vol. 26, pp. 1009-1019, 1997.

[10] B. C. Deuel TF, Cantley L, "Restenosis injury: a problem in regulation of growth," in *Molecular basis of cardiovascular disease*, ed Philadelphia: Saunders, 1999, pp. 367-89.

[11] P. Roy-Chaudhury, J. Zhang, M. Krishnamoorthy, Y. Wang, R. Banerjee, A. Tevar*, et al.*, "Cellular phenotypes in dialysis access stenosis: myofibroblasts, fibroblasts and contractile smooth muscle cells," *J Am Soc Nephrol,* vol. 17, p. 75A, 2006.

[12] S. Stracke, K. Konner, I. Kostlin, R. Friedl, P. Jehle, V. Hombach*, et al.*, "Increased expression of TGF-beta1 and IGF-I in inflammatory stenotic lesions of hemodialysis fistulas," *Kidney Int,* vol. 61, pp. 1011-1019, 2002.

[13] M. G. Hoffmann R, Dussaillant GR, et al., "Patterns and mechanisms of in-stent restenosis: a serial intravascular ultrasound study," *Circulation,* vol. 94, pp. 1247-1254, 1996.

[14] P. A. Kearney M, Haley L, et al., "Histopathology of in-stent restenosis in patients with periphereal artery disease," *Circulation,* vol. 95, pp. 1998-2002, 1997.

[15] Y. E. Pisoni R, Dykstra D, et al., "Vascular access use in Europe and United States: Results from DOPPS," *Kidney Int,* vol. 61, pp. 302-316, 2002.

[16] W. DW, "Vascular access: a nephrologist's point of view," *Am J Kidney Dis,* vol. 1993, pp. 457-471, 1993.

[17] T. Htay and M. W. Liu, "Drug-eluting stent: a review and update," *Vascular Health and Risk Management,* vol. 1, pp. 263-276, 2005.

[18] B. M. van Haaften AC, Moll FL, de Borst GJ, "Therapeutic options for carotid in-stent restenosis: review of the literature," *J Vasc Interv Radiol,* vol. 21, pp. 1471-7, 2010.

[19] www.fistulafirst.org, "Arteriovenous FistulaFirst," ed: Fistula First.

[20] P. Roy-chaudhury, L. Arend, J. Zhang, M. Krishnamoorthy, Y. Wang, R. Banerjee*, et al.*, "Neointimal hyperplasia in early arteriovenous fistula failure," *Kidney international,* vol. 50, p. 782, 2007.

[21] S. Sun, J. Beitler, T. Ohki, T. Calderon, R. Schechner, R. Yaparpalvi*, et al.*, "Inhibitory effect of brachytherapy on hyperplasia in arteriovenous fistula," *J Surg Res,* vol. 115, pp. 200-208, 2003.

[22] A. J. Jackson, P. Coats, and D. B. Kingsmore, "Pharmacotherapy to improve

outcomes in vascular access surgery: a review of current treatment strategies," *Nephrol. Dial. Transplant,* p. doi:10.1093/ndt/gfr552, 2012.

[23] L. Bordenave, P. Fernandez, M. Remy-Zolghadri, S. Villars, R. Daculsi, and M. D, "In vitro endothelialized ePTFE prostheses: Clinical update 20 years after the first realization.," *Clin Hemorheol Microcirc,* pp. 227-234, 2005.

[24] K. Pawlowski, S. Rittgers, S. Schmidt, and G. Bowlin, "Endothelial cell seeding of polymeric vascular grafts," *Front Biosci,* vol. 9, 2004.

[25] J. Rotmans, J. Heyligers, H. Verhagen, E. Velema, M. Nagtegaal, and D. de Kleijn, "In vivo cell seeding with anti-CD34 antibodies successfully accelerates endothelialization but stimulates intimal hyperplasia in porcine arteriovenous expanded polytetrafluoroethylene grafts," *Circulation,* pp. 12-18, 2005.

[26] D. J. Colombo A, Banning A, Grube E, Hauptmann K, Silber S, et al, "Randomized study to assess the effectiveness of slow- and moderate-release polymer-based paclitaxel-eluting stents for coronary artery lesions," *Circulation,* pp. 788-794, 2003.

[27] S. P. Regar E, Bode C, Holubarsch C, Guermonprez J, Wijns W, et al, "Angiographic findings of the multicenter Randomized Study with the Sirolimus-Eluting Bx Velocity Balloon-Expandable Stent (RAVEL): Sirolimus-eluting stents inhibit restenosis irrespective of the vessel size," *Cicrulation,* pp. 1949–1956, 2002.

[28] J. Kopecek, "Smart and genetically engineered biomaterials and drug delivery systems," *Eur J Pharm Sci,* pp. 1-16, 2003.

[29] K. Orihara, S. Biro, H. Eto, Y. Ikeda, and C. Tei, "Hyperthermia at 43°C for 2 h Inhibits the Proliferation of Vascular Smooth Muscle Cells, but not Endothelial Cells," *Journal of Molecular and Cellular Cardiology,* vol. 34, pp. 1205-1215, 2002.

[30] M. Brinton, C. Tagge, R. Stewart, A. Cheung, Y. Shiu, and D. Christensen, "Thermal sensitivity of endothelial cells on synthetic vascular graft material," *Int. J. Hyperthermia,* vol. 28, pp. 163–174, 2012.

[31] F. Lejbkowicz and S. Salzberg, "Distinct Sensitivity of Normal and Malignant Cells in Vitro," *Environmental Health Perspectives,* vol. 105, pp. 1575-1578, 1997.

[32] A. Alter, L. A. Rozenszajn, H. I. Miller, and U. Rosenschein, "Ultrasound Inhibits the Adhesion and Migration of Smooth Muscle Cells In Vitro," *Ultrasound in Med. & Biol.,* vol. 24, pp. 711-721, 1998.

[33] A. Lawrie, A. F. Brisken, S. E. Francis, D. I. Tayler, D. C. Chamberlain, and C. M. Newmann, "Ultrasound Enhances Reporter Gene Expression After Transfection of Vascular Cells In Vitro," *Circulation,* vol. 99, pp. 2617-2620, 1999.

[34] T. Kondo and E. Kano, "Enhancement of hyperthermic cell killing by nonthermal effect of ultrasound," *Int. J. Radiat. Biol.,* vol. 51, pp. 157-166, 1987.

[35] L. J. Feril, T. Kondo, Q. Zhao, and R. Ogawa, "Enhancement of hyperthermia-induced apoptosis by nonthermal effects of ultrasound," *Cancer Lett,* vol. 178, pp. 63-70, 2002.

[36] L. B. J. Feril and K. Takashi, "Biological Effects of Low Intensity Ultrasound: The Mechanism Involved, and its Implications on Therapy and Biosafety of Ultrasound," *J. Radiat. Res.,* vol. 45, pp. 479-189, 2004.

[37] P. J. Fitzgerald, A. Takagi, M. P. Moore, M. Hayase, F. D. Kolodgie, D. Corl, *et al.*, "Intravascular Sonotherapy Decreases Neointimal Hyperplasia After Stent Implantation in Swine," *Circulation,* vol. 103, pp. 1823-1831, 2001.

[38] C. J. McMahon, C. E. Mullins, and H. G. El Said, "Intrastent Sonotherapy in pulmonary vein restenosis: a new treatment for a recalcitrant problem," *Heart,* vol. 89, p. e6, 2003.

[39] R. E, T. A, G. van der Giessen, G. Sianos, J. Vos, P. Smits, *et al.*, "Sonotherapy, Antirestenotic Therapeutic Ultrasound in Coronary Arteries: The First Clinical Experience," *Catheter Cardiovasc Interv,* vol. 60, pp. 9-17, 2003.

[40] H. Mudra, M. Hug, A. Knape, and C. Spes, "Intravascular sonotherapy for treatment of in-stent restenosis," *Z Kardiol,* vol. 103, pp. 103-11, 2002.

[41] P. Serruys, A. Hoye, G. Grollier, A. Colombo, J. Symons, and H. Mudra, "A European multi-center trial investigating the anti-restenotic effect of intravascular sonotherapy after stenting of de novo lesions (EUROSPAH: EUROpean Sonotherapy Prevention of Arterial Hyperplasia," *International Journal of Cardiovascular Interventions,* vol. 2, pp. 53-60, 2004.

[42] S. Jeffrey, "theheart.org," ed, 2002.

[43] J. Vaitekunas, "VP of R&D at Cybersonics Inc.," Discussion at Ultrasonics Industry Association Conference, San Francisco ed, 2012.

[44] A. Capon and S. Mordon, "Can thermal lasers promote skin wound healing?," *Am J Clin Dermatol,* vol. 4, pp. 1-12, 2003.

[45] N. Kipshidze, V. Nikolaychik, M. Muckerheidi, M. Keelan, V. Chekanov, M.

Maternowski, *et al.*, "Effect of Short Pulsed Nonablative Infrared Laser Irradiation on Vascular Cells In Vitro and Neointimal Hyperplasia in a Rabbit Balloon Injury Model," *Circulation,* vol. 104, pp. 1850-55, 2001.

[46] C.-C. Lin, C.-F. Chang, M.-Y. Lai, T.-W. Chen, P.-C. Lee, and W.-C. Yang, "Far-Infrared Therapy: A Novel Treatment to Improve Access Blood Flow and Unassisted Patency of Arteriovenous Fistula in Hemodialysis Patients," *J Am Soc Nephrol,* vol. 18, pp. 985-992, 2007.

[48] C. S. Jørgensen and W. P. Paaske, "Physical and mechanical properties of ePTFE stretch vascular grafts determined by time-resolved scanning acoustic microscopy," *European journal of vascular and endovascular surgery : the official journal of the European Society for Vascular Surgery,* vol. 15, p. 416.

[49] N. E. Clough. Innovations in ePTFE Fiber Technology: New Capabilites, New Applications, New Opportunities. Available: http://www.gore.com/MungoBlobs/168/901/ePTFE_INNOVATIONS_PAPER.pdf

[50] A. Piattelli, A. Scarano, M. Piattelli, and S. Matarasso, "Cellular colonization and bone formation into expanded polytetrafluoroethylene membranes: a light microscopical and histochemical time course study in the rabbit," *Journal of periodontology,* vol. 67, p. 720.

[51] S. K. Williams, S. S. Berman, and L. B. Kleinert, "Differential healing and neovascularization of ePTFE implants in subcutaneous versus adipose tissue," *Journal of biomedical materials research,* vol. 35, p. 473.

[52] H. Miura, T. Nishibe, K. Yasuda, T. Shimada, K. Hazama, H. Katoh, *et al.*, "The Influence of Node-Fibril Morphology on Healing of High-Porosity Expanded Polytetrafluoroethylene Grafts," *European Surgical Research,* vol. 34, pp. 224-231.

[53] D. A. Christensen and U. Vyas, "Ultrasound beam propagation using the hybrid angular spectrum method," 2008.

[54] U. Vyas and D. Christensen, "Ultrasound beam simulations in inhomogeneous tissue geometries using the hybrid angular spectrum method," *IEEE Transactions on Ultrasonics, Ferroelectrics and Frequency Control,* vol. 59, pp. 1093-1100.

[55] F. Shen and A. Wang, "Fast- Fourier- transform based numerical integration method for the Rayleigh-Sommerfeld diffraction formula," *Applied optics,* vol. 45, p. 1102.

[56] G. R. Torr, "The acoustic radiation force," *American Journal of Physics,* vol. 52, p. 402.

[57] F. Borgnis, "Acoustic Radiation Pressure of Plane Compressional Waves," *Reviews of Modern Physics,* vol. 25, pp. 653-664.